JOURNAL OF GEOPHYSICAL RESEARCH, VOL. 115, B06407, doi:10.1029/2008JB006126, 2010

Exhumation, crustal deformation, and thermal structure of the Nepal Himalaya derived from the inversion of thermochronological and thermobarometric data and modeling of the topography

Frédéric Herman,[1,2] Peter Copeland,[3] Jean-Philippe Avouac,[1] Laurent Bollinger,[4] Gweltaz Mahéo,[5] Patrick Le Fort,[6] Santaman Rai,[6,7] David Foster,[8] Arnaud Pêcher,[6] Kurt Stüwe,[9] and Pierre Henry[10]

Received 30 September 2008; revised 16 November 2009; accepted 5 January 2010; published 24 June 2010.

[1] Two end-member kinematic models of crustal shortening across the Himalaya are currently debated: one assumes localized thrusting along a single major thrust fault, the Main Himalayan Thrust (MHT) with nonuniform underplating due to duplexing, and the other advocates for out-of-sequence (OOS) thrusting in addition to thrusting along the MHT and underplating. We assess these two models based on the modeling of thermochronological, thermometric, and thermobarometric data from the central Nepal Himalaya. We complement a data set compiled from the literature with 114 $^{40}Ar/^{39}Ar$, 10 apatite fission track, and 5 zircon (U-Th)/He thermochronological data. The data are predicted using a thermokinematic model (PECUBE), and the model parameters are constrained using an inverse approach based on the Neighborhood Algorithm. The model parameters include geometric characteristics as well as overthrusting rates, radiogenic heat production in the High Himalayan Crystalline (HHC) sequence, the age of initiation of the duplex or of out-of-sequence thrusting. Both models can provide a satisfactory fit to the inverted data. However, the model with out-of-sequence thrusting implies an unrealistic convergence rate $\geq$30 mm yr^{-1}. The out-of-sequence thrust model can be adjusted to fit the convergence rate and the thermochronological data if the Main Central Thrust zone is assigned a constant geometry and a dip angle of about 30° and a slip rate of <1 mm yr^{-1}. In the duplex model, the 20 mm yr^{-1} convergence rate is partitioned between an overthrusting rate of 5.8 ± 1.4 mm yr^{-1} and an underthrusting rate of 14.2 ± 1.8 mm yr^{-1}. Modern rock uplift rates are estimated to increase from about 0.9 ± 0.31 mm yr^{-1} in the Lesser Himalaya to 3.0 ± 0.9 mm yr^{-1} at the front of the high range, 86 ± 13 km from the Main Frontal Thrust. The effective friction coefficient is estimated to be 0.07 or smaller, and the radiogenic heat production of HHC units is estimated to be 2.2 ± 0.1 μW m^{-3}. The midcrustal duplex initiated at 9.8 ± 1.7 Ma, leading to an increase of uplift rate at front of the High Himalaya from 0.9 ± 0.31 to 3.05 ± 0.9 mm yr^{-1}. We also run 3-D models by coupling PECUBE with a landscape evolution model (CASCADE). This modeling shows that the effect of the evolving topography can explain a fraction of the scatter observed in the data but not all of it, suggesting that lateral variations of the kinematics of crustal deformation and exhumation are likely. It has been argued that the steep physiographic transition at the foot of the Greater Himalayan Sequence indicates OOS thrusting, but our results demonstrate that the best fit duplex model derived from the thermochronological and thermobarometric data reproduces the present morphology of the Nepal Himalaya equally well.

[1]Tectonics Observatory, California Institute of Technology, Pasadena, California, USA.
[2]Earth Sciences Department, ETH Zurich, Zurich, Switzerland.
[3]Department of Earth and Atmospheric Sciences, University of Houston, Houston, Texas, USA.
[4]Département Analyse Surveillance Environnement, CEA, DAM, DIF, Arpajon, France.
[5]Laboratoire des Sciences de La Terre, UMR 5570, Ecole Normale Supérieure de Lyon, Université de Lyon 1, CNRS, Villeurbanne, France.
[6]Institut Dolomieu, Université Joseph Fourier, Grenoble, France.
[7]Now at Department of Geology, Tribuhvan University, Kirtipur, Gandhi Bhawan, Kathmandu, Nepal.
[8]Department of Geological Sciences, University of Florida, Gainesville, Florida, USA.
[9]Institut für Geologie, Universität Graz, Graz, Austria.
[10]CEREGE, Europole de l'Arbois, Aix-en-Provence, France.

0148-0227/10/2008JB006126

Citation: Herman, F., et al. (2010), Exhumation, crustal deformation, and thermal structure of the Nepal Himalaya derived from the inversion of thermochronological and thermobarometric data and modeling of the topography, *J. Geophys. Res.*, *115*, B06407, doi:10.1029/2008JB006126.

1. Introduction

[2] The steep front of the High Himalaya is a striking feature of the morphology of the Himalayan mountain range (Figure 1). It defines the physiographic boundary between the Lesser and High Himalaya [*Gansser*, 1964]. A number of studies indicate that it coincides with locally higher rock uplift and exhumation rates, as well as intense microseismic activity attesting of a tectonic origin, possibly resulting from some coupling between crustal deformation and surface erosion [e.g., *Hodges et al.*, 2004; *Avouac*, 2007, and references therein]. For example, the pattern of river incision across the Himalaya of central Nepal exhibits a zone with high incision rates, reaching up to 5 ± 1.2 mm yr^{-1} [*Lavé and Avouac*, 2001; *Garzanti et al.*, 2007], that coincides with the front of the High Himalaya. This zone also corresponds to a region from where particularly young thermochronological ages have been reported (Figure 2) [*Harrison et al.*, 1998; *Coleman and Hodges*, 1998; *Catlos*, 2000; *Burbank et al.*, 2003; *Bollinger et al.*, 2004a; *Hodges et al.*, 2004; *Wobus et al.*, 2003; *Huntington et al.*, 2006; *Huntington and Hodges*, 2006; *Blythe et al.*, 2007].

[3] The fact that the High Himalayan front is linear rather than indented by the main rivers is a clear indication that incision is compensated by locally higher rock uplift rate [*Lavé and Avouac*, 2001; *Robl et al.*, 2008]. This zone of locally higher uplift and erosion rates could reflect (1) thrusting over a midcrustal ramp [e.g., *Gansser*, 1964; *Cattin and Avouac*, 2000; *Lavé and Avouac*, 2001] (Figures 2 and 3); (2) the growth of a Lesser Himalaya duplex at midcrustal depth [e.g., *Schelling and Arita*, 1991; *DeCelles et al.*, 2001; *Robinson et al.*, 2003; *Avouac*, 2003; *Bollinger et al.*, 2004a, 2006] (Figure 3b); or (3) out-of-sequence thrusting along the front of the High Himalaya [e.g., *Harrison et al.*, 1998; *Hodges et al.*, 2004; *Wobus et al.*, 2003] (Figure 3c). Note that points 1 and 2 are intimately linked since the duplex may have developed because of an underlying ramp and ramp overthrusting. In any case, some transfer of material from the underthrusting Indian crust to the Himalayan wedge (a process that we call here "underplating") is definitely needed over longer timescales to account for the growth of the orogenic wedge. A number of kinematic models involving some component of underplating and with or without out-of-sequence thrusting at the front of the High Himalaya might be possible a priori. It has already been shown that the duplex model is compatible with the available thermochronological and thermometric data available at the time for the Himalaya of central Nepal [*Bollinger et al.*, 2006]. However, this previous study did not explore fully the range of possible kinematic models, nor the range of possible thermal parameters, such as radiogenic heat production and shear heating. In a recent study, *Whipp et al.* [2007] and *Wobus et al.* [2006] focused on the analysis of low-temperature thermochonological data in the High Himalaya and concluded that, considered alone, such data are insufficient to discriminate among these various models of crustal deformation. It is thus clear that discriminating the various models that have been proposed probably require a more global analysis of thermometric, barometric and thermochronological data not only from the High Himalaya but also from the Lesser Himalaya, an approach that is taken in this study.

[4] Determining the contribution of out-of-sequence thrusting to the strain budget across the Himalaya is important with regard to seismic hazard. The seismic hazard posed by out-of-sequence thrust faults is indeed poorly known and earthquakes on high-angle splay faults within the Himalaya could certainly be devastating. From a more fundamental perspective, determining the contribution of out-of-sequence thrusting is important because this is one possible response of an orogenic wedge to a locally higher erosion rate [*Hodges et al.*, 2004; *Avouac*, 2007] and it can help test the channel flow model recently propounded by *Beaumont et al.* [2001, 2004] and *Hodges et al.* [2001]. Although the numerical model of *Beaumont et al.* [2001, 2004] includes an important component of underplating, it holds primarily that the Tibetan middle crust is squeezed from beneath the plateau due to a positive feedback between crustal flow and focused erosion along the front of the high range, in turn leading to out-of-sequence thrusting. An alternative model, which also includes some coupling between erosion and crustal deformation but does not require out-of-sequence thrusting, is that locally higher surface erosion would have driven locally faster underplating rate, through the development of a midcrustal duplex [*Avouac*, 2003; *Bollinger et al.*, 2004a, 2006]. This mechanism has in fact been reproduced in analogue experiments [*Konstantinovskaia and Malavieille*, 2005; *Bonnet et al.*, 2007].

[5] This study aims at exploring more widely than previous studies the range of possible thermokinematic models in view of the rather dense thermochronological (low and high temperatures) and thermobarometric data available from the Himalaya of central Nepal (Figure 1). The study is based on new ^{40}Ar/^{39}Ar and fission track (FT) data from the Kathmandu nappe and new (U-Th)/He data from the Palung area south of the Kathmandu basin which are presented hereafter. These data are analyzed jointly with a broad set of thermometric, barometric and thermochronological data compiled from the literature. We adopt the approach described by *Herman et al.* [2007a], who use a thermokinematic model, PECUBE [*Braun*, 2003; *Herman et al.*, 2007a], to perform a formal nonlinear inversion of the data, using the Neighborhood Algorithm [*Sambridge*, 1999a, 1999b]. The forward thermokinematic models consider the possibility of either localized thrusting along a single major thrust fault, the Main Himalayan Thrust (MHT), with nonuniform underplating (i.e., including a zone along the MHT where underplating is more pronounced) leading to duplexing or out-of-sequence thrusting in addition to thrusting along the MHT with uniform underplating. Finally, we combine the thermokinematic model with a landscape evolution model to assess to which extent the proposed kinematics can explain the morphology of the

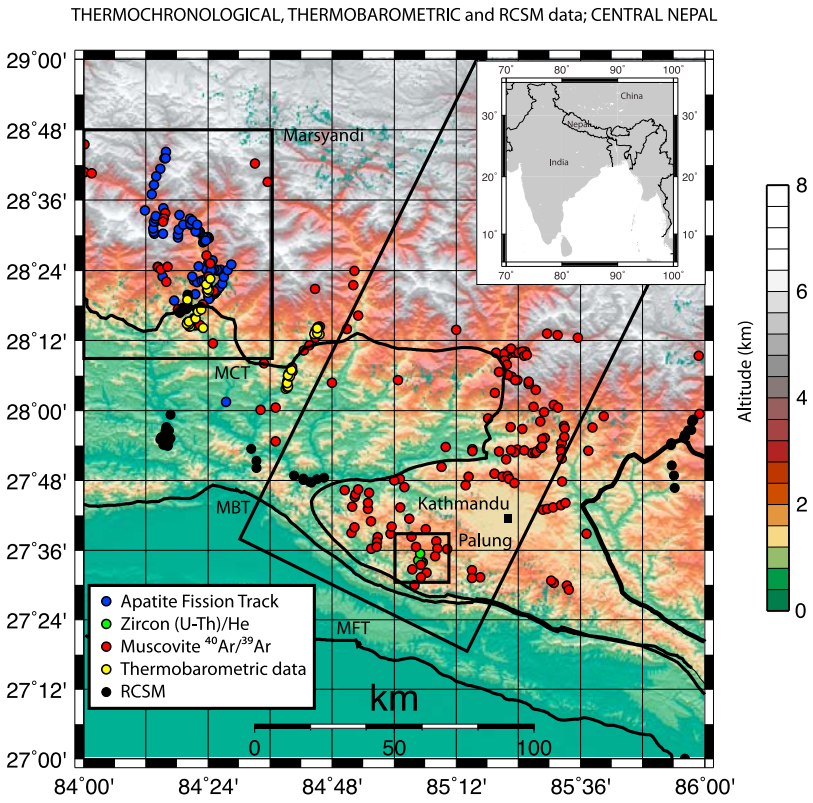

Figure 1. Compiled thermochronological and thermobarometric data. Shaded relief map derived from a digital elevation model (Shuttle Radar Topography Mission, U.S. Geological Survey) of central Nepal Himalaya. Inset shows the regional map. The dots depict the location of compiled data: blue, apatite FT data;, red, muscovite $^{40}Ar/^{39}Ar$; green, zircon (U-Th)/He; yellow, thermobarometric data; black, Raman Spectroscopy of Carbonaceous Material (RSCM) data. Refer to text for references. Main Front Thrust (MFT), Main Boundary Thrust (MBT), and Main Central Thrust (MCT) are highlighted by the black lines. The black boxes show regions extracted in Figure 5a for the Marsyangdi River catchment, Figure 7 for the Palung area, and Figure 20g (in which CASCADE model predictions are compared to the actual topography).

range. In addition to shedding light on the kinematics of crustal deformation, our study also brings constraints on the thermal structure of the Himalaya and thermal properties of the Himalayan rocks.

2. Geologic and Geomorphic Constraints

[6] In this section, we outline the general geologic and geomorphic setting, only emphasizing aspects that are most appropriate for this study. Our interest is the thousand year to million year timescale over 15 Myr. Further details are presented in recent reviews [e.g., *Yin*, 2006; *Avouac*, 2007].

2.1. Regional Setting

[7] The Himalayan arc and Tibetan Plateau are the results of convergence between India and Asia [*Powell and Conaghan*, 1973]. Since the onset of collision 60 to 40 Ma, India has indented ~3000 km into Asia, causing lateral extrusion and crustal shortening [e.g., *Molnar and Tapponnier*, 1975] to create the highest topography currently observed on Earth.

[8] The Himalayan fold and thrust belt is commonly divided into four lithotectonic units, separated by broadly east-west trending major faults [e.g., *Gansser*, 1964; *LeFort*, 1975]. From south to north, these are the Siwalik Molasse (SM), the Lesser Himalayan Series (LHS), the High Himalayan Crystalline (HHC) and the Tethyan Himalayan Series (THS). The SM comprise foreland deposits today incorporated into the hanging wall of the Main Frontal Thrust (MFT). The LHS is a sequence of metamorphic siliciclastic and carbonate rocks separated from the SM by the Main Boundary Thrust (MBT). The higher-grade metamorphics of the HHC are exposed between the Main Central Thrust zone (MCT) and a normal fault called the North Himalayan Fault [*Burg et al.*, 1984] or the South Tibet Detachment fault (STD) [*Burchfiel et al.*, 1992]. The STD juxtaposes the THS over the HHC. The MCT zone is a shear zone of variable thickness (up to 3 km) which parallels metamorphic isograds and juxtaposes units with different geochemical characteristics. As a result, there exist some variations in the literature with regard to its exact definition [e.g., *Searle et al.* 2008]. At depth, the MFT is interpreted to merge with the MBT and the MCT to form a south verging décollement [e.g., *Schelling and Arita*, 1991; *Hauck et al.*, 1998] (Figure 2). This décollement extends 150–200 km to the north and is usually referred as the Main Himalayan Thrust (MHT) for consistency with the name assigned to its downdip continuation beneath southern Tibet [*Zhao et al.*,

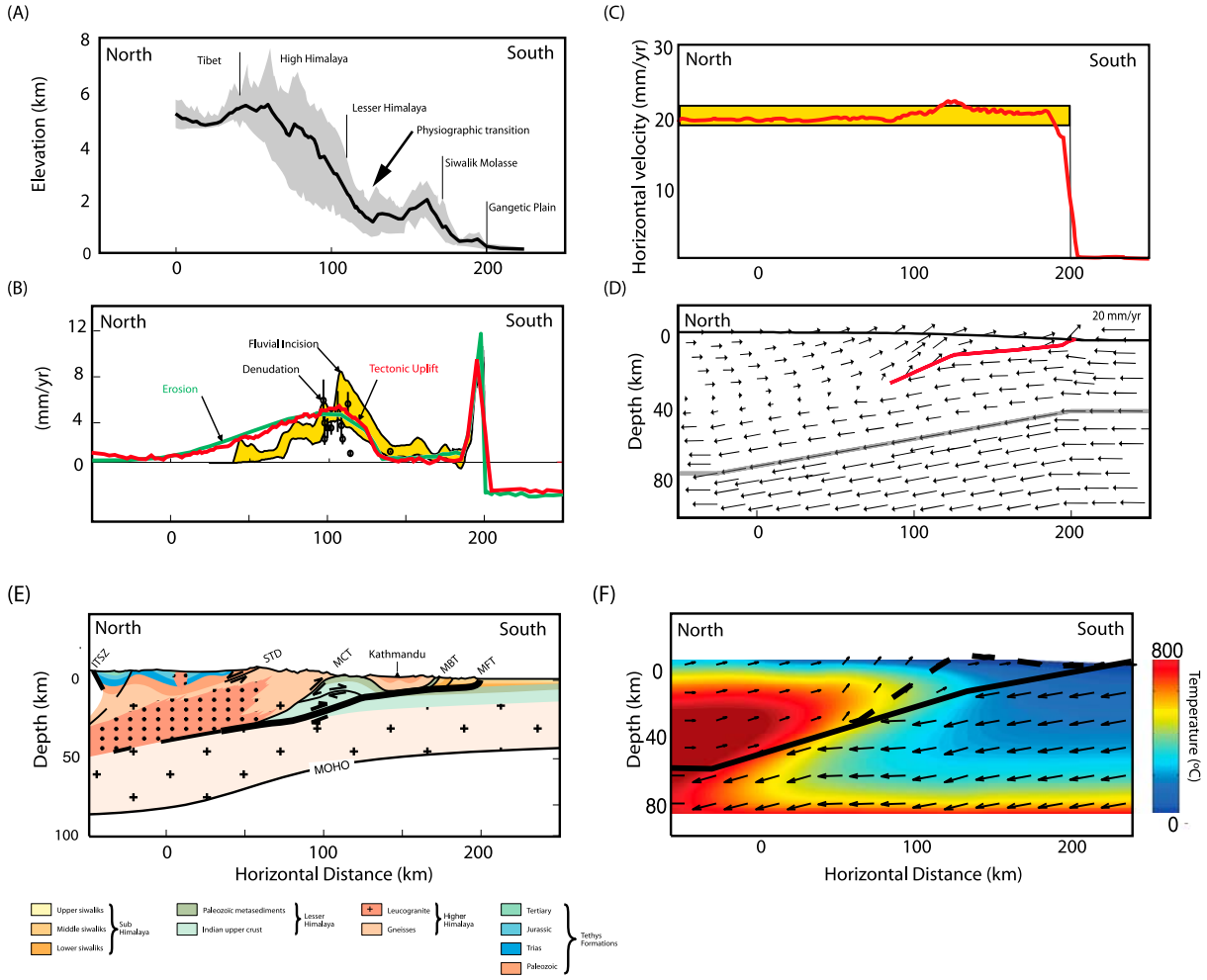

Figure 2. (a) Mean and maximum elevation within a 50 km swath in central Nepal (modified from *Lavé and Avouac* [2001]). Note the location of the physiographic transition. (b) Predicted uplift and erosion rates [*Cattin and Avouac*, 2000] compared to incision rates from *Lavé and Avouac* [2001] and denudation rate derived using apatite FT dating [*Burbank et al.*, 2003]. (c) Horizontal velocity of Asia relative to India as derived from slip on the Main Himalayan Thrust (MHT) [*Cattin and Avouac*, 2000]. (d) Velocity predicted from a numerical model [*Cattin and Avouac*, 2000]. (e) Geological section across central Nepal Himalaya at the longitude of Kathmandu. The thick line shows the MHT, which reaches the surface at the front of the Siwalik Hills where it coincides with the Main Front Thrust (MFT). The Main Boundary Thrust fault (MBT) separates Lesser Himalaya metasediment sequence (LHS) from the molasse deposits of the sub-Himalaya (the Siwalik Hills). The Main Central Thrust (MCT) fault places the higher-grade metamorphic rocks of the High Himalayan Crystalline units (HHC) over the LHS. ITSZ, Indus-Tsangpo Suture Zone; STD, South Tibet Detachment fault. (f) Thermal structure predicted from a numerical model (this study) and velocity field for the duplex model (see text for details).

1993]. The MCT, MBT and MFT and the intervening thrust faults are generally thought to have formed as a forward propagating sequence of thrusting [e.g., *LeFort*, 1975].

2.2. Topography and Erosion Patterns

[9] One major geomorphic characteristic of the Himalaya is the presence of a topographic break ~75–100 km north of the MFT which coincides approximatively with the location of the MCT zone (Figure 2a). *Lavé and Avouac* [2001] observed that river incision during the Holocene does not exceed about 1 mm yr^{-1} south of the physiographic transition and increases abruptly at the front of the high range to ~4–8 mm yr^{-1} (Figure 2b). It is worth stressing that river incision rate is not necessarily equal to erosion rate or uplift rate. Rapid exhumation within this zone is consistent with the very young cooling ages [e.g., *Arita and Ganzawa*, 1997; *Burbank et al.*, 2003; *Blythe et al.*, 2007] (Figure 2b). *Wobus et al.* [2005] reported cosmogenic dating of detrital material suggesting low erosion rates between 0.2 and 0.8 mm yr^{-1} south of the MCT at a thousand year timescale, which are at odds with other longer-term estimates and could reflect temporal variations of erosion rates at the thousand year timescale. We focus here on the longer timescale and therefore ignore these data. It is worth noting that the zone of rapid river down cutting is about 50 km wide and the transition from low to high rates coincides with the front of the

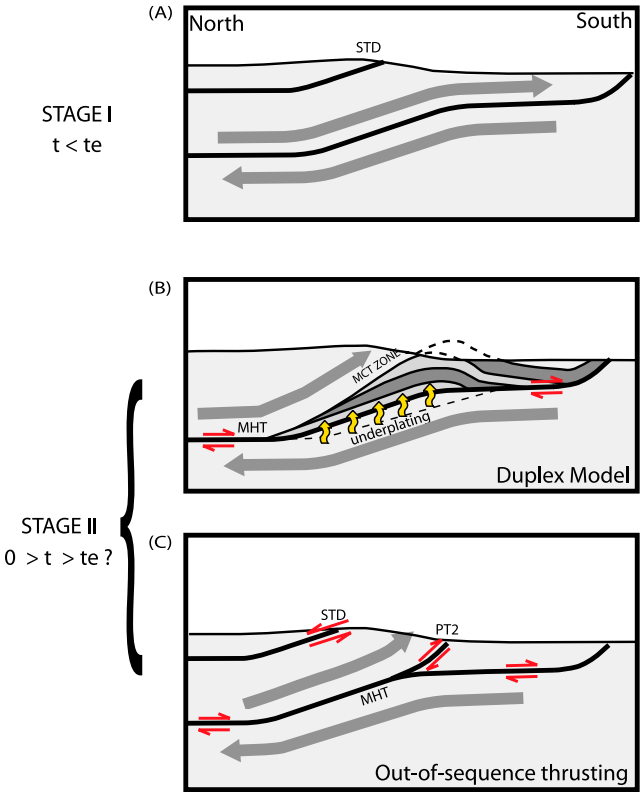

Figure 3. Simplified sketch of the kinematics discussed in this study. (a) Overthrusting and underthrusting along the MHT until t_e. (b) Duplex formation model from t_e to present day. (c) Out-of-sequence thrusting at the physiographic transition.

high range but not necessarily with any lithological transition. In fact, the steep wall gorges observed in the High Himalaya persist in the Lesser Himalaya rocks.

2.3. Geometry of the Main Himalayan Thrust

[10] Some idea of the structure of the crust across central Nepal can be derived from geophysical observations and surface geology. The frontal part of the system is relatively well constrained from balanced cross sections across the Siwalik fold-and-thrust belt and some, gravity and magnetotelluric data [e.g., *Schelling and Arita*, 1991; *Mugnier et al.*, 1999; *Lemonnier et al.*, 1999; *Lavé and Avouac*, 2000; *Hetényi et al.*, 2006]. These data show that the MFT, the MBT and the intervening thrust faults all root into a 5–7 km deep décollement at the top of the underthrusted Indian basement (Figure 2e). The décollement probably extends beneath the Higher Himalaya, as indicated from a zone of high conductivity; which could correspond to sediments dragged along the décollement [*Lemonnier et al.*, 1999]. This décollement probably connects with the major shallow dipping reflector that has been imaged from various seismological experiments in Southern Tibet [*Hirn and Sapin*, 1984; *Zhao et al.*, 1993; *Brown et al.*, 1996; *Nelson et al.*, 1996] and across the Himalaya of eastern Nepal [*Schulte-Pelkum et al.*, 2005]. This décollement constitutes the sole of the Himalayan wedge and is called here the MHT for consistency with the terminology described above. How the décollement beneath the Lesser Himalaya, which lies at depth of 7 to 10 km, connects with the décollement beneath southern Tibet at a depth of about 35–40 km, is more enigmatic.

[11] In the auxiliary material we present structural measurements which document the broad antiform depicted, in the study area, by the foliation across the Lesser Himalaya.[1] This antiform, the Pokhara-Gorkha anticlinorium, which has been noticed in a number of previous studies [e.g., *Heim and Gansser*, 1939; *Brunel et al.*, 1979; *Brunel and Kienast*, 1986; *Pêcher*, 1989] suggests some duplex [*Schelling and Arita*, 1991; *DeCelles et al.*, 2001; *Robinson et al.*, 2003; *Avouac*, 2003; *Bollinger et al.*, 2004a, 2006] associated with a ramp, as illustrated in Figure 2e. Direct geophysical observation for that ramp is however scant [*Pandey et al.*, 1995; *Lemonnier et al.*, 1999; *Schulte-Pelkum et al.*, 2005].

[12] The geometry of the MHT seems to be characterized by a ramp and flat geometry (Figure 2e). The southernmost flat segment is shallow, extends over a width of 70–80 km long and reaches the surface along a 30 ramp, where it coincides with the MFT. The midcrustal ramp has been inferred to dip by about 15 from the focal mechanisms of local earthquakes and the pattern of uplift [*Cattin and Avouac*, 2000].

2.4. Shortening Rates

[13] Shortening rates across the whole range have been estimated using various methods, spanning over different timescales. A number of studies have focused on determining the current shortening rate across the Nepal Himalaya from geodetic measurements [*Bilham et al.*, 1997; *Jouanne et al.*, 1999; *Larson et al.*, 1999; *Jouanne et al.*, 2004; *Bettinelli et al.*, 2006]. The most recent study indicates 19 ± 2.5 mm yr^{-1} of shortening across central Nepal [*Bettinelli et al.*, 2006]. This rate compares well with the 21.5 ± 2 mm yr^{-1} slip rate on the MFT determined from deformed Holocene terraces in the sub-Himalaya south of Kathmandu basin [*Lavé and Avouac*, 2000]. This is consistent with a model in which the only significant active thrust across that segment of the Himalaya is the MHT. This kinematic framework can be reproduced in numerical mechanical models provided that the friction on the MHT is low enough (Figures 2c and 2d) [*Cattin and Avouac*, 2000].

[14] Some idea of the long-term shortening rate across the Himalaya can be derived from the southward migration of proximal facies in the foreland [*Lyon-Caen and Molnar*, 1983]. This rate, which is estimated to between 13 and 19 mm yr^{-1} over the last 15 to 20 Myr [*Mugnier and Huyghe*, 2006], compares well with the 10–20 mm yr^{-1} rate deduced from the sedimentation rate determined from magnetostratigraphic sections in the sub-Himalaya of central Nepal [*Appel et al.*, 1991; *Harrison et al.*, 1993] given the dip angle of the Indian basement and geometry of foreland basin [*Lavé*, 1997; *Avouac*, 2003; *Hetényi et al.*, 2006]. This quantity is not directly a measure of the shortening rate since it does not account for the erosion of the advancing topographic front of the range [*Avouac*, 2003]. It is rather a measure of the rate at which the Indian basement is thrusted under the range and might therefore be called the "under-

[1] Auxiliary material data sets are available at ftp://ftp.agu.org/apend/jb/2008jb006126. Other auxiliary material files are in the HTML.

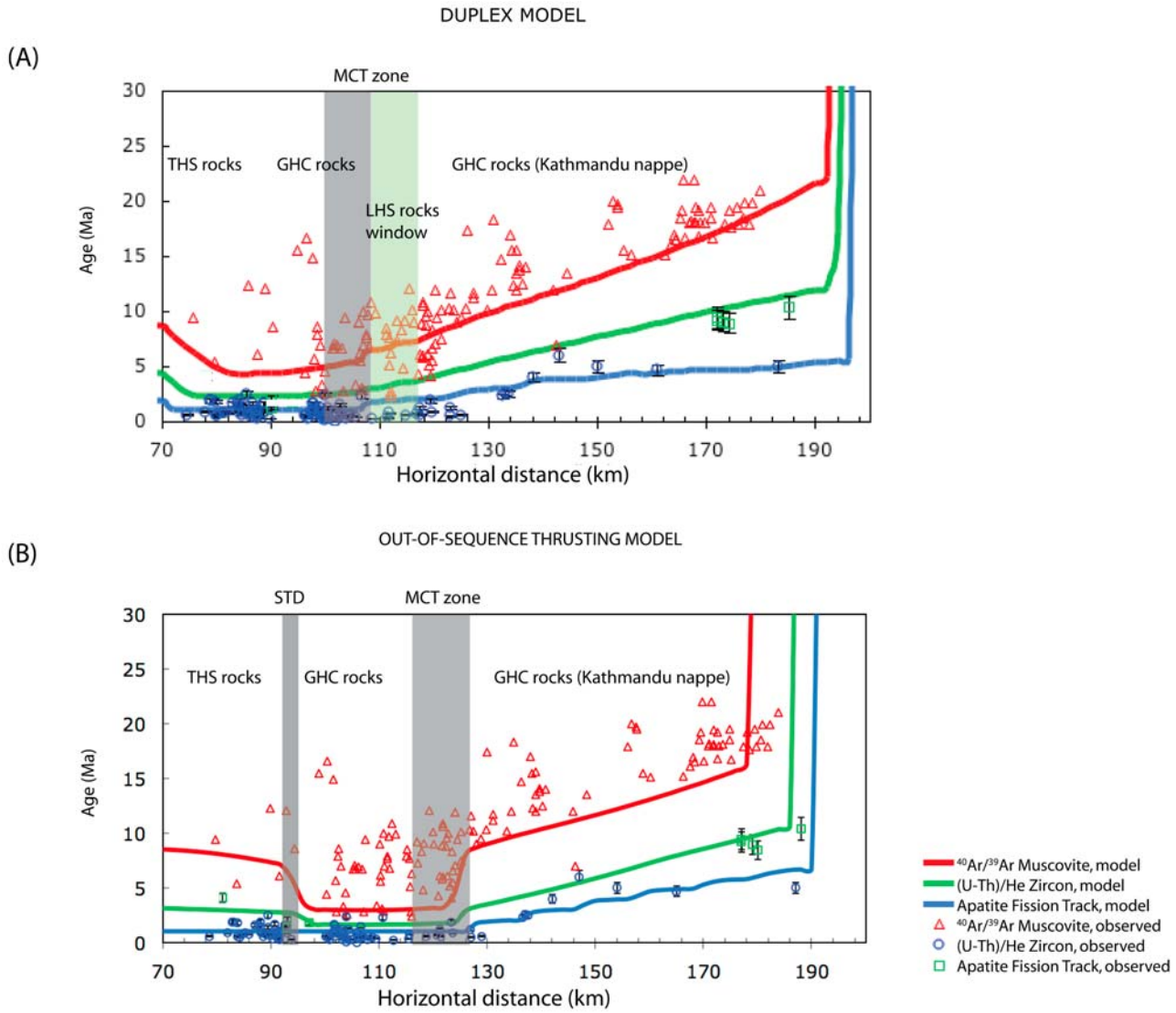

Figure 4. (a) Simulated thermochronological ages versus horizontal distance for a good fitting model for the duplex model (model 1, Table 5) compared to the actual data. Solid lines represent model predictions. Scatter triangles and dots depict data. Red is associated with $^{40}Ar/^{39}Ar$ in muscovite, green is associated with (U-Th)/He in zircon, and blue is associated with apatite FT. STD and MCT zones are highlighted by the grey areas. THS, Tethyan Himalayan Series; GHC, Greater Himalayan Crystalline. The green area is related to the LHS exposed in the footwall of the MCT, as predicted by the model. (b) Same as Figure 4a but for the out-of-sequence thrusting model (model 7, Table 5).

thrusting rate" [*DeCelles and Decelles*, 2001]. The horizontal gradient of thermochronological ages can be used to estimate the rate of overthrusting (which is equal to erosion rate if the topography is at steady state and using an Eulerian frame of reference) [*Avouac*, 2003]. A simple linear regression across the data set available at the time indicates a value of 4–5 mm yr^{-1} [*Avouac*, 2003; *Bollinger et al.*, 2004a]. The total rate of convergence, the sum of the underthrusting and overthrusting rates, yields a value of 20 mm yr^{-1}, close to that estimated from orogen-scale balanced cross section [*Schelling and Arita*, 1991; *Srivastava and Mitra*, 1994; *DeCelles and Decelles*, 2001; *Mugnier and Huyghe*, 2006; *Robinson et al.*, 2006]. Assuming that most of the deformation is accommodated on the MHT, the shortening rate seems to have been relatively steady, around 20 mm yr^{-1}, over the last 15–20 Myr.

2.5. Radiogenic Heat Production and Thermal Conductivity

[15] Some idea of the thermal characteristics of the underthrusting Indian crust might be inferred from heat flow measurements and from in situ and laboratory measurements of radiogenic heat production of rocks collected at the surface or in boreholes. The low value of the heat flow over the Indian Shield of *Roy and Rao* [2000] requires a relatively low radiogenic heat production of 0.8 $\mu W\ m^{-3}$ on average for the underthrusting Indian crust.

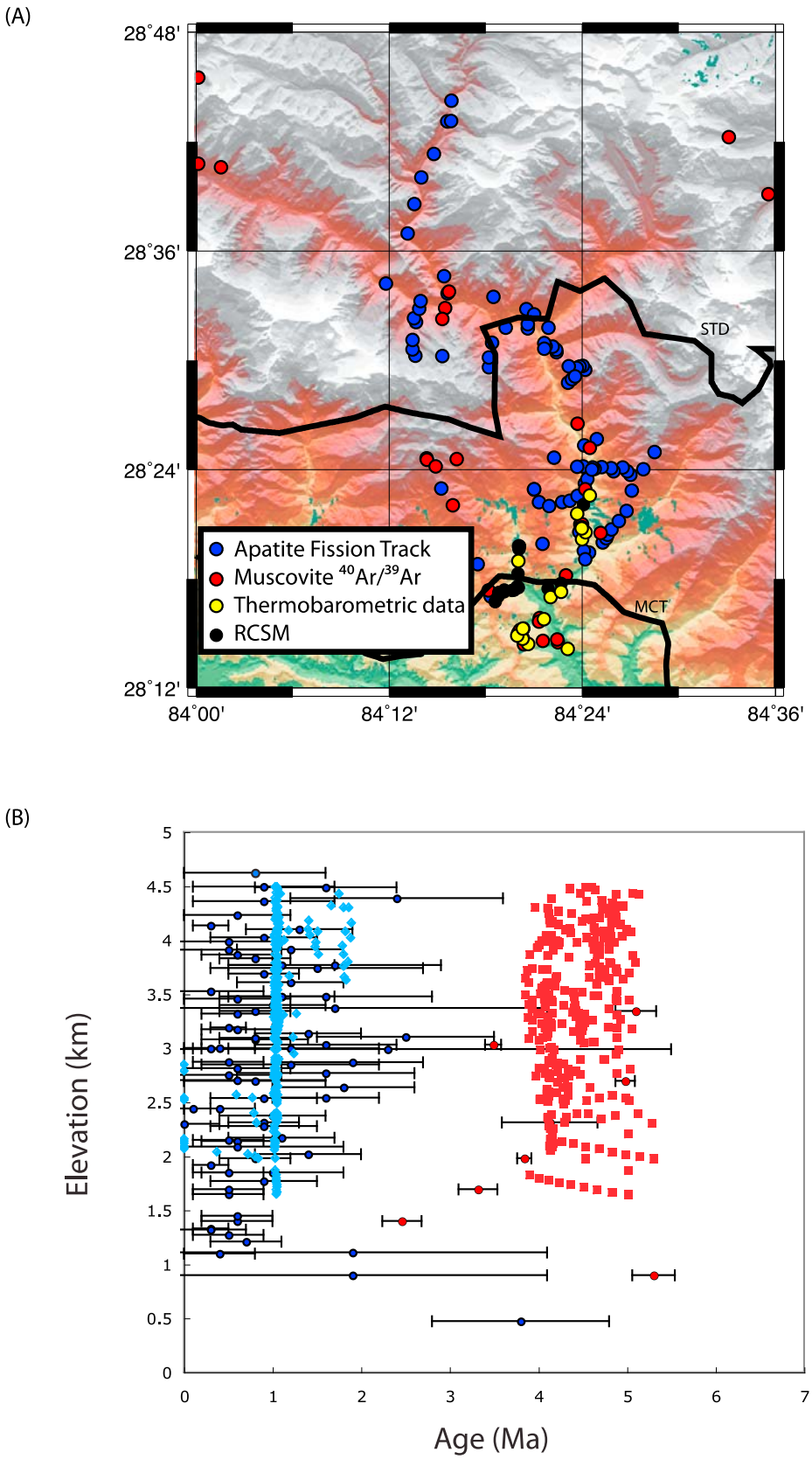

Figure 5. Thermochronological and thermobarometric data in the Marsyangdi River catchment. (a) Shaded topography and data extracted from Figure 1. (b) Age-elevation plot for apatite FT (blue) and muscovite $^{40}Ar/^{39}Ar$ (red) shown in Figure 5a. Symbols with error bars are data, and symbols with no error bar are model predictions from CASCADE/PECUBE coupled model.

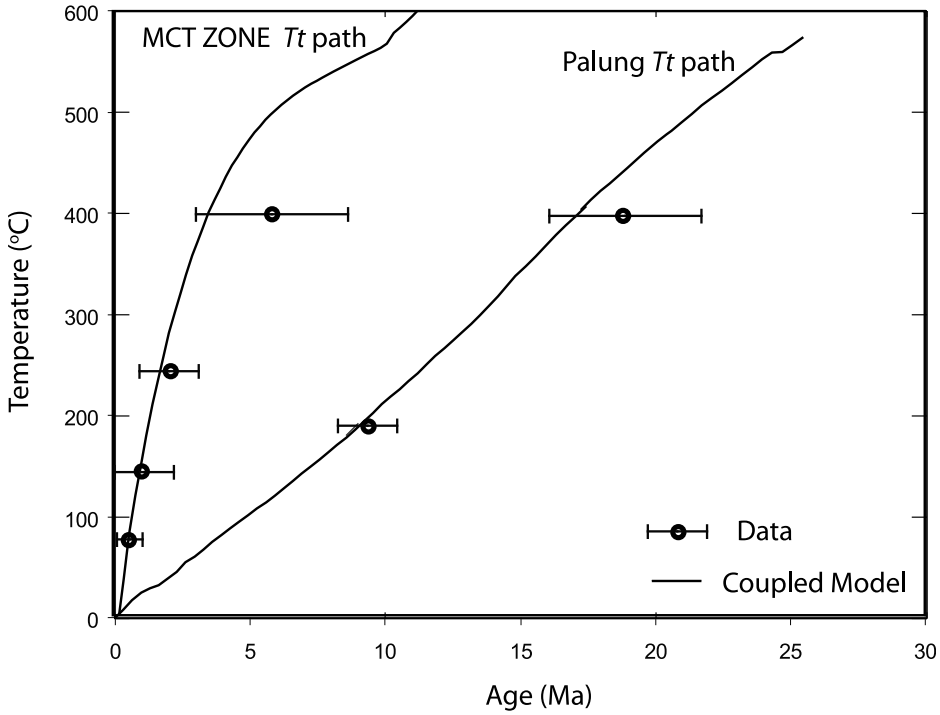

Figure 6. Age versus temperature for rocks exposed in the Palung area and within the MCT zone (rock structurally above the modeled MCT, as defined by the evolving sheet lying above the MHT at the beginning of the model simulation). The dark lines are *T-t* paths predicted from the duplex model in two dimensions, and dots with error bars are derived from the compiled data set.

[16] Few studies have focused on the thermal properties of Himalayan rocks. The abundance of K, U, and Th in granitic and gneissic rocks within the Indian Shield show evidence for some variability in radiogenic heat production reaching locally values as high as 1.5 to 5.5 μW m^{-3} [*Menon et al.*, 2003]. Values of radiogenic heat production based on measurements of K, U and Th for High Himalaya Crystalline rocks span between 1.5 and 6.0 μW m^{-3}, and cluster around 4 μW m^{-3} [e.g., *England et al.*, 1992; *Whipp et al.*, 2007]. The sedimentary rocks of the THS, are commonly assigned a radiogenic heat production of about 0.5 μW m^{-3} [e.g., *Bollinger et al.*, 2006; *Brewer and Burbank*, 2006; *Whipp et al.*, 2007].

[17] We are not aware of any systematic study of thermal conductivity of rocks in the Nepal Himalaya, but we rely on the study of *Ray et al.* [2007], who measured the thermal conductivity of the major rock formations of the Garhwal Himalaya. Seventy-three rock samples including gneiss, metabasic rock and quartzite were measured using a steady state divided bar method, and yielded values between 1.5 and 3.5 W m^{-1} K^{-1} (except for a quartzite which yielded much higher values between 4 and 8 W m^{-1} K^{-1}), with a mean value of about 2.5 W m^{-1} K^{-1}.

3. Thermochronological and Thermobarometric Data

3.1. Compiled thermochronological data

[18] Thermochronological methods can be used to constrain thermal histories of rocks since they record the time elapsed since a rock went through a given closure temperature window. A wide range of thermochronometric systems of different closure temperatures have been applied in the LHS and the HHC series (Figure 1), on bedrock rock samples as well as on detrital samples (which we do not model directly): ^{40}Ar/^{39}Ar in muscovite [*Copeland et al.*, 1991; *Macfarlane et al.*, 1992; *Macfarlane*, 1993; *Arita et al.*, 1997; *Coleman and Hodges*, 1998; *Catlos*, 2000; *Hodges et al.*, 2004; *Bollinger et al.*, 2004a; *Huntington and Hodges*, 2006], FT in zircon and apatite [*Arita and Ganzawa*, 1997; *Burbank et al.*, 2003; *Blythe et al.*, 2007] (Figures 1 and 4). Some ages have also been obtained from in situ Th-Pb dating of monazite [*Harrison et al.*, 1997a; *Rai et al.*, 1998; *Catlos et al.*, 2001, 2002; *Kohn et al.*, 2001]. Some debate exists regarding whether these dates reflect retrograde monazite growth or are a mix of prograde and retrograde dates [e.g., *Bollinger and Janots*, 2006; *Martin et al.*, 2007]. These data are therefore not considered in this study.

[19] Locally, some sparse ^{40}Ar/^{39}Ar cooling ages on biotite have been acquired [e.g., *Edwards et al.*, 1996; *Rai*, 1998]. However, although the closure temperature of muscovite is usually higher than that of biotite, muscovite yields the youngest ^{40}Ar/^{39}Ar age in the Himalaya [*Edwards et al.*, 1996; *Macfarlane*, 1993; *Bollinger and Janots*, 2006]. This inversion is common in the Himalayan setting and has been discussed in previous papers [e.g., *Stüwe and Foster*, 2001]. It may reflect late muscovite crystallization in a fluid-rich shear zone, a scenario plausible for some very young samples acquired at the top of the MCT zone according, among other arguments, to the textural relationship between the minerals. However, it may also reflect excess Ar in biotite

Table 1. The $^{40}Ar/^{39}Ar$ Muscovite Data[a]

Sample	Longitude	Latitude	Weight (mg)	Preferred Age	1σ (Ma)	Steps Used[b]	Percent of Gas	Method[c]
BE320	85.124	27.581	7.7	<20				
BE327	85.117	27.556	6.3	<40				
BE333	85.071	27.531	7.1					
HT-11	85.049	27.472		20.8	±0.1	D-L	94	I
KN029	85.472	27.907	2.8	9.6	±0.1	A-I	99	P
KN029			30.0	9.6	±0.2	B-J	94	P
Average				9.6	±0.1			
KN041	85.480	27.986	6.0					
KN067	85.452	28.050	3.1	7.0	±0.1	C-K	86	P
KN071	85.412	28.071	9.5	7.8	±0.1	4-10	94	P
KN080	85.445	28.000	21.0	5.1	±0.4	B-I	90	I
KN100	85.353	27.846	8.0	12.3	±0.2	E-K	84	P
KN100			34.3	11.7	±0.4	A-J	98	P
				12.1	±0.2			
KN109	85.313	27.801	9.1	12.0	±0.1	D-J	80	P
KN109			34.0	12.4	±0.5	B-J	91	P
Average				12.1	±0.1			
KN217	85.318	28.039	34.0	12.1	±0.1	E-I	79	P
KN237	85.294	27.965	3.2	11.6	±0.1	E-J	82	P
KN244	85.368	27.940	4.6	7.5	±0.1	D-L	96	P
KN250	85.407	27.936	4.9	8.3	±0.1	D-I	63	P
KN270	85.536	27.849	3.2	11.9	±0.1	B-I	82	P
Average				9.8	±0.1			
KN272	85.266	27.496	4.4	22.0	±0.2	B-I	74	P
KN295	84.818	27.747	3.1	19.7	±0.2	C-J	86	P
KN295			62.9	19.2	±0.3	B-K	89	P
Average				19.5	±0.2			
KN299	84.999	27.781	4.6	16.6	±0.2	C-I	64	P
KN299			34.1	16.5	±0.3	B-J	84	P
Average				16.6	±0.1			
KN301	85.015	27.758	4.8	15.1	±0.2	C-K	94	P
KN427	85.228	27.791	30.0	12.0	±0.2	A-J	100	I
KN436	85.218	27.767	27.1	13.5	±0.3	A-K	100	P
KN440	85.549	27.718	19.3	14.2	±0.2	A-J	100	P
KN441	85.534	27.712	21.6	18.5	±0.5	A-J(E)	98	I
KN441			27.7	19.2	±0.3	B-J	95	P
Average				18.9	±0.3			
KN443	85.559	27.729	31.4	13.5	±0.3	B-H	98	P
KN445	85.564	27.760	24.1	17.1	±0.3	A-J	96	I
KN450	85.568	27.764	27.1	13.7	±0.4	A-I	87	I
KN455	85.559	27.779	26.9	38.8	±0.5	F-J	69	P
KN459	85.537	27.782	24.4	17.2	±0.3	D-J	88	P
KN461	85.379	27.775	31.0	12.0	±0.3	B-J	95	P
KN462	85.357	27.779	25.2	12.0	±0.2	A-J	93	I
KN463	85.363	27.788	30.2	12.9	±0.2	A-J	94	I
KN471	85.506	27.795	32.0	13.2	±0.2	A-M	100	I
KN517	85.625	27.874	28.0	7.3	±0.2	A-H	74	P
KN521	85.641	27.944	35.3	5.6	±0.4	B-J	95	I
KN527	85.679	27.972	21.0	7.1	±0.4	E-J	70	I
KN665	85.535	27.871	5.8	8.8	±0.1	B-I	97	P
KN666	85.533	27.878	5.7	8.9	±0.1	C-I	74	I
KN667	85.539	27.896	22.1	10.1	±0.3	C-J	92	P
KN668	85.547	27.914	25.6	8.3	±0.1	A-L	100	I
KN669	85.548	27.939	25.6	7.7	±0.2	B-J	99	P
KN670	85.545	27.945	23.5	7.9	±0.3	C-K	98	I
KN671	85.540	27.951	5.2	8.6	±0.5	F-J	80	P
KN672	85.534	27.961	19.0	8.8	±0.2	A-K	100	I
KN674	85.529	27.974	5.8	11.2	±0.8	C-H	83	P
KN674			6.5	7.8	±0.1	C-J	97	P
Average				8.2	±0.1			
KN675	85.527	27.987	6.8	8.2	±0.2	F-K	88	P
KN677	85.525	28.000	11.0	7.1	±1.8	D-I	57	I
KN677			4.8	7.2	±0.2	E-J	94	P
Average				7.1	±0.2			
KN679	85.512	28.008	5.6	7.9	±0.1	B-H	90	P
KN689	85.467	27.959	15.0	9.1	±0.3	A-J	99	I
KN690	85.482	27.910	2.8	11.6	±0.2	C-I	94	P
KN693	85.473	27.885	30.0	9.6	±0.2	C-J	93	P
KN694	85.467	27.880	5.2	10.8	±0.2	B-J	97	P
KN695	85.454	27.869	5.3	10.3	±0.2	C-J	90	P
KN696	85.449	27.865	5.9	10.2	±0.2	A-J	100	P
KN697	85.438	27.865	5.6	9.0	±0.1	B-M	95	P

Table 1. (continued)

Sample	Longitude	Latitude	Weight (mg)	Preferred Age	1σ (Ma)	Steps Used[b]	Percent of Gas	Method[c]
KN698	85.411	27.874	22.3	9.4	±0.3	B-K	93	P
KN701	85.396	27.870	5.5	9.9	±0.1	B-J	97	P
KN702	85.390	27.874	5.4	10.3	±0.1	E-J	73	P
KN703	85.380	27.866	30.0	11.0	±0.2	B-L	99	P
KN704	85.369	27.873	5.3	11.7	±0.1	A-M	100	I
KN707	85.329	27.867	4.9	11.4	±0.2	A-L	97	I
KN709	85.241	27.874	29.0	17.1	±0.2	E-J	73	P
KN710	85.239	27.868	4.7	64.7	±0.5	E-K	74	P
KN714	85.154	27.879	24.3	<225				P
KN723	85.427	28.068	3.5	10.9	±0.1	E-M	95	P
KN724	85.408	28.081	3.7	10.1	±0.1	A-J	100	I
KN731	85.372	28.087	31.0	12.2	±0.4	A-K	100	I
KN731			5.1	12.0	±2.0	B-G	98	P
KN731			5.9	6.8	±0.3	B-I	99	I
Average				7.5	±0.3			
KN732	85.359	28.091	4.3	11.2	±0.1	A-I	98	I
KN733	85.347	28.097	6.8	6.8	±0.1	A-M	96	I
KN734	85.330	28.101	6.9	8.5	±0.1	AB-AI	91	P
KN735	85.324	28.107	25.0	9.8	±0.2	E-I	89	P
KN736	85.314	28.100	3.4	4.9	±0.2	B-J	89	P
KN737	85.307	28.093	4.5	5.8	±0.4	A-I	98	P
KN738			5.2	13.4	±0.2	A-H	83	P
KN739			31.0	9.3	±0.1	A-L	100	I
KN740	85.379	27.793	5.4	12.5	±0.1	A-I	75	I
KN742	85.417	27.758	7.9	14.1	±0.1	B-I	86	P
KN743	85.340	27.793	5.7	13.6	±0.1	D-K	90	P
KN745	85.473	27.698	4.8	14.1	±0.1	B-I	95	P
KN746	85.488	27.701	6.1	14.6	±0.1	B-H	94	P
KN748	85.508	27.705	26.6	15.5	±0.2	A-K	100	I
KN753	85.618	27.631	25.5	15.3	±0.2	A-J	99	P
KN864	85.071	27.495	7.7	22.5	±0.5	B-K	93	P
KN865	85.090	27.506	8.6	17.6	±0.2	C-J	95	P
KN870	84.893	27.554	7.9	20.2	±0.2	A-J	98	P
KN873	84.904	27.566	7.2	<25				
KN876	84.907	27.577	7.0	19.9	±0.2	E-I	59	P
KN880	84.854	27.735	6.3	15.2	±0.1	D-J	93	P
KN881			8.6	16.4	±0.4	E-L	86	P
KP002	84.899	27.739	5.4	16.9	±0.1	B-E	90	P
KP040	84.895	27.690	8.9	19.6	±0.4	A-F	98	P
KP074	84.848	27.637	7.0	18.9	±0.3	B-I	87	P
KP095	84.840	27.621	6.4	17.6	±0.1	A-G	99	P
KP124	84.924	27.581	6.0	<22				
KP136	84.925	27.597	8.5	<22				
KP145	84.941	27.611	9.9	17.0	±0.4	B-F	97	P
KP159	84.970	27.620	6.6	19.9	±0.3	D-K	82	P
KP216	85.155	27.579	8.9	18.4	±0.1	C-J	87	P
KP238	85.240	27.517	7.8	<18				
KP316	85.121	27.599	8.7	19.1	±0.3	B-K	99	P
KP319	85.072	27.605	7.1	<29				
KP347	85.510	27.484	5.7	19.8	±0.4	A-D	71	P
KP378	85.555	27.476	6.0	<18				
NE04	85.346	28.136	41.7	7.5	±0.2	C-I	98	
NE06	85.366	28.135	5.7	6.4	±0.2	C-I	89	
NE08	85.401	28.145	6.8	7.4	±0.3	E_J	95	P
NE09	85.416	28.162	7.4	6.9	±0.1	B-I	92	P
NE10	85.424	28.169	5.5	6.8	±0.1	C-F	89	P
NE11	85.592	28.203	16.4	12.3	±0.1	B-H	86	P
NE13	85.542	28.209	5.7	12.1	±0.2	C-I	82	P
NE15	85.526	28.211	7.3	8.8	±0.1	D-O	98	P
NE20	85.491	28.214	7.0	7.3	±0.1	D-H	85	P
NE23	85.436	28.191	6.2	7.8	±0.2	F-K	90	P
NE25	85.385	28.158	5.7	6.8	±0.2	G-L	92	P
SR13	85.032	27.666	6.6	<16				
SR34	85.004	27.697	7.1	<19				
SR91	84.843	27.698	8.2	18.1	±0.2	D-I	73	P

[a]Weight, is mass of muscovite used for analysis. Details about analytical procedure can be found in Appendices A and B.
[b]Steps correspond to heating steps detailed in the auxiliary material.
[c]Methods are P, which determines the age using the plateau method, and I, which uses the $^{40}Ar/^{39}Ar$ isochron diagram.

Table 2. Apatite Fission Track Data[a]

Sample	n	Standard Track Density ($\times 10^6$ cm^{-2})	Fossil Track Density ($\times 10^4$ cm^{-2})	Induced Track Density ($\times 10^6$ cm^{-2})	Uranium Content (ppm)	χ^2 Probability (%)	Age Dispersion (%)	Central Fission Track Age (Ma $\pm 1\sigma$)
KN-29	21	1.302 (4581)	5.689 (75)	5.482 (7228)	53	36	4	2.6 ± 0.3
KN-71	19	1.328 (4581)	3.247 (32)	2.523 (2487)	24	62	1	3.3 ± 0.6
KN-80	20	1.354 (4581)	1.933 (17)	3.757 (3304)	35	73	9	1.3 ± 0.3
KN-100	20	1.380 (4581)	2.185 (26)	0.991 (1179)	9	4	57	6.1 ± 1.4
KN-109	20	1.406 (4581)	10.09 (110)	6.214 (6773)	55	57	5	4.4 ± 0.4
KN-237	10	1.431 (4581)	2.339 (10)	2.557 (1093)	22	4	78	2.8 ± 1.2
KN-244	18	1.457 (4581)	4.191 (42)	5.418 (5430)	47	80	0	2.2 ± 0.3
KN-270	17	1.483 (4581)	1.016 (8)	0.715 (563)	6	90	1	4.0 ± 1.4
KN-272	10	1.509 (4581)	16.41 (73)	9.748 (4336)	81	95	0	4.9 ± 0.6
KN-299	20	1.535 (4581)	1.178 (15)	0.697 (887)	6	98	0	5.0 ± 1.3

[a]The variable n is the number of grains counted; χ^2 is probability that single grain ages represent one population. Values in parentheses number of tracks counted to determine the reported track densities. Details about analytical procedure can be found in Appendices A and B.

[*Kelley*, 2002], a scenario implying that the biotite age has no geological significance. We decided to ignore the isolated $^{40}Ar/^{39}Ar$ on biotite cooling ages. The systematic variation of the muscovite ages reported here and previously and the apparent randomness of the biotite ages support this approach.

[20] Recently, *Blythe et al.* [2007] complemented this data set with 82 apatite FT, 7 zircon FT and 7 (U-Th)/He in apatite ages from the MCT zone in the Marsyangdi valley area (Figure 5). These ages are consistent with other data and highlight a zone of very young ages at the bottom of the high range. These data also enable estimation of how cooling ages vary with elevation. The advantage of an age-elevation data set is that the exhumation rate can be determined independently of the thermal gradient [*Braun*, 2002a]. Note however that horizontal advection also contributes to the age-elevation relationship [*Stüwe and Hintermüller*, 2000; *Herman et al.*, 2007a; *Huntington et al.*, 2007]. The data from the Marsyangdi area (Figures 1 and 5a) imply relatively rapid exhumation rate, ≥2–5 mm yr^{-1}, but the scatter is too high to determine well constrained rates if all the data are considered together (Figure 5b). The whole set of thermochonological ages available from the Marsyangdi area do provide a relatively detailed history of the cooling ($T - t$ path) of the MCT zone over the last 6 Myr (Figure 6).

3.2. New Thermochronological Data

[21] In order to complement the existing data set we collected samples from the high range down to the southern edge of the Kathmandu klippe and used a variety of thermochronological techniques (Figure 1). The full details of the analytical techniques can be found in Appendices A and B.

3.2.1. The $^{40}Ar/^{39}Ar$ Data

[22] We report here 114 $^{40}Ar/^{39}Ar$ ages in muscovite with 13 duplicate determinations (Figure 1 and Table 1), which now represents the most complete suite of ages in the HHC assimilated nappes overlying the LHS. These multiple analyses suggest the data are reproducible with an uncertainty of 0.2 to 0.4 Ma (the discrepancy of these duplicate analyses ranged from 0.1 to 0.8 Ma or 1.4 to 6.6% of the mean value); this level of uncertainty is acceptable for our purposes and changes within this magnitude would not affect our interpretation.

[23] The 114 muscovite results reported here are in general agreement with data previously published. Although the methods and standards used in these studies were different than those reported here, a general comparison seems reasonable. On the other hand, if these data are subject to close scrutiny, some might wish to ignore some of these results due to problems with the original analysis or because of the difficulty of comparison (see Appendix A for discussion); rejection of all of these data would make little difference as they represent only 8% of the data. *Macfarlane et al.* [1992] reported three $^{40}Ar/^{39}Ar$ muscovite results from the lower Langtang valley; *Macfarlane* [1993] reported these data for a second time along with seven other muscovite results. One of these samples, with an age of 2.6 Ma, was collected within a brittle fault zone and consisted of predominantly calcite, white mica, and quartz, suggesting that much of this mica grew below its closure temperature, and therefore, we believe the age of this sample does not reflect the same conditions as the other nine muscovites reported by *Macfarlane* [1993] or the data reported here. *Arita et al.* [1997] reported five muscovite and one whole-rock phyllite $^{40}Ar/^{39}Ar$ analyses from the Kathmandu nappe and one muscovite from the MCT zone south of Manaslu, 50 km to the northwest. Only the five muscovite ages from the Kathmandu nappe are considered here.

[24] In the southern part of the Kathmandu nappe, nine of the muscovites reported here appear to not have been equilibrated during Himalayan metamorphism. This suggests that during the early Miocene these samples were either heated for a rather brief time or that their maximum temperature during this time was less than ~350°C (the nominal closure temperature of muscovite) or that the closure temperature of these muscovites is high, in excess of 400°C which is consistent with recent measurements of *Harrison et al.* [2009] and *Célérier et al.* [2009]. Two of the muscovites reported by *Arita et al.* [1997] also suggest lack of equilibration in the Miocene following an older heating event. For all of these samples, we use the youngest apparent age obtained during step heating as the maximum possible time of the most recent mobilization of Ar in these muscovites.

[25] Together with the compiled data, the most striking feature is that the ages increase progressively from north to south from circa 5 Ma to circa 20 Ma at the front of the

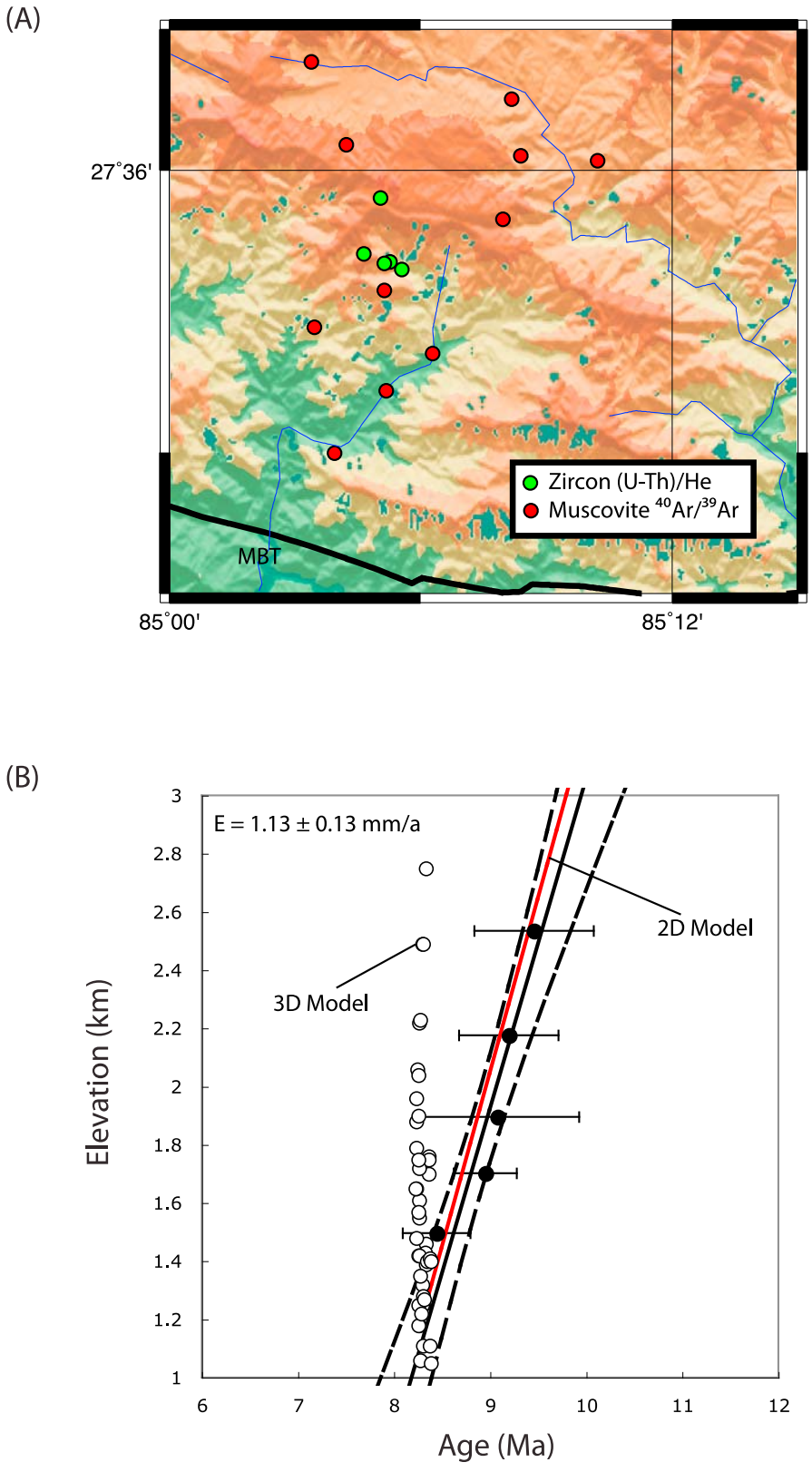

Figure 7. Thermochronological and thermobarometric data in the Palung area. (a) Shaded topography and data extracted from Figure 1. (b) Age-elevation plot for zircon (U-Th)/He shown in Figure 7a. Black dots are data. The black line is the linear regression performed on data with 95% confidence interval (dashed black lines). *E* defines the exhumation rate derived from the linear regression. The red line represents the exhumation rate for 2-D duplex model. The open circles are model predictions from CASCADE/PECUBE coupled model.

Table 3. Zircon (U-Th)/He Ages From Palung Area[a]

Sample	Elevation (m)	Longitude	Latitude	Rep	*n*	Mass (mg)	He (ng/mol)	U (ppm)	Th (ppm)	Radius (μm)	F_t	Age (Ma) Raw	Age (Ma) Corrected	Error (Ma)
PL3	1400	85.0925	27.5648	A	1	17.9	43.83	1118	70.6	54.3	0.82	7.11	8.64	0.017
				B	1	23	27.69	715	49.5	60	0.84	7.01	8.36	0.016
				C	1	12	28.94	862	55.2	48.6	0.8	6.08	7.59	0.015
				D	1	22.9	40.63	919	302.3	57.1	0.83	7.55	9.08	0.018
				mean									8.42	0.36
PL4	1650	85.0878	27.5676	A	1	25.2	29.74	777	30	62.9	0.84	6.98	8.23	0.016
				B	1	23.7	38.2	867	36.1	60	0.84	8.02	9.57	0.019
				C	1	23.7	29.51	729	34.9	60	0.84	7.36	8.78	0.017
				D	1	13.5	33.26	815	42.2	48.6	0.81	7.42	9.22	0.018
				mean									8.95	0.32
PL5	1840	85.0856	27.5669	A	1	16.9	23.74	584	51	51.4	0.82	7.33	8.98	0.018
				B	1	15.5	32.1	942	26.1	51.4	0.81	6.23	7.65	0.015
				C	1	15.7	47.13	986	67.9	51.4	0.81	8.65	10.63	0.021
				mean									9.08	0.85
PL6	2100	85.0774	27.5703	A	1	23.3	32.4	794	48.7	58.6	0.84	7.4	8.86	0.017
				B	1	31	21.08	395	398.9	68.6	0.85	7.94	9.33	0.018
				C	1	19	22.85	474	54.1	58.6	0.83	8.64	10.41	0.021
				D	1	17.2	26.06	680	38.3	55.7	0.82	6.95	8.44	0.017
				mean									9.2	0.52
PL7	2470	85.084	27.5901	A	1	17.2	70.3	1477	35.8	55.7	0.82	8.7	10.56	0.021
				B	1	23.5	16.9	422	74.4	62.9	0.84	7.08	8.41	0.017
				C	1	19.1	36.56	842	95.7	57.1	0.83	7.78	9.4	0.019
				mean									9.46	0.76

[a]Rep, replicates; *n*, number of grains used. For each replicate, 1σ is the analytical error. For the mean age the error is the standard deviation divided by $(k-1)^{1/2}$, where k is the number of replicates. F_t is the α ejection correction. Details about analytical procedure can be found in the appendix.

High Himalaya and in the hanging wall of the MCT (Figure 4).

3.2.2. Fission Track Data

[26] We have determined 10 apatite fission track ages which span from 6.1 ± 1.4 Ma to 1.3 ± 0.3 Ma (Table 2). These new data are consistent with the compiled data. Altogether they depict a southward increase of ages similar to the muscovite ages pattern, with ages varying from less than 1 Ma around the MCT to a few millions years to the south (Figure 4).

3.2.3. (U-Th)/He Data

[27] The Palung area south of Kathmandu basin (Figures 1 and 6), where a granite body is intruded into the Kathmandu klippe, is probably one the few appropriate locations in the Lesser Himalaya where it is possible to sample a vertical transect with possibly sufficient difference in elevation to constrain the exhumation rate. This alkaline granite, of Ordovician age [*Schärer and Allègre*, 1983], is crosscut by very narrow valleys which will give access to samples at elevations between ~1400 m to ~2600 m. A few FT ages [*Arita and Ganzawa*, 1997] and some $^{40}Ar/^{39}Ar$ ages are already available from this area (Figure 6). In complement, we collected a vertical transect for (U-Th)/He dating of zircon (Figures 7 and Table 3). The ages range between 8.45 ± 0.35 Ma and 9.46 ± 0.62 Ma. The age-elevation correlation suggests an apparent exhumation rate of 1.13 ± 0.13 mm yr^{-1} (Figure 7b).

3.3. Thermometric and Thermobarometric Data

[28] Different techniques have been used to estimate the peak metamorphic conditions reached by the rocks now exposed in the Himalaya. A number of studies have focused on the MCT zone and the HHC where the lithology is appropriate for thermobarometric techniques based on the thermodynamics of mineral assemblages [e.g., *Pêcher*, 1989; *Guillot et al.*, 1999; *Rai et al.*, 1998; *Catlos et al.*, 2001; *Kohn et al.*, 2001; *Rolfo et al.*, 2001; *Kaneko*, 1995]. In general it is possible to infer both the peak metamorphic pressure and temperature. In the metasediments of the Lesser Himalaya peak metamorphic temperature was mostly estimated from Raman Spectroscopy of Carbonaceous Material (RSCM) [*Beyssac et al.*, 2004; *Bollinger et al.*, 2004a]. These data show an inverted thermal gradient with temperature increasing up the section from about 350°C in the core of the Lesser Himalaya anticlinorium to as much as (≥700°C) a few kilometers above the MCT zone (Figure 8). The pressure data show exhumation from about 4–8 kbar within the MCT zone, increase to a maximum of about 10–12 kbar at the top of the MCT zone and decrease gradually farther up the section to about 6–7 kbar (Figure 9).

4. Modeling Inversion Approach

[29] In this section we detail the methods we use to analyze the data set described above. The data are first compared with predictions made from thermokinematic modeling computed using PECUBE [*Braun*, 2003; *Herman et al.*, 2007a]. This numerical model is briefly described in section 4.1 and the parameterization of the kinematic model is described in section 4.2. In contrast with previous thermokinematic models applied to the Himalayas [e.g., *Henry et al.*, 1997; *Huerta et al.*, 1998, 1999; *Bollinger et al.*, 2006; *Wobus et al.*, 2006; *Whipp et al.*, 2007], the model parameters are adjusted to best fit the data using a formal inversion algorithm, the Neighborhood Algorithm [*Sambridge*, 1999a, 1999b]) described in section 4.3. This inversion is based on simplifying assumptions; topography is assumed steady state and the kinematics of deformation is

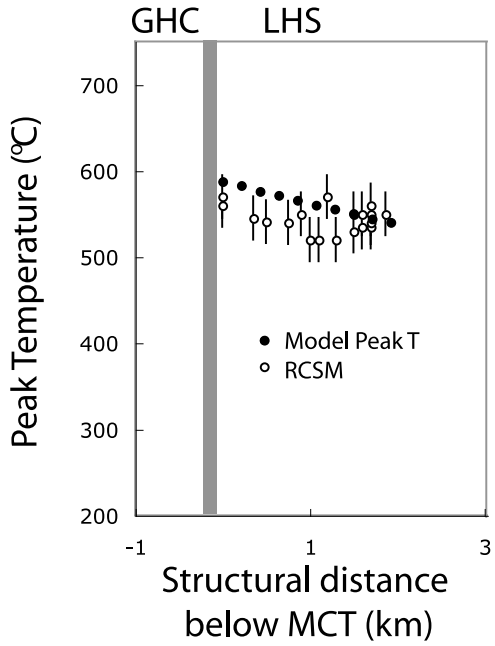

Figure 8. Thermometric (RSCM) data from Marsyangdi river catchment. The predicted peak temperature for the duplex formation model for model 1 versus structural distance. The open circles are measured temperatures with their uncertainties, and the solid circles are model predictions for the duplex model.

assumed to be 2-D (no lateral variations). The relationship between morphology and the kinematics of deformation is assessed using the landscape evolution model CASCADE [*Braun and Sambridge*, 1997] coupled with PECUBE, which is described in section 4.4. In contrast with previous models [e.g., *Henry et al.*, 1997; *Huerta et al.*, 1998, 1999; *Bollinger et al.*, 2006; *Wobus et al.*, 2006; *Whipp et al.*, 2007], this 3-D modeling enables testing whether the current morphology of the range is consistent with the proposed kinematics of crustal deformation and erosion. The coupling of CASCADE with PECUBE moreover enables assessing the validity of the assumptions made in the 2-D inversion of the thermochronological and thermobarometric data.

4.1. Thermokinematic Model: PECUBE

[30] We solve the heat transfer equation in two and three dimensions:

$$\rho c\left(\frac{\partial T}{\partial t}+\mathbf{v}\nabla T\right)=k\nabla^2 T+H+H_s \qquad (1)$$

where $T(x, y, z, t)$ is the temperature (K), ρ is rock density (kg m^{-3}), c is heat capacity (J kg^{-1} K^{-1}), $\mathbf{v}(u, v, w)$ is the velocity field (km Myr^{-1}), k is the thermal conductivity (W m^{-1} K^{-1}), $H(x, y, z)$ is radioactive heat production per unit mass (μW m^{-3}), and H_s is the shear heating (μW m^{-3}). We use a modified version of a finite element code (PECUBE [*Braun*, 2003; *Herman et al.*, 2007a]) to solve equation (1) within a crustal block, including the effects of a time-varying topography. We included the effects of spatially varying radiogenic heat production and shear heating for our study. We compute shear heating everywhere in the medium as the product of the shear stress and strain rate tensors [e.g., *Graham and England*, 1976; *Molnar and England*, 1990; *Burg and Gerya*, 2005]. The strain rate can be estimated from the velocity field, whereas the components of the stress tensor can only be approximated since the model is kinematic. In the brittle domain, all the components of the stress tensor are equal to the lithostatic pressure ($\tau = \mu\ (\rho - \rho_w)\ g\ z$ and $\mu = \tan(\phi)$, where τ is the shear stress (Pa), g is the gravitational acceleration (m s^{-2}), ρ_w is the density of water, z is the depth (m), and ϕ is the friction angle). In the ductile domain, the shear stress is calculated from a power law ($\tau^p = \dot{\epsilon}/[A\ \exp(-Q/RT)]$, where $\dot{\epsilon}$ is the strain rate (s^{-1}), p and A are the intrinsic constants (MPa^{-1} s^{-1}), Q is the activation energy (J mol^{-1}), and R is the universal gas constant). A granite flow law [*Hansen and Carter*, 1982] is used for the parameters in the ductile regime, and a 50 MPa value is assumed for the maximum shear stress.

[31] At the end of the model run, we extract thermal histories to compute ages and recorded peak pressure and temperature for rocks that end up at the surface. The thermochronological ages are computed solving the solid state

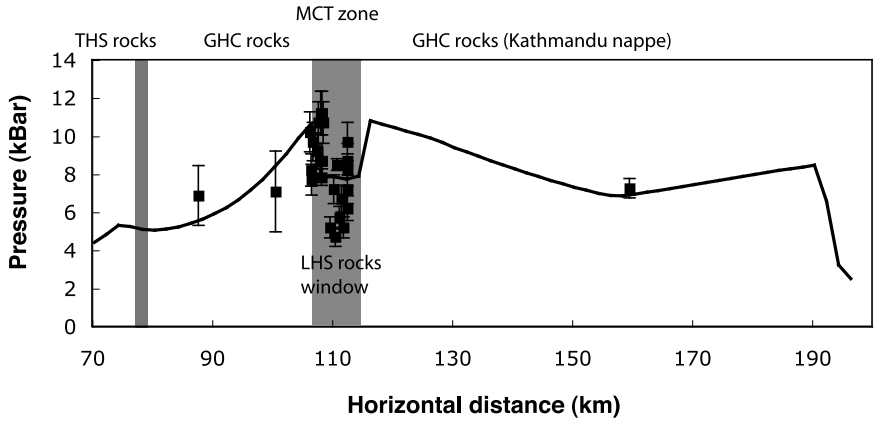

Figure 9. Peak pressure versus horizontal (map) distance; data (black squares with error bars) and duplex model prediction (black line). Note that the data point on the Kathmandu klippe is just shown for reference [*Rai et al.*, 1998] since there are no coordinates reported for this sample.

diffusion equation, as described in detail by *Herman et al.* [2007a].

4.2. Model Kinematics

[32] Figure 10 portrays the kinematics we use in the models. We test two kinds of kinematic model, using an Eulerian frame of reference, (1) duplex formation and (2) out-of-sequence thrusting, and we assume a two-stage kinematic evolution. For both models, the first stage is identical: we simulate the effect of overthrusting a hot hanging wall over a downgoing footwall within a crustal block that is 200 km long and 60 km thick (Figure 10). The main thrust is treated as a flat ramp, defined in the model by a kink fault which is assumed to be equivalent to the MHT. The velocity field is defined according to the fault-bend folding method [*Suppe*, 1983], in which only simple shear parallel to the underlying fault is allowed. The location of the kink is imposed at depth D (km) and 70 km north from the surface trace of the thrust at the surface (Figure 10), which in turn defines the dip of the flat. The dip of the ramp is set equal to 15°. The displacement along this thrust is achieved by ascribing a total convergence velocity (v_t = 20 mm yr^{-1}), which is partitioned between the footwall/underthrusting and hanging wall/overthrusting velocities, v_u and v_o, respectively (Figure 10):

$$v_o = (1 - \lambda)v_t \tag{2}$$

$$v_u = \lambda v_t \tag{3}$$

During this first stage, $t \leq t_e$, some accretion (A_2 (mm yr^{-1})) is included all along the thrust (Figure 10) to simulate foreland propagation.

[33] In the second stage of the duplex model ((Figure 10a, $t \geq t_e$), we increase the total vertical exhumation (A_1 (mm yr^{-1})) over a given window, which is lying between a distance w (km) and 130 km away from the trace of the MHT at the surface (Figure 10). This, in turn, corresponds to a local increase of erosion. It is important to realize that, as we add this vertical exhumation, material from the underthrusted plate is underplated through the main thrust, which leads to the formation of a duplex structure similar to the one described by *Schelling and Arita* [1991], *DeCelles et al.* [2001], *Robinson et al.* [2003], and *Bollinger et al.* [2004a] (Figure 10a). During this second stage, we accurately track the evolution of a sheet lying above the MHT. The trace of the exposed thrustsheet at the end of the numerical experiment is then used to define the location and dip of the MCT.

[34] During the second stage of the out-of-sequence thrusting model (Figure 10b), the increase of exhumation is accommodated by motion along a major fault, equivalent to the MCT1 [*Arita*, 1983; *Catlos et al.*, 2001] or PT2 structure [e.g., *Hodges et al.*, 2001; *Wobus et al.*, 2003], that is imposed parallel to the ramp (as it is required to maintain a kinematic field that respects the continuity equation). The chosen parametrisation (Figure 10) is such that the slip rate on that fault is αv_o.

[35] The STD is set inactive in the duplex model (noting that the model is only valid for the last ~15 Myr) and accommodates some motion in the out-of-sequence thrusting model so that the convergence rate is kept constant and equal to 20 mm yr^{-1}. In fact the model is not very sensitive to the STD. Motion on the STD does not have a strong effect on the key modeled data and, in absence of reset cooling ages from above the STD, kinematics of that fault is not testable. It follows that the kinematics of the STD are only constrained indirectly due to the imposed total shortening rate.

4.3. Inversion Method: Neighborhood Algorithm

[36] Following previous similar studies [*Braun and van der Beek*, 2004; *Herman et al.*, 2007a], we use the Neighborhood Algorithm (NA) [*Sambridge*, 1999a, 1999b] to determine the range of model parameters permitted by the data and to select plausible best fitting models. We assume the prior information to be a uniform probability density function (PDF) across a given range and derive a posterior PDF for each parameter. The NA is a two-stage numerical procedure for nonlinear inverse problems. Details of NA are given by *Sambridge* [1999a, 1999b].

[37] The first, search, stage consists of a direct search method in a multidimensional parameter space. The objective of this mathematical procedure is to find models, or parameters, which minimize the misfit to the data. NA is an iterative method making use of simple geometrical concepts. At each stage the entire parameter space is divided into a set of Voronoi cells, one cell about each previously sampled model. Voronoi cells represent the nearest neighborhood about each point. These cells are then used to guide the next sampling step, in a randomized fashion. As iterations proceed, the algorithm concentrates sampling in regions of the parameter space where a given misfit function is optimized. In our study, we optimize a weighted least squares misfit function ψ,

$$\psi = \sum_{j=1}^{M} \frac{1}{N_j} \sum_{i=1}^{N_j} \frac{(x_{i,m} - x_{i,o})^2}{\sigma_i^2} \tag{4}$$

where $x_{i,o}$ are values issued from linear regressions between horizontal distance below to the MCT and age for each thermochronological/thermometric data, $x_{i,m}$ are the modeled ages/temperatures, and σ_i is the standard deviation on the linear regressions. Note that we first project the data along 1-D profiles from north to south and perform the regressions on it. Our objective is to reproduce the thermochronological and thermometric data as well as the exposed geology along a 2-D cross section. We do not attempt to fit with great detail all the age/elevation relationships observed in the thermochonological data but rather try to reproduce the horizontal variations in age, which dominates the patterns in the data. Each set of data has the same weight on the misfit. We also only try to explain the ^{40}Ar/^{39}Ar reset ages in the MCT zone. We use map distance for thermochronological data and structural distance for the thermometric data. M corresponds to the number of different data sets and N is the amount of data for each type of data. Finally, we assume that x_i (in equation (4)) are independent.

[38] The second, appraisal, stage consists of an algorithm for resampling the entire ensemble of models produced in the first stage, and deriving information from them in the

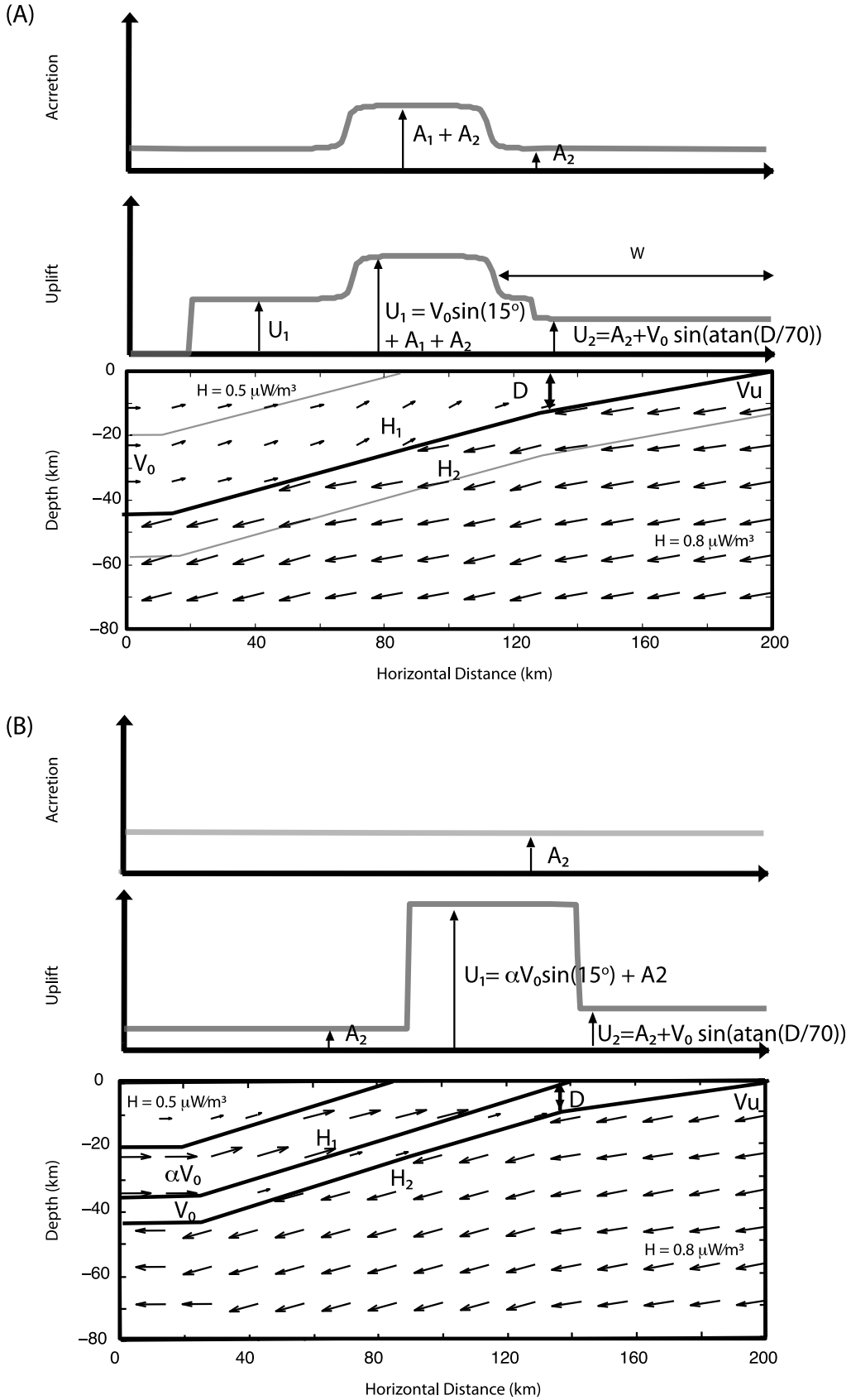

Figure 10. Kinematics used in (a) duplex and (b) out-of-sequence thrusting models. See text for details about the different parameters. Accretion, uplift, and velocity field are shown against horizontal distance. *U* is for uplift. All other parameters are defined in the text and Tables 4 and 5.

Table 4. Constrained Parameters[a]

Parameter	Prior Information	Posterior Value	Error	Posterior Value Out of Sequence	Error	Units	Kinematic Model[b]	Comment
λ	0.4–0.95	0.71	0.07	0.67	0.1		DM/OOS	Partitioning between overthrusting and underthrusting
T_b	600–850	776	54	706	144	°C	DM/OOS	Temperature at the base of the model
D	7–13	11.45	1.38	8.01	0.07	km	DM/OOS	Depth of kink-fault
w	50–110	86	13	N/A	N/A	km	DM	Distance of high exhumation window from trace of MHT
E_1	1.0–6.5	3.4	0.9	N/A	N/A	mm/yr	DM	Enhanced exhumation of underplating window
E_2	0.0–1.5	0.25	0.18	0.3	0.21	mm/yr	DM/OOS	Vertical accretion rate
μ	0.01–0.1	0.05	0.03	0.06	0.04		DM/OOS	effective friction coefficient
H_1	1.6–2.4	2.1	0.16	1.7	0.4	μW/m^3	DM/OOS	Radiogenic heat production in GHC
H_2	0.8–2.4	1.9	0.24	1.04	0.4	μW/m^3	DM/OOS	Radiogenic heat production below MHT
t_e	14–4	9.8	1.7	7.3	1.6	Ma	DM/OOS	timing of formation of duplex
α	1–4	N/A	N/A	2.8	0.8		OOS	increase of motion along the MCT

[a]The range of the prior distribution is taken to be uniform. The posterior value shows the optimal value of the posterior distribution for the duplex model. The same results are given for the out-of-sequence thrusting model. Note that the prior probability is a marginal probability, interpreted as a description of what is known about each variable before the inversion. The posterior probability is then derived with the formal inverse approach. N/A stands for not applicable.

[b]DM is duplex model, and OOS is out-of-sequence thrusting.

form of Bayesian measures of covariance and marginal PDFs. The likelihood function used to compute the PDFs is defined using the ensemble of models produced during the first stage as follows:

$$L = \prod_{j=1}^{M} \exp\left[-\frac{\nu_j}{2N_j} \sum_{i=1}^{N_j} \frac{(x_{i,m} - x_{i,o})^2}{\sigma_i^2} \right] \quad (5)$$

where ν_j is the number of degrees of freedom for each data set (i.e., number of data minus the independently constrained model parameters).

[39] The independent parameters which are solved in the inversion and some useful dependent parameters are listed in Table 4. Table 4 presents the prior information on each parameter. For both models we invert λ; the temperature at the base of the model (T_b(°C)), the radiogenic heat production in the HHC sequence (H_1); radiogenic heat production in the 5 km thick layer below the MHT (H_2); t_e; D; μ and A_2. For the duplex model only, we invert w and A_1. For the out-of-sequence model only, we try to constrain α. For both models, we impose a radiogenic heat production in the Indian Shield of 0.8 μW m^{-3} and 0.5 μW m^{-3} in the THS, and the topography is maintained steady.

4.4. CASCADE/PECUBE Coupled Model

[40] We assume that large-scale landscape evolution is mainly controlled by river incision via a unit stream power model:

$$\frac{\partial h}{\partial t} = u - v\frac{\partial h}{\partial x} - KA^m S^n \quad (6)$$

where h (m) is the topography, u (mm yr^{-1}) is vertical rock uplift, K is erosional constant (m^{1-2m}/a), A (m^2) is drainage area, used as proxy for local discharge, S is the river gradient (in the direction of water flow), and m and n are positive constants set equal to 1/2 and 1, respectively [*Whipple and Tucker*, 1999]. It also includes a maximum slope of 35° to represent hillslope processes. It is worth noting that we do not include diffusion because it did not enable to satisfyingly reproduce the first-order geomorphology compared to using a maximum slope. The isostatic rebound is approximated by computing the vertical deflection of an elastic plate subject to vertical loading. We use the CASCADE algorithm [*Braun and Sambridge*, 1997], which solves equation (6) on an irregular Lagrangian grid. Adaptive remeshing of the deforming grid was based on maximum and minimum surface areas assigned to each node (i.e., nodes are removed when areas become to small and vice versa). Coupling to PECUBE is then achieved by first interpolating the evolving surface topography on an Eulerian mesh and imposing this geometry as surface boundary condition of the 3D thermal model.

5. Inversion of the Data Set From 2-D Thermokinematic Modeling

[41] Using a high performance cluster, we are able to perform a large amount of forward model runs (~30,000 in total) in a reasonable amount of time. It is worth noting that it is necessary to run such a large number of models to obtain a statistically significant fit, given the amount of parameters set free. As explained above, all the thermochronological and thermometric data are inverted except that the effect of elevation is not considered because the topography in the 2-D model is simplified (in this section we use a topography linearly decreasing with horizontal distance from 6 km to 0 and discuss in section 6 the effects of using a more realistic topography in the PECUBE/CASCADE coupled model) and does not allow to extract elevation profile which could be compared to the real data. The comparison might not make much sense anyway because it is unlikely that the present topography can be assumed steady state.

[42] The results of the inversion are shown in Figures 11 and 12 as scatterplots in the parameter space. Each dot represents a forward model. The color scheme associated with each dot relates the quality of fit to the data (using exponential value of the optimized function ψ). Figure 11 corresponds to the inversion results of the duplex formation model, whereas Figure 12 depicts the results of the inversion for the out-of-sequence model. In Figures 13 and 14, we present the one-dimensional computed marginal PDFs. The results are summarized in Table 4. The optimal posterior

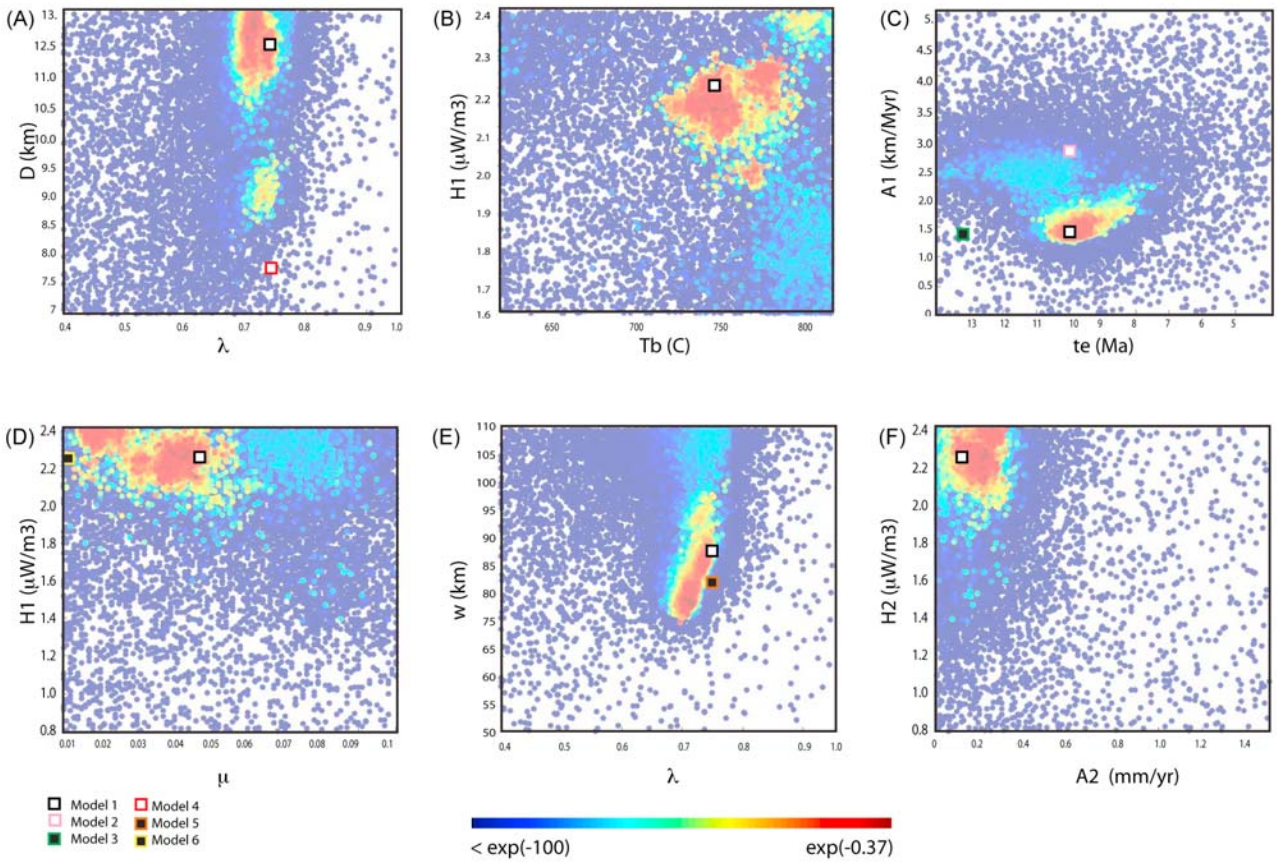

Figure 11. Results of the Neighborhood Algorithm (NA) inversion for the duplex model as scatter diagrams of the misfit between observations and predictions. Each dot corresponds to a forward model run. The position of the dot is determined by the value of the model parameters (which are defined in Table 4). The color of the dots is proportional to the value of the calculated misfit: red corresponds to low misfit values, and blue corresponds to high misfit values. Each diagram corresponds to a projection of all model runs onto a plane defined by 2 of the 10 parameters. Note that during the inversion procedure all model parameters are free to vary simultaneously. Only a small number (six) of all possible combinations of pairs of parameters are shown. Open squares show the location of the best fit model (model 1). Forward models are shown by the colored squares; model 2, pink and white; model 3, green and black; model 4, red and white; model 5, brown and black; model 6, yellow and black.

values for each kinematic scenario are given in Table 4. Their estimated errors resulting from the second stage of the inversion method are reported.

5.1. Duplex Model

[43] For the duplex model, the outcome of the inversion clearly demonstrates the compiled data set contains information on most of the parameters as convergence of the NA is observed (Figure 11) and Gaussian and exponential PDFs from the 1-D marginal integrals are obtained (Figure 13). The function ψ is minimized down to a value of 0.69 corresponding to a reduced chi-square $\chi_r^2 = 5.03$.

[44] We first discuss the plausibility of the model parameters derived from the inversion. The estimated overthrusting rate deduced from λ values is well constrained to 5.8 ± 1.4 mm yr^{-1} (Figures 11a and 13a). This is because this rate is essentially determined by cooling age gradients in the LHS. The rate of accretion associated with the growth of the Lesser Himalayan duplex is also relatively tightly constrained to 1.55 ± 0.9 mm yr^{-1}, which is consistent with the rate infer by *Huerta et al.* [1999]. This is because, together with the overthrusting rate, this rate determines the gradient of peak metamorphic temperatures in the Lesser Himalaya. The age of initiation of the duplex is constrained to 9.8 ± 1.7 Ma. This parameter is mostly constrained by the distribution of peak metamorphic temperatures; which places constraints on total exhumation. The age of the formation of the Himalayan duplex turns out to be comparable to the age proposed by *Robinson et al.* [2003] based on palinplastic reconstruction and Nd isotope record of exhumation of the Lesser Himalaya from sections in the sub-Himalaya of western Nepal [*Huyghe et al.*, 2001]. Finally, the model predicts an erosion rate pattern that coincides reasonably well with that inferred from river incision [*Lavé and Avouac*, 2001; *Garzanti et al.*, 2007] (Figure 15). The inversion results suggest H_1 equal to 2.2 ± 0.2 μW m^{-2} for the HHC (Figures 11b and 13g). Some shear heating is required to fit the data, but the effective friction coefficient

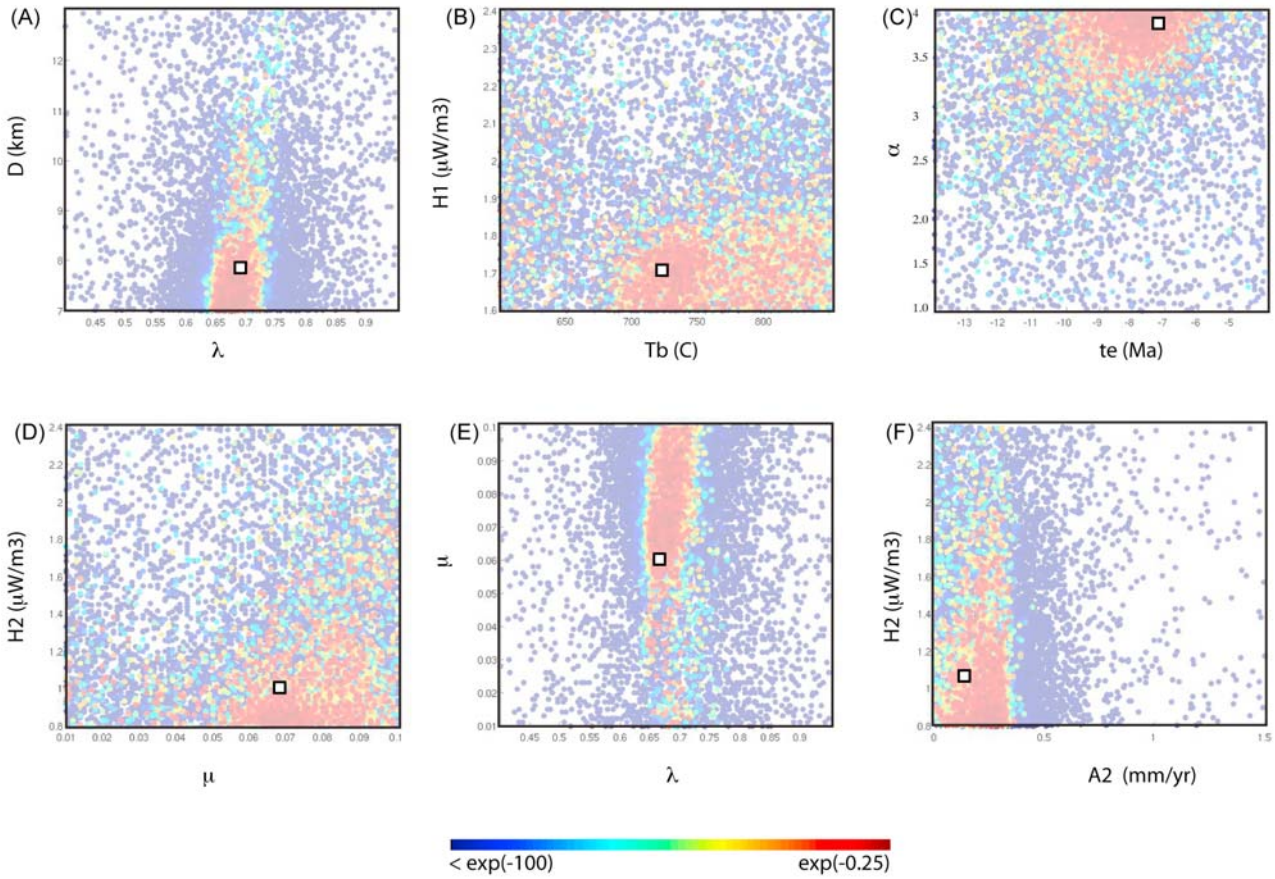

Figure 12. Same as Figure 11 for the out-of-sequence thrusting model. Squares show the location of the best fit model (model 7).

is found to be smaller than 0.07 (Figure 13j). Such a low value is consistent with the maximum effective friction of the order of 0.1–0.2 derived from the requirement that the stresses within the relatively low taper of the Himalayan wedge cannot exceed its internal brittle strength as estimated from *Byerlee*'s [1978] law [*Cattin and Avouac*, 2000]. The depth of the upper edge of the midcrustal ramp D is constrained to a minimum depth of about 11 km (Figures 11a and 13e). It implies a minimum dip angle of the décollement beneath the Lesser Himalaya of about 9°; which leads to mean rock uplift/exhumation of about 1 mm yr^{-1}, comparable to that of *Lavé and Avouac* [2001] and obtained from the slope of age-elevation relationship of the newly established zircon (U-Th)/He data (Figure 7b). Finally, the analysis places a lower limit on T_b of 700°C and lower limit on w of 86 km (Figure 13). It implies that the high exhumation window is located more than 86 km away from the surface trace of the MHT. This more or less corresponds to the front of the high range.

[45] The set of parameters corresponding to that best fitting model (model 1) is listed in Table 5 and is represented in Figures 11 and 13. This model is able to reproduce the inverted metamorphic gradient and provides a satisfying fit to most available observations on the chronology and amount of exhumation in the HHC and LHS. The corresponding velocity field and thermal structure are shown in Figure 15. Predictions of these particular models are reported in Figures 4 and 6–8. The ages predicted from this model generally fit the young ages around and north of the MCT Zone as well as the linear increase of ages toward the south (Figure 4a). The duplex model fits the youngest ages in the footwall of the MCT, and the average ages between the MCT and STD. The 2-D models cannot, however, resolve the scatter in age that is observed. This can be easily explained since the data is projected along a 1-D profile and ignore both lateral and temporal variations. Lateral variations must in fact exist since the extent of the HHC klippes in the lesser Himalaya vary laterally significantly (Figure 1). Furthermore, the 2-D model used in the inversion ignores effects due to the temporal variations of the topography, the potentially changing relative position of the samples, and do not include model complexities such as fluid flow generating late muscovite recrystallization, fluid flow in the uppermost crust or grain size for the computation of the thermochronological ages. The model reproduces reasonably well the $T - t$ paths in the MCT zone and in the Lesser Himalaya (Figure 6). In Figures 5 and 7, we also compare the elevation-age profiles in the Marsyangdi and Palung area with the cooling ages at the surface of the model topography and the vertical uplift rates deduced from the best fitting duplex model. Note that this comparison makes the common assumption that all points lie more or less along

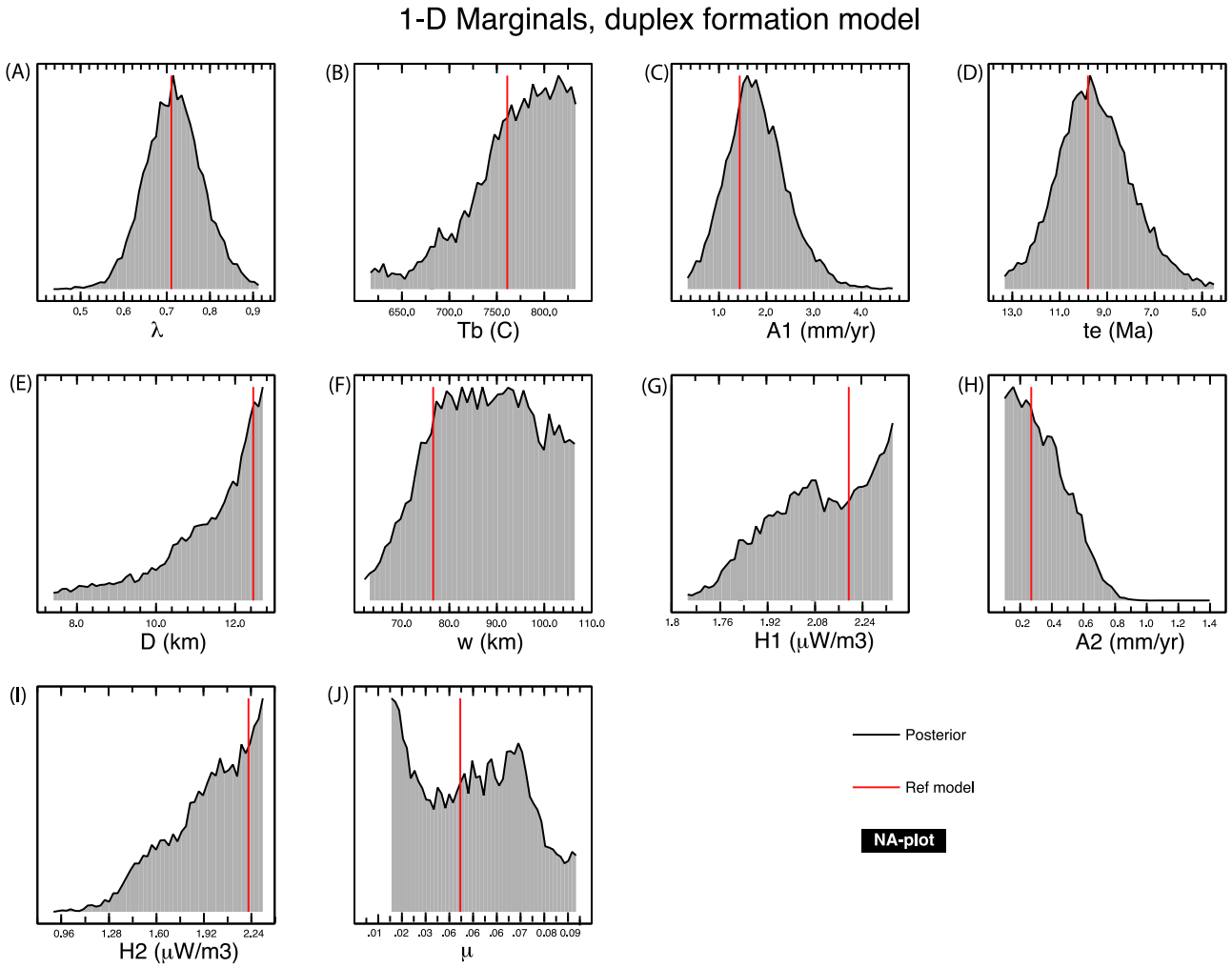

Figure 13. The 1-D marginal PDFs for all the 10 model parameters obtained using the NA resampling algorithm for the duplex model. The *x* axes represent the range of possible values for each parameter. The *y* axes are the value of *L* in equation (5). The parameter prior distributions are assumed uniform (i.e., the optimal parameter value has the same probability for any value within the chosen range). The solid line represents the value for the model that leads to the best fit.

the same trajectory so that the gradient of age with elevation is directly a measure of the vertical component of exhumation (assuming the thermal structure and topography are at steady state). The model can also explain how peak temperatures vary with structural distance from the MCT, with peak temperature decreasing from ~800°C in the HHC rocks to ~450°C in the vicinity of the MCT zone and down to ~450° in the LHS (Figure 8). In Figure 9, we compare the peak pressures reached for rocks that end up at the surface at the end of the forward run. To a first order, there is a good agreement between observed pressure patterns in the HHC, the MCT zone and the LHS (although the estimated pressure in the latter unit are slightly overestimated). From north to south, peak pressures increase toward the MCT zone within the HHC up to ~11 kbar and then decline progressively to the south, on what is equivalent to the Kathmandu klippe. The model is able to predict peak pressures that abruptly drop down to about 7–8 kbar within the LHS window. This is easily explained by the fact that the 2-D model is median in between an end-member without any duplex erosional breaching (in Kathmandu region) and another of total breaching after the erosion of the overlying nappes (along Marsyangdi).

[46] We have selected a number of models to illustrate the sensitivity of the model to the various adjustable parameters (models 2 to 6); those for which a sensible PDF resulted from the inversion. The parameter values we use for each model are reported in Table 5 and plotted in the parameter space for reference (Figure 11). We only discuss the results in the light of the thermochronological data.

[47] In model 2, we increase the exhumation rate, and consequently the amount of Indian rocks that are being underplated through the MHT. It clearly appears in Figure 16a that a zone of nonreset ages for $^{40}Ar/^{39}Ar$ in muscovite is exposed in the footwall of the MCT. As discussed above, such a sharp contrast in ages has been interpreted to reflect the presence of an active thrust in the Holocene [e.g., *Wobus et al.*, 2003]. This forward model clearly demonstrates that no active faulting is required to explain the nonreset ages at the front of the High Himalaya.

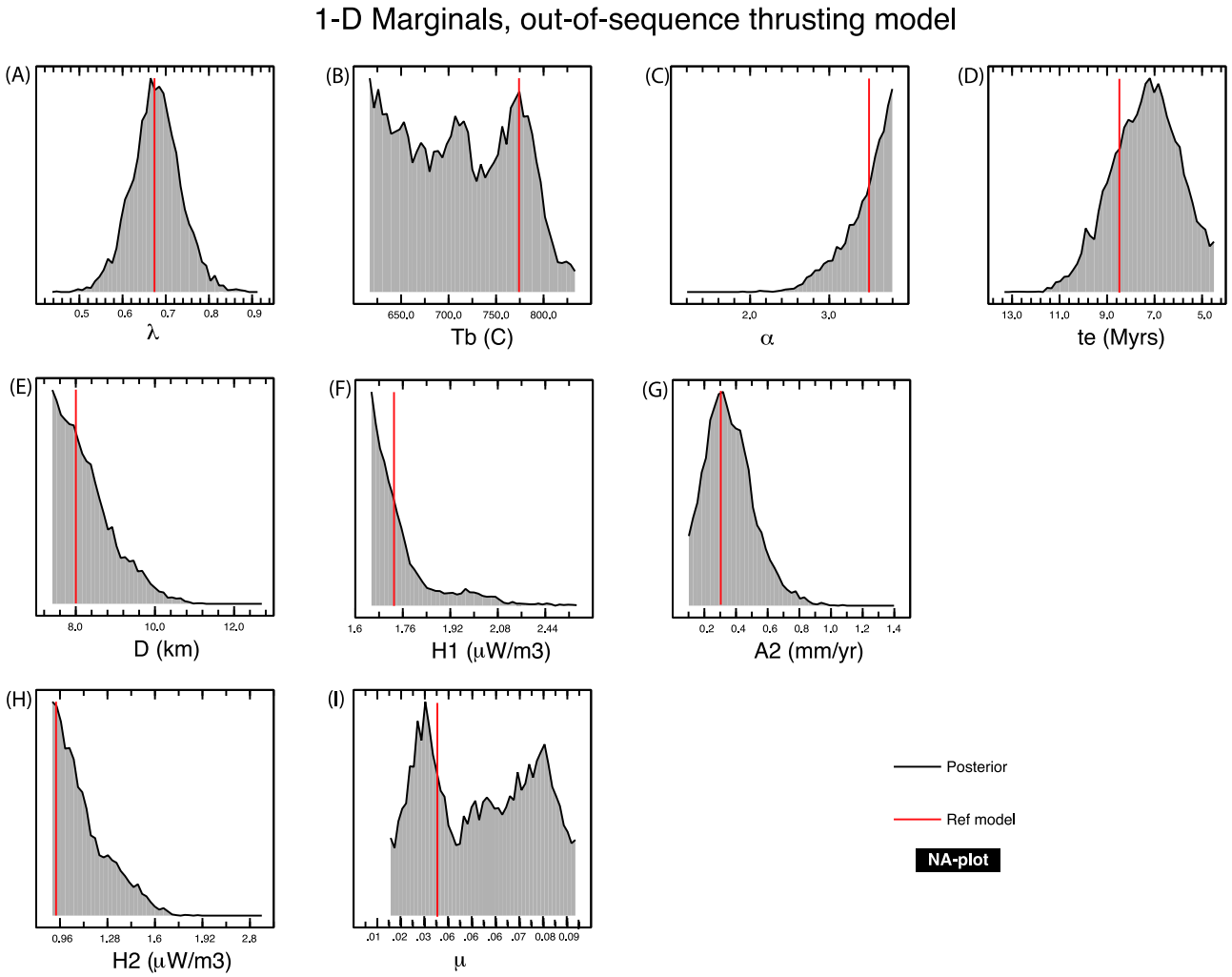

Figure 14. Same as Figure 13 for the out-of-sequence thrusting model, except that only nine parameters are constrained from the inversion.

Instead, it reflects the fact that an increase of erosion would lead to an increase of underplated material, which has not experienced temperature high enough to completely reset the ages. Furthermore, we observe that the trace of the MCT in our model does not necessarily match with the abrupt reset/unrest age transition in the $^{40}Ar/^{39}Ar$ in muscovite data (as we will further show with the CASCADE/PECUBE coupled model). In model 3, we increase the timing of initiation of the duplex, t_e, to about 13 Ma. A similar behavior is observed, leading to zone of nonreset ages in the footwall of the MCT. However, the contrast in ages across the MCT is not as significant as in the previous scenario. Indeed, the ages progressively increase toward the south. In models 4 and 5, we modify the dip of the flatter section of the MHT and the location of underplating window through D and w. The most noticeable observation is again the emergence of this zone of old ages in the footwall of the MCT. In model 6, we reduce the effective friction coefficient. It appears to modify for $^{40}Ar/^{39}Ar$ in a very narrow zone. This further suggests that the data do not actually allow to tightly constrain the effective friction coefficient, but we can excude values larger than about 0.07. Finally, no major distinction can be observed in the low-temperature systems, as shown in Figure 5b.

5.2. Out-of-Sequence Model

[48] Compared to the duplex model, fewer parameters can be constrained tightly but convergence of the NA toward satisfying values of the misfit function is observed. The function ψ is minimized down to a value of 0.57 corresponding to a reduced chi-square $\chi^2_r = 3.69$. Inspection of the PDFs shows that the space of model parameters yielding a good fit to the data is relatively well defined. Gaussian PDFs are observed for λ, T_e, A_2 and exponential PDFs are observed for α, H_1, H_2 and D. As in the duplex model, the estimated overthrusting rate is well constrained to 6.6 ± 2 mm yr^{-1} (Figures 11a and 13a). No good constraints can be derived on μ and T_b. Some accretion all along the MHT is required to fit the data (Figure 14g). It appears in Figures 12b and 12f (and Figures 14f and 14h) that H_1 and H_2 are required to be smaller than 2 μW m^{-3}, which is relatively low for granitic rocks. Increased extrusion of the HHC due to reactivation of the MCT, t_e, would have started about 7.3 ± 1.6 Ma.

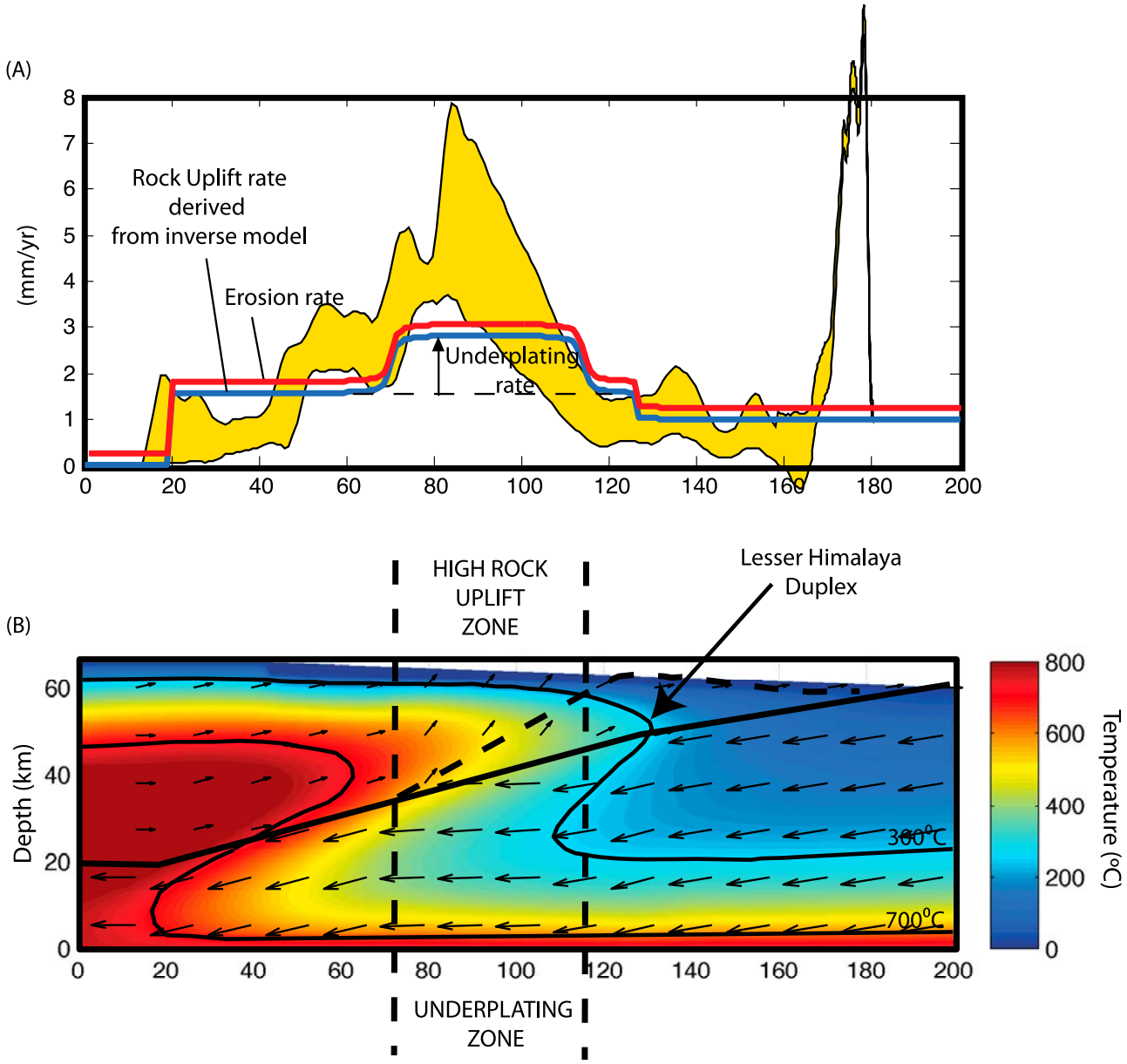

Figure 15. Rock uplift rate, erosion rate, thermal field, and velocity field for the duplex model. (a) Rock uplift rate (blue), erosion rate (red), underplating rate, and incision rates from *Lavé and Avouac* [2001] (yellow) are plotted against horizontal distance. Note that the detailed geometry of the MFT is not included in the model, which explains why no high rock uplift is modeled. (b) Thermal field as predicted for the duplex model at the end of the simulation. Underplating zone matches with the high rock uplift zone. Location of the Lesser Himalaya duplex is indicated. Small black arrows depict the velocity field predicted by the duplex model.

[49] The modeling shows that a reasonable fit to the thermochronological and thermometric data can also be obtained from the out-of-sequence thrusting model (Figure 4b). The set of parameters corresponding to that best fitting model, model 7, is listed in Table 5. The corresponding velocity field and thermal structure are shown in Figure 17. It should be noticed that the model can fit the young cooling ages within the MCT zone but that a rather rapid rate of extrusion of the HHC is needed, which corresponds to an α of about 3.8. It results that the pattern of ages is not as smooth as in the duplex model and predicts younger ages between the MCT and STD. The model predicts an erosion rate pattern which coincides reasonably well with that inferred from river incision rate during the Holocene [*Lavé and Avouac*, 2001] (Figure 17).

[50] The rapid extrusion that is required to reproduce the zone of young ages in the hanging wall of the MCT causes exhumation of hot HHC material within a narrow zone. Compared to the duplex model, there is no additional vertical heat advection below the MCT since it is modeled as a sharp fault. This in turn leads to a sharp age transition across the MCT that enables fitting both the very young ages

Table 5. Parameter Values Used for Each Forward Model[a]

Parameter	Model 1	Model 2	Model 3	Model 4	Model 5	Model 6	Model 7	Model 8	Model 9
Kinematics	DM	DM	DM	DM	DM	DM	OOS	OOS	OOS
λ	0.768	0.768	0.768	0.768	0.768	0.768	0.679	0.679	**0.73**
α	N/A	N/A	N/A	N/A	N/A	N/A	3	**1.2**	**1.2**
T_b	754	754	754	754	754	754	706	706	706
D	12.8	12.8	12.8	**7.8**	12.8	12.8	8.01	8.01	8.01
w	91.5	91.5	91.5	91.5	**81.5**	91.5	N/A	N/A	N/A
A_1	1.55	**2.51**	1.51	1.51	1.51	1.51	N/A	N/A	N/A
A_2	0.06	0.06	0.06	0.06	0.06	0.06	0.3	0.3	0.3
μ	0.05	0.05	0.05	0.05	0.05	**0.01**	0.06	0.06	0.06
H_1	2.24	2.24	2.24	2.24	2.24	2.24	1.7	1.7	1.7
H_2	2.24	2.24	2.24	2.24	2.24	2.24	1.04	1.04	1.04
t_e	10.8	10.8	**13.8**	10.8	10.8	10.8	7.26	7.26	7.26
Ramp dip	15	15	15	15	15	15	15	15	**30**
Flat dip	10.4	10.4	10.4	10.4	6.8	10.4	6.6	6.6	6.6

[a]The variables are defined in Table 4. N/A stands for not applicable. Varied parameters between each model are indicated by bold type.

(~2 Ma) in the footwall and progressive increase in age in the hanging wall.

[51] A major problem with the OOS model is that it requires a rapid slip rate on the MCT if the dip of the MCT is 15°. The inversion results suggest that α must be greater than 2.5, with a best fitting value of 3.8. The best fitting model corresponds to a slip rate of 18 mm yr^{-1}. This is the rate required to fit the young cooling ages at front of the High Himalaya, given the assumed dip angle of 15°. It is highly improbable that such a high slip rate on the MCT has sustained over the past 10 Myr, as shown in Figure 18 where we compare the shortening rate derived from the kinematic model to inferred shortening rates. Furthermore, such a rapid slip rate on the MCT would need to be compensated by a comparably large normal slip rate on the STD, if the convergence rate is maintained at 20 mm yr^{-1}. This seems improbable in view of the lack of evidence for active deformation on the STD. Despite some local indices of Plio-Quaternary activity nearby Thakkola and Gyirong grabens [*Hurtado et al.*, 2001], evidence of recent motion on the STD is weak. Although the STD can be traced all along the entire Himalayan arc for nearly 2000 km, not a single focal mechanism suggests active N-S extension [*Molnar and Lyon-Caen*, 1989]. In addition, cross cutting relationships with dated granite bodies show little cumulative slip on the STD over the past 15 Myr [*Searle and Godin*, 2003]. The alternative possibility would be that the shortening rate between India and South Tibet would be much larger than the current rate estimated from geodesy. This seems unlikely especially since the convergence rate between India and stable Eurasia has been relatively stable around, 4–5 cm yr^{-1}, over the past 10 Myr [*Patriat and Achache*, 1984].

[52] We have explored the possibility of forcing the slip rate on the MCT to a more reasonable value (i.e., less than 2 mm yr^{-1} in order to keep the total shortening within the uncertainty of the estimated shortening as shown in Figure 18). In model 8, we have thus imposed a lower value of α of 1.2, corresponding to a slip rate on the MCT of 1.3 mm yr^{-1}. The model then fails to reproduce the young ages north of the MCT ($\leq$8 Ma) (Figure 19b). Previous workers [e.g., *Whipp et al.*, 2007] have modeled a 28° ramp based on the surface geology [*Searle and Godin*, 2003], and if a similarly steep dip of 30° for the MCT is used in our model, it is possible to fit both the youngest ages and the shortening rate estimates (model 9 of Figure 19b and Table 2; see also Figure 18). Note that in our kinematic model the MCT must be parallel to the dip of the ramp to respect continuity and mass conservation. In that case, the slip rate on the MCT required for the model to fit the data is only ~1 mm yr^{-1}, only 5% of the 20 mm yr^{-1} shortening rate across the range. Although the contribution to the total shortening is found be small, it would however contribute to about 20% of the local rock uplift of the High Himalaya. In turn, this analysis rules out significant sustained activity in the MCT zone over the last 10 Myr, but does not exclude the possibility of episodic out-of-sequence reactivation of the MCT zone (as suggested by *Hodges et al.* [2004]). Therefore, we cannot exclude short periods with higher rates but are constraining the long-term average value to be low. Geophysical data are needed to test the viability of a 30° dip for the out-of-sequence thrusting model.

[53] Finally, the out-of-sequence model cannot explain the general klippe and windows structures in the Lesser Himalaya and it is therefore hard to reconcile with the observed surface geology. We therefore consider that the duplex model is a more probable scenario than the out-of-sequence model.

6. Consistency of the Duplex Model With the Topography Across Nepal Himalaya

[54] *Harrison et al.* [1997b] (and, subsequently, *Wobus et al.* [2003] and *Hodges et al.* [2004]) suggested that activity on the MCT marks the break in slope of the present-day mountain range. In this study, we now assess whether the proposed kinematics of crustal deformation across the Himalaya associated with the duplex model can also explain the first-order features of the observed topography. We use a theoretical topography as initial geometry with no topographic break (Figure 20a) and run the model forward in time for about 10 Myr (i.e., since the initiation of the Lesser Himalayan duplex (Table 4)). The kinematic field derived from the inverse problem is used to estimate horizontal tectonic advection and vertical uplift (u and v in equation (6)) on the topographic surface (using the parameters summarized in Table 4). The isostatic rebound predicted in CASCADE is included in the term u (assuming an elastic thickness of 15 km). The climate is imposed uniform across the range and

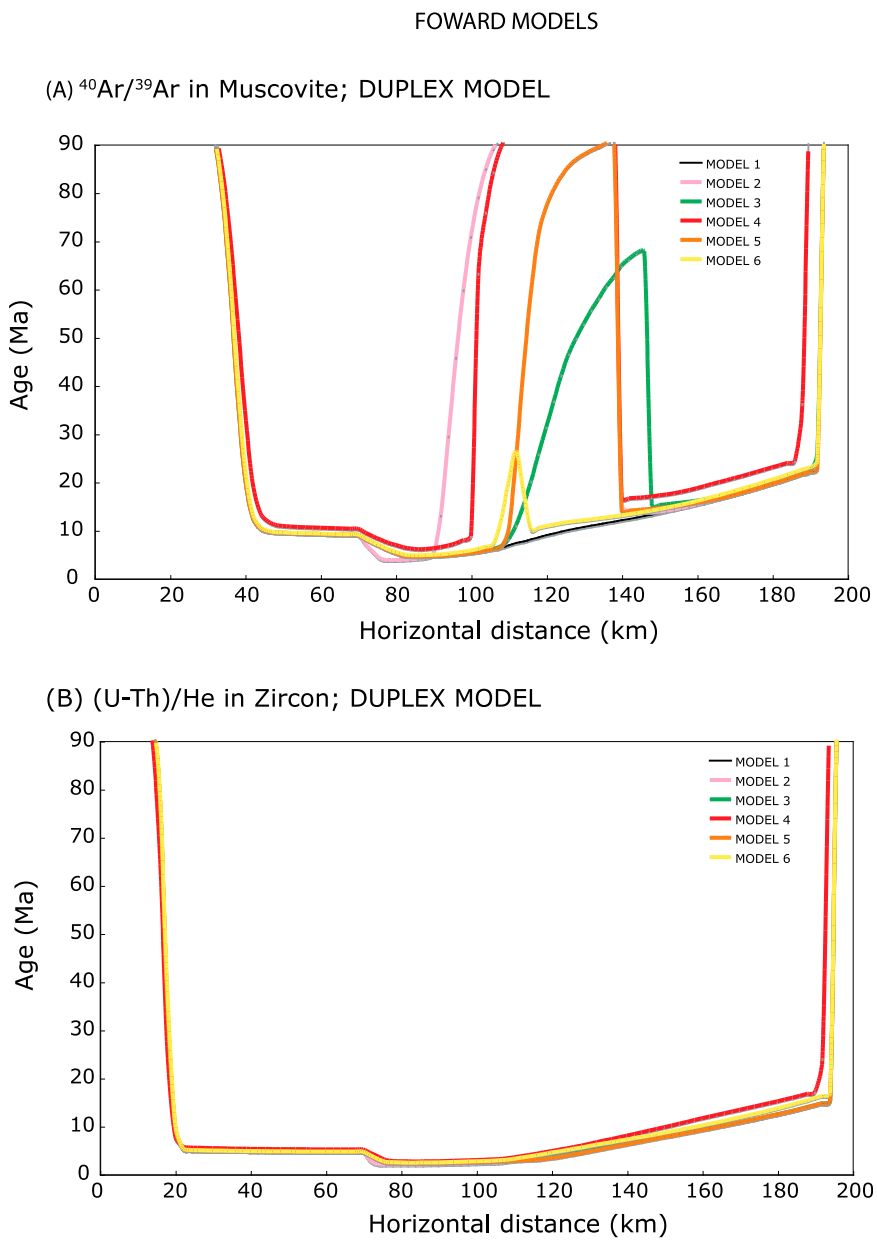

Figure 16. Forward modeling results. (a) The $^{40}Ar/^{39}Ar$ ratio in muscovite ages versus horizontal (map) distance for the duplex model. The parameters used for each model are summarized in Table 5. (b) (U-Th)/He in zircon ages versus horizontal distance for the duplex model.

does not vary through time. K is adjusted to reproduce the first-order geomorphology and topography (set equal to 3.5 10^{-6} yr^{-1}). The model is run at a spatial resolution of about 1 km on an irregular mesh, thus, fluvial processes dominate landscape evolution [*Kooi and Beaumont*, 1996]. The initial mesh is 200 km long and 80 km wide (so that we can have a model that is comparable to the swath topography shown in Figure 2a) and use Dirichlet boundary conditions (using linearly decreasing topography from north to south). We only attempt to reproduce the geomorphology to a first order and do not try to explain specific geomorphic features such as river spacing of the major drainage systems or simulate the effects of glacial erosion. It would be pointless to push the model any further since the physics of river incision, hillslope erosion and/or glacial erosion are still poorly known.

[55] We illustrate the results of the simulation in Figure 20, where we plot the evolution of the topography with time in both plan (Figures 20a–20f) and cross-sectional views (Figures 20g–20m). These results show that it is possible to produce the topographic break above the underplating window. The model indeed leads to an increase of topography and slope across the created physiographic transition. It only takes about 1 Myr to produce a topographic break that is dynamically steady in space and time, given the high exhumation rate of about 3 mm yr^{-1} (in 1 Myr, ~3 km of

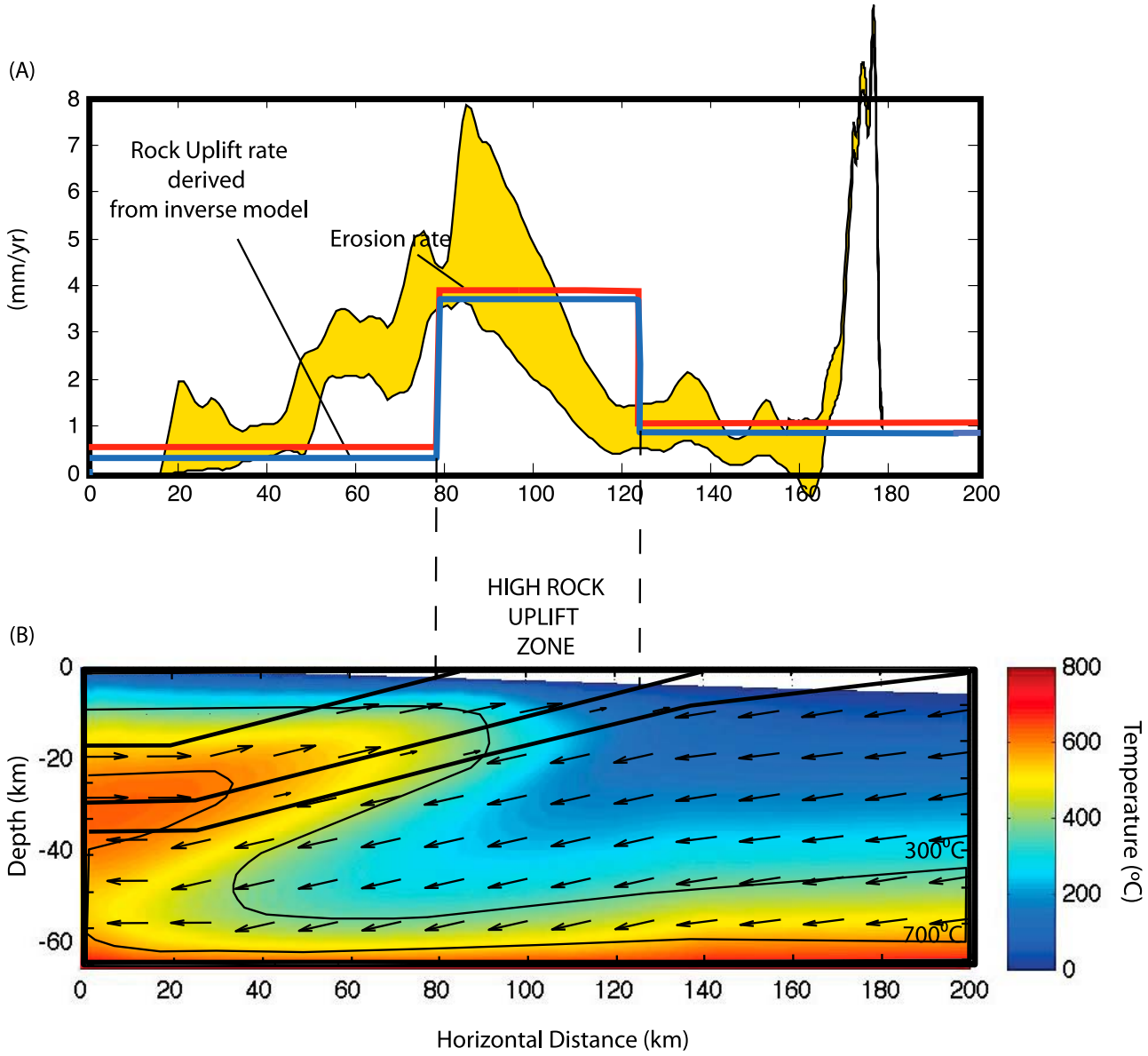

Figure 17. Rock uplift rate, erosion rate, thermal field, and velocity field for the out-of-sequence thrusting model. (a) Rock uplift rate (blue), erosion rate (red), underplating rate, and incision rates from *Lavé and Avouac* [2001] (yellow) are plotted against horizontal distance. Note that the detailed geometry of the MCT is not included in the model, which explains why no high rock uplift is modeled. (b) Thermal field as predicted for the out-of-sequence thrusting model at the end of the simulation. High rock uplift zone is due to thrusting. Small black arrows depict the velocity field predicted by the out-of-sequence thrusting model.

rocks have been uplifted, a third of which has been exhumed and in turn led to an increase of elevation of about 2 km at the physiographic transition). In Figure 20g, we present the real topography extracted from a digital elevation model (Shuttle Radar Topography Mission, U.S. Geological Survey (USGS)) and reduced down to a resolution of 1 km comparable to that used in the model. The similarity between the two topographies is surprisingly striking. To further illustrate the comparison, we directly compare the swath profile from Figure 2a to a 2-D projected view of the model predictions in Figure 20m. It again shows how successful the imposed kinematic model is at simulating the physiographic transition.

[56] While the topographic break tends to evolve toward a steady state position, which is controlled by tectonics, the main tributaries remain affected by horizontal advection (similarly to what is observed in the Himalayas [*Stüwe et al.*, 2008] and other orogens, as pointed by *Herman and Braun* [2006]). Hence, in a framework of reference attached to the MFT, the transport of geomorphic features to the south is inevitable. Moreover, the simulation illustrates that the drainage network can rapidly adapt given the high exhu-

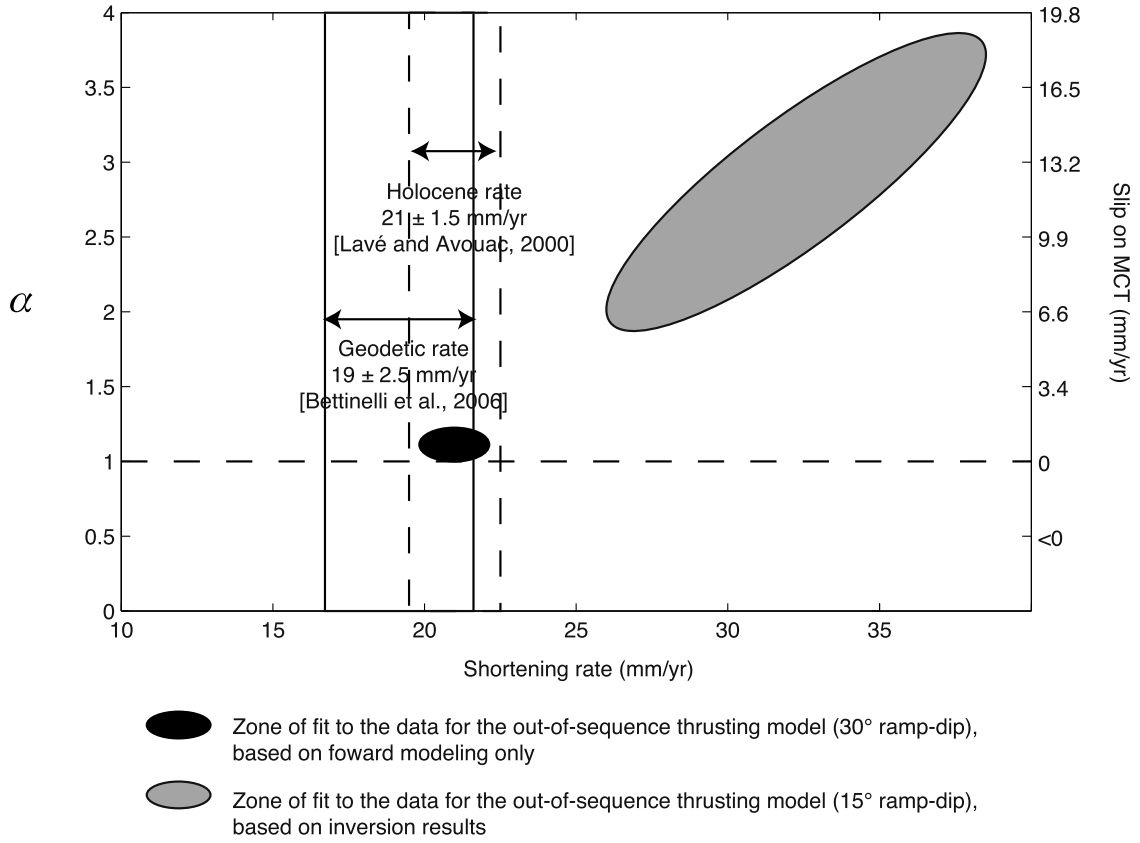

Figure 18. Estimated shortening rate across the range compared to the shortening rate required by the out-of-sequence thrusting model. Estimated geodetic rate of shortening across the whole range [*Bettinelli et al.*, 2006] are depicted with the black line, and Holocene shortening rates due to slip on the MFT [*Lavé and Avouac*, 2000] are depicted with long dashed line. For the clarity, we do not show the recent estimates of *DeCelles and Decelles* [2001] of ~22 mm yr^{-1}. The gray ellipse shows the zone of fit the data extracted from the inversion using a 15° ramp dip. The black ellipse shows the zone of fit using a 30° ramp dip.

mation rates (for instance by comparing Figures 20h and 20k).

7. Three-Dimensional Coupled Landscape Evolution/Thermokinematic Model

[57] The coupling of the landscape evolution model CASCADE with the thermokinematic model PECUBE allows evaluation of the effect of the evolving topography on the thermal structure and thus relax the assumption made in the 2-D models used for the inversion. Also it allows evaluation of what kind of variability in the distribution of cooling ages, peak metamorphic temperatures and pressure might be expected due to the topography. In Figure 21a, we show the peak pressure reached by rocks exposed at the surface. Similarly to the 2-D forward model, predicted peak pressure profiles agree well with field data from the MCT zone and HHC in central Nepal. A sharp pressure drop of several kbars is observed between the HHC and LHS units. Adopting this simplified definition of MCT stated above, the model produces a zone of HHC rocks that have been overthrusted above LHS rocks, forming a nappe. This klippe can be seen as an equivalent in space and age to the Kathmandu klippe. It also illustrates small variations of the parameters of the duplex model can explain the emplacements of klippes along the Himalayan front.

[58] Figure 21b shows the $^{40}Ar/^{39}Ar$ in muscovite ages. Similarly to the 2-D models, a zone of reset ages appears locally in the footwall of the MCT, in its direct vicinity. This zone corresponds to rocks that have experienced temperatures higher than 400°C as recorded in the RSCM data. At lower structural levels, $^{40}Ar/^{39}Ar$ in muscovite ages are rapidly unreset in the LHS (much older ages can be expected as reported by *Wobus et al.* [2003], while those on the nappe are reset and linearly increase to the south. For the lower closer temperature system ((U-Th)/He in zircon (Figure 21c) and apatite FT (Figure 21d), there is no real distinction between HHC and LHS rocks.

[59] The argument relating the change of exhumation rates to the change of age-elevation relationship slopes is often based on the assumption that the surface topography, or more precisely the shape of the drainage network, does not evolve with time. This has been the case for recent studies in the Nepal Himalaya [e.g., *Huntington et al.*, 2006; *Whipp et al.*, 2007]. Our coupled model includes this complexity. To illustrate the effect it might have on age-elevation data, in Figure 22 we present model predictions within the MCT zone. In Figure 5b, we plot the model predictions within the box shown in Figure 21b. The apatite FT ages are within the

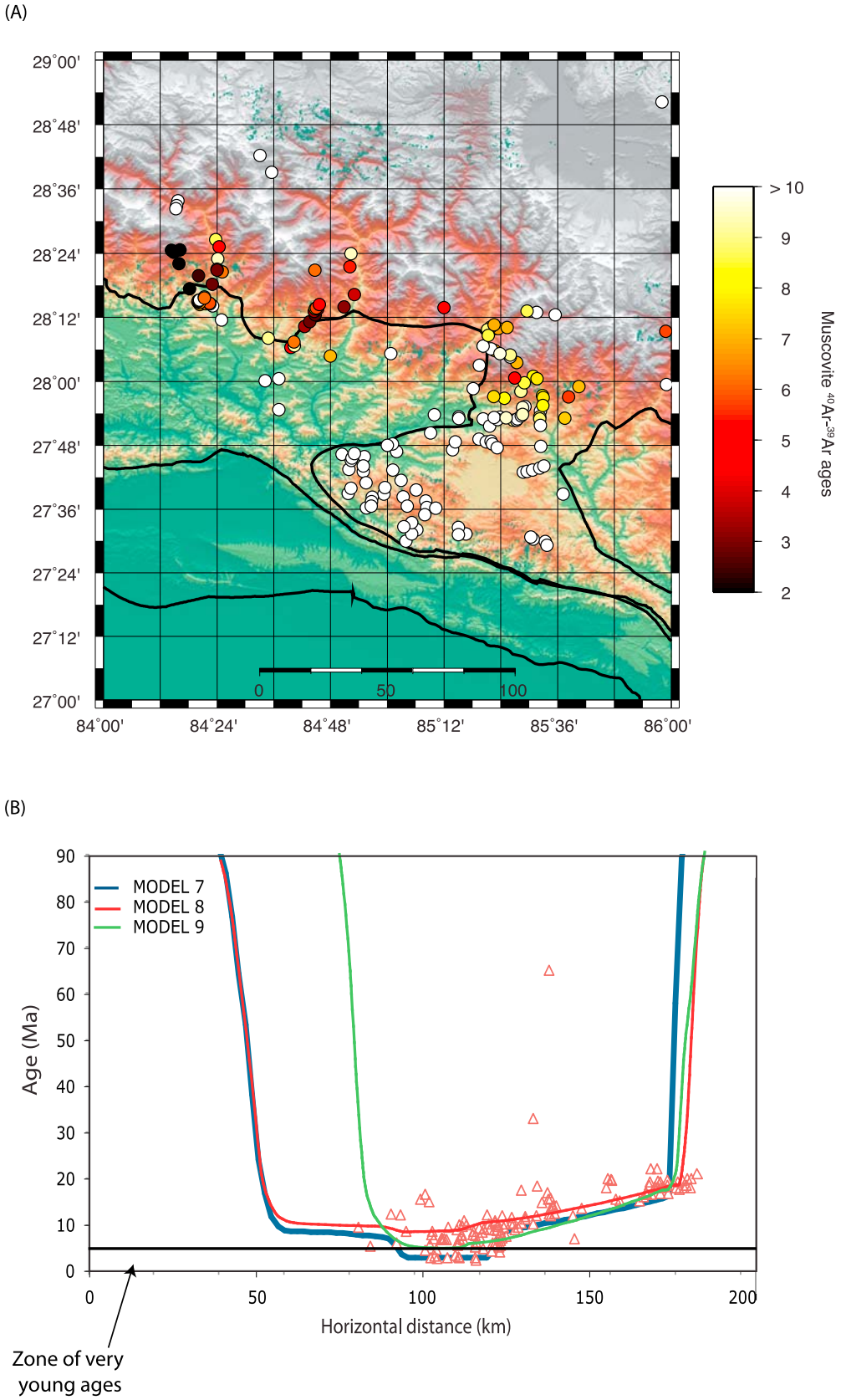

Figure 19. (a) The $^{40}Ar/^{39}Ar$ ratio in muscovite ages in central Nepal. (b) The $^{40}Ar/^{39}Ar$ ratio in muscovite ages versus horizontal (map) distance for the out-of-sequence model for three forward models. The parameters used for each model are summarized in Table 5.

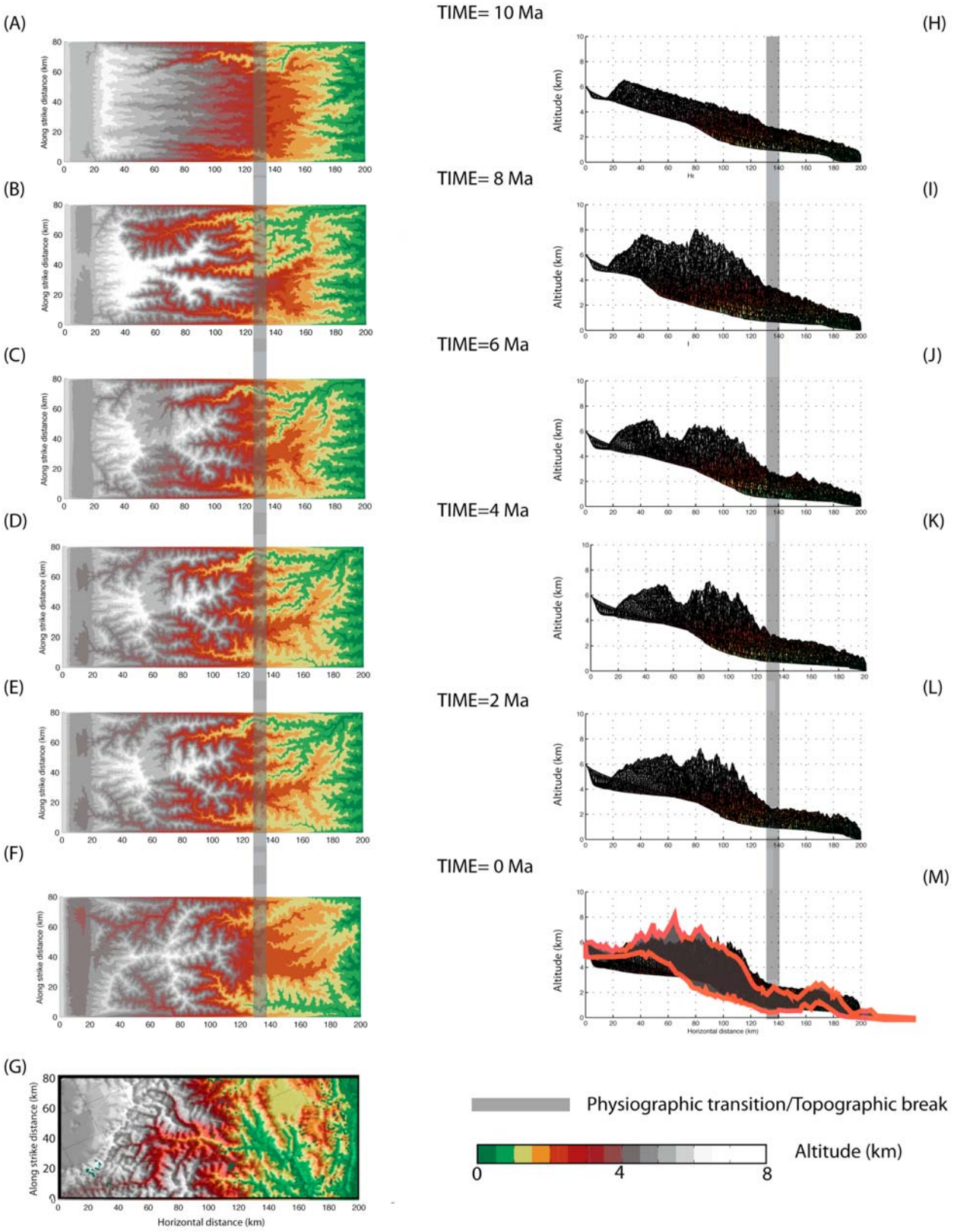

Figure 20. CASCADE simulation. (a–f) Plan view of model prediction forward in time (from initiation of duplex formation (~10 Ma) to today. (g) Real topography extracted from Figure 1. (h–m) Mean and maximum elevation within a 50 km swath. The gray bar depicts the location of the physiographic transition or topographic break. (m) The red line illustrates the swath topography across central Nepal that is overlaid on the model results.

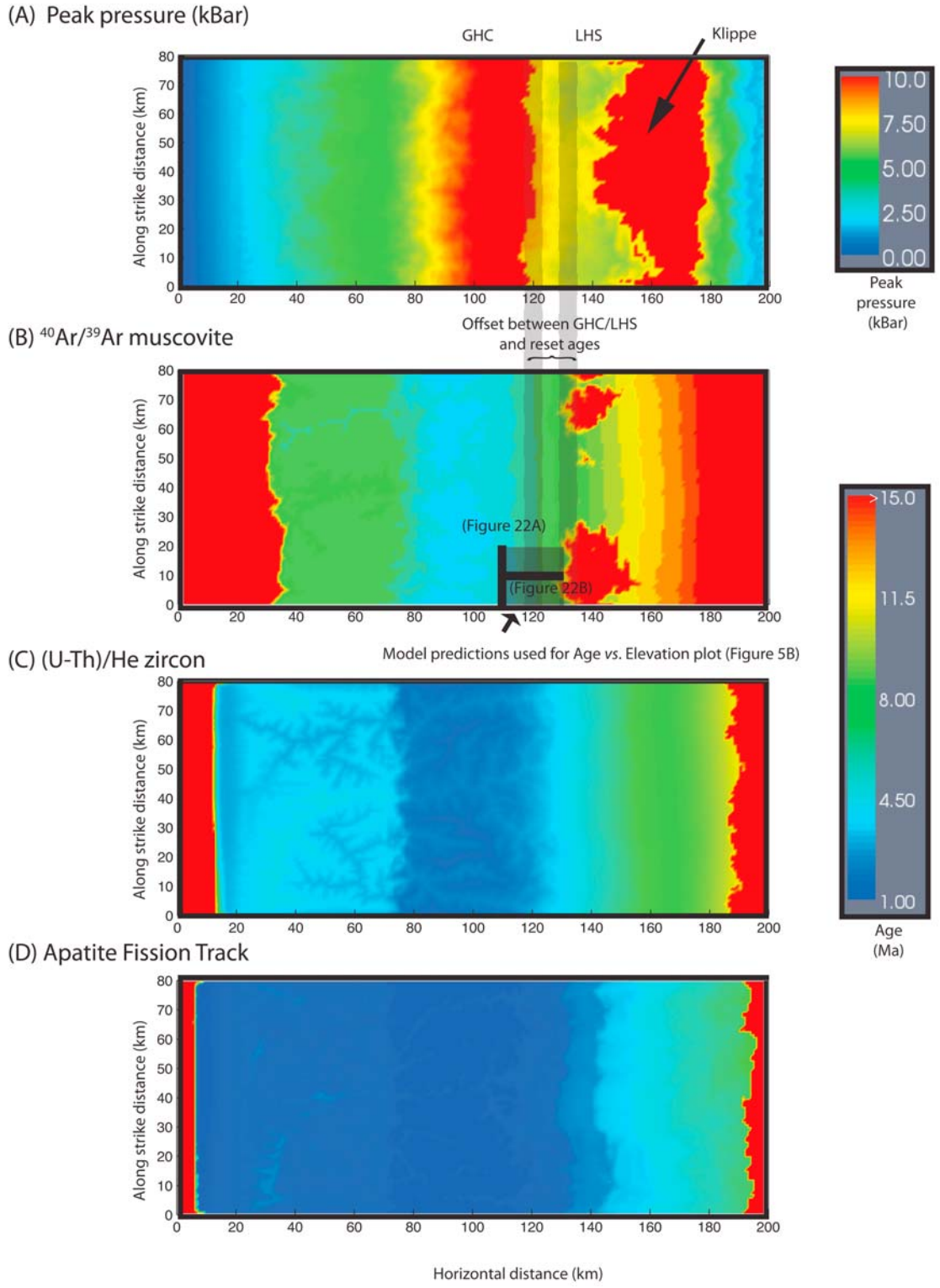

Figure 21. Peak pressure and age predictions for the coupled CASCADE-PECUBE model overlaid on the topographic surface shown in Figure 20m. (a) Peak pressure. (b) The $^{40}Ar/^{39}Ar$ ratio in muscovite ages. (c) (U-Th)/He in zircon ages. (d) Apatite FT ages. The gray lines on Figures 21a and 21b depict the boundary between Indian and Asian rocks.

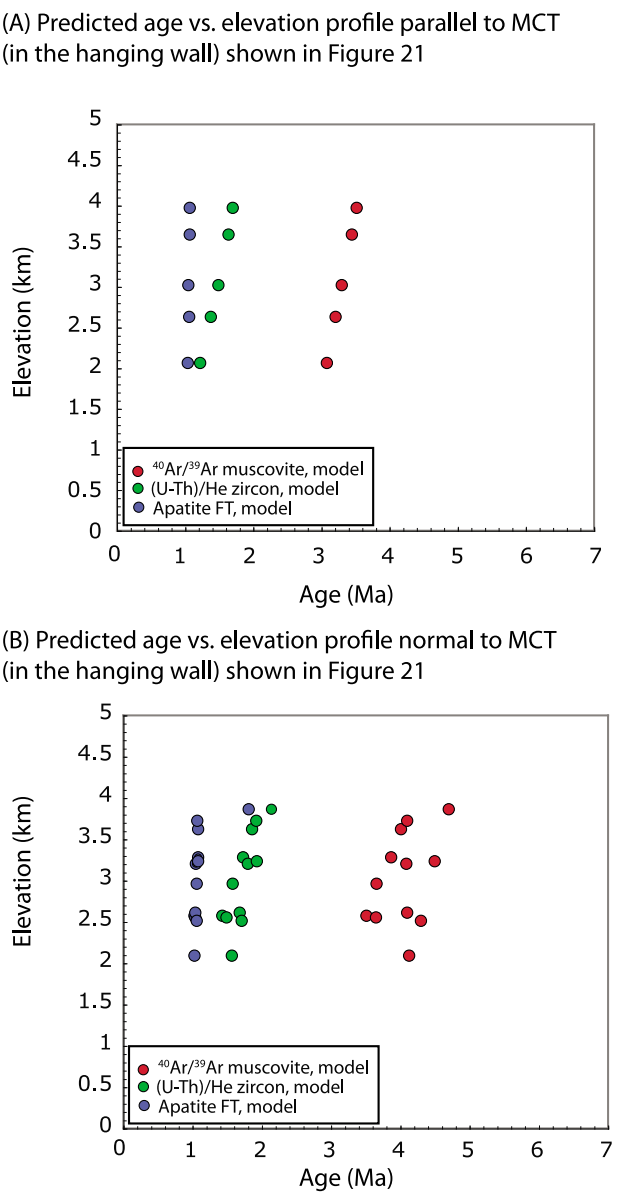

Figure 22. Predicted age-elevation relationships. (a) Along profile parallel to MCT. (b) Along profile perpendicular to MCT.

range of the actual data. Note that given the large uncertainties, it makes no sense to try to explain potential changes in exhumation rates from age-elevation plot, as performed by *Whipp et al.* [2007] or *Huntington et al.* [2006]. The scatter observed in the model predictions of $^{40}Ar/^{39}Ar$ are due to the change of topography with time as well as the geometry (which controls the shape of the isotherms and in turn change of ages with horizontal distance as discussed above). This is further highlighted if the predicted data are projected along a 2-D profile (Figure 23). Figure 23 also shows that not all the scatter in the data can be explained by including an evolving surface topography in the model. In Figure 22a, we extract an age-elevation profile parallel to the MCT, where the exhumation rate is uniform. Slopes of age-elevation relationships are clearly varying as a function of the closure temperature of the system (i.e., slope is higher for lower closure temperature system due to the coupling between the shape of the topography and the underlying isotherms), as previously predicted from numerical modeling [*Braun*, 2002b]. In Figure 22b, we show a profile perpendicular to the MCT. It appears that the slope for the $^{40}Ar/^{39}Ar$ in muscovite system is lower, which would bias estimates of exhumation rates from such a profile [e.g., *Huntington et al.*, 2006]. As a consequence, our models suggest that there could be other ways to interpret the change in age-elevation slope for high- and low-temperature thermochronometers than an acceleration in erosion rate at 2 Ma, as recently suggested by *Huntington et al.* [2006].

[60] Finally, we observe that difference in age with horizontal distance seems to be predominant compared to the difference in elevation. In Figure 7b, we compare zircon (U-Th)/He modeled ages versus the observed ages. It appears that the model does not exhibit any correlation between age an elevation. It rather reflects the fact that the isotherms are nearly vertical where the ages are set. This could either highlight a weakness of the model or the fact that we only use a small amount of data and therefore the derived exhumation rate from the slope of the age-elevation relationship must be treated cautiously. Furthermore, note the model predictions could also be slightly biased since it does not involve high-frequency topography [*Braun*, 2002b] (given the spatial resolution of the landscape evolution model) and does not include the effects of fluid flow in the most upper crust, which should smooth the effects of the shape of the topography on the underlying isotherms [*Whipp and Ehlers*, 2007].

8. Discussion

8.1. Some Common Characteristics of the Out-of-Sequence and Duplex Models: Rapid Erosion of HHC, Low Friction on MHT, and a 4.4–6.8 mm yr^{-1} Overthrusting Rate

[61] It turns out that even with the extensive data set used in this study, it is quite challenging to discriminate the duplex and the out-of-sequence models based only on how they fit the thermochronological data. It is noteworthy that, in order to get these models to fit the data, they must share some common characteristics. Although the out-of-sequence model requires a slip rate on the MCT that seems too large if the dip on the ramp and MCT is 15° (see discussion in section 5.2), the rate of overthrusting of the Lesser Himalaya is well constrained to 4.4–6.8 mm yr^{-1}, since as mentioned above it is primarily dictated by the horizontal gradient of cooling ages. Note that these results are in agreement with estimates of *Avouac* [2003], *Bollinger et al.* [2004a, 2006], and *Brewer and Burbank* [2006]. The young cooling ages at front of the High Himalaya require a zone with rapid exhumation estimated to about 3 ± 0.9 mm yr^{-1} (Figures 15 and 17). The mean exhumation rate is estimated to about 0.9 ± 0.31 mm yr^{-1} in the Lesser Himalaya.

[62] The effect of shear heating due to frictional sliding along the MHT has to be small, implying a low effective friction on the MHT no greater than 0.07. The mechanical modeling of *Cattin and Avouac* [2000] provided a kinematic

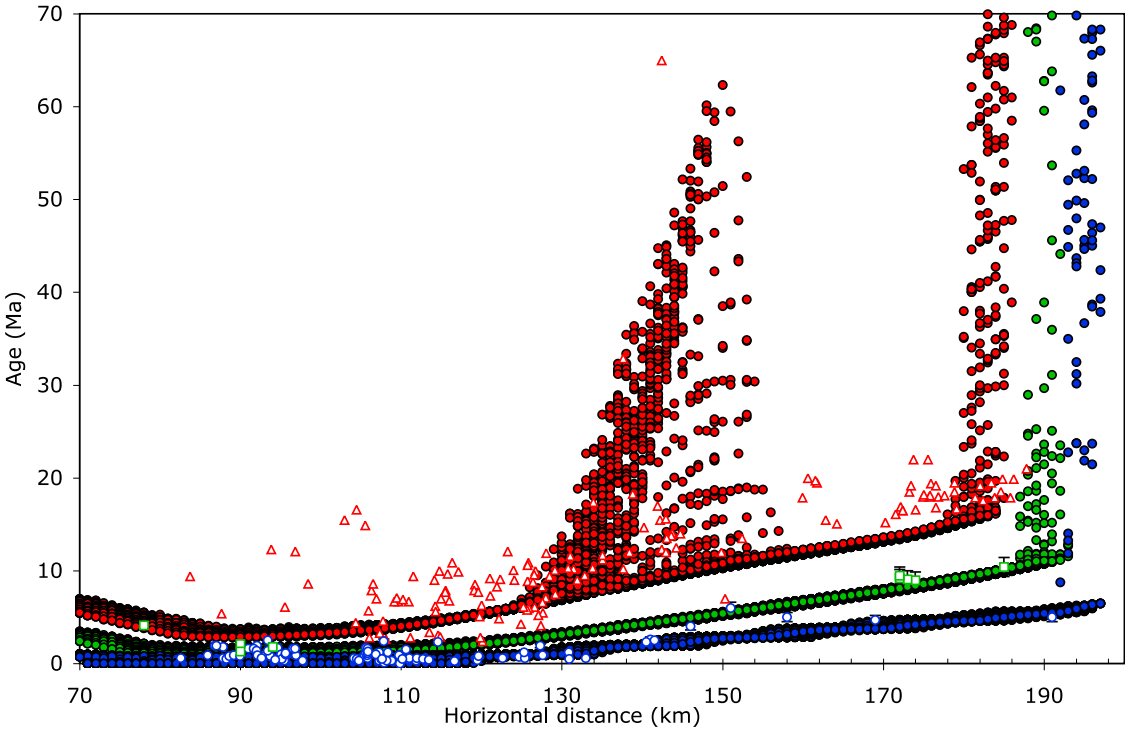

Figure 23. A 2-D stack view of model predictions shown in Figure 21 compared to data. Model predictions are indicated by red dots for muscovite $^{40}Ar/^{39}Ar$, green dots for zircon (U-Th)/He, and blue dots for apatite FT. Actual data are indicated by red triangles for muscovite $^{40}Ar/^{39}Ar$, green open dots for zircon (U-Th)/He, and blue open dots for apatite FT.

field that is mechanically plausible and appears to be consistent with our findings. They also provided an estimate of effective friction coefficient along the MHT, which they suggest to be, in order to simulate long-term deformation, lower than 0.13. Furthermore, this value appears to be in agreement with the low taper angle of the Himalayan wedge [*Davis et al.*, 1983; *Cattin and Avouac*, 2000; *Hilley and Strecker*, 2004] and the low deviatoric stresses inferred from the effect of topography on seismicity [*Bollinger et al.*, 2004b].

8.2. Importance of Thermochronological Data South of the MCT

[63] While the data reported in those studies were compatible with that model, the data presented mainly by *Bollinger et al.* [2004a] and here clearly suggest that such late stage thrusting is not required in any part of the Nepal Himalaya. The most important difference between previous studies and the present work is the number of samples and the size of the sampled area within the footwall of the MCT (i.e., within the Lesser Himalaya). It seems the thermal history of large-scale faults is difficult to ascertain using the results of small-scale studies. Moreover, when considering the thermal history of metamorphic rocks (as opposed to, for example, volcanic rocks), concentration on small areas may tend to lead one to overestimate the importance of an individual data set. Statements such as the Rb-Sr biotite data for both the country rocks and pegmatites suggest further cooling of the Kathmandu complex at circa 7.5 Ma [*Johnson and Rogers*, 1997] implies the events at circa 7.5 Ma were somehow different from 8.5 or 6.5 Ma. Although we also report here data of this age we do not ascribe any particular geologic significance to this time. The importance of a particular sample comes not from the sample itself but how it can be placed in a spatial and temporal continuum.

8.3. Erosion Rate Pattern Across the Range

[64] The general pattern of rock uplift/exhumation rate derived from both models compares reasonably well with the river incision rates estimated by *Lavé and Avouac* [2001], which is representative of the Holocene period (Figures 15 and 17). In the zone of high exhumation, the rates are equal to 3.0 ± 0.9 mm yr^{-1} (Figures 11c and 13c) over the 9.8 ± 1.7 Ma (Figures 11c and 13d), which is a few millimeters per year smaller than the patterns of river downcutting during the Holocene modeled by *Lavé and Avouac* [2001] and more recently by *Garzanti et al.* [2007] based on sediment fluxes. The difference might be due to the fact that over the Holocene uplift pattern is primarily controlled by thrusting over the midcrustal ramp, while the effect of the episodic migration of the ramp associated with the development of the duplex leads to a somewhat lower uplift rate over the long term. Another possible explanation would be a transient response to deglaciation. *Church and Ryder* [1972] and more recently *Herman and Braun* [2006, 2008], who concentrated on a tectonically active area somewhat comparable to the rates observed in the Himalayas, showed that the transition from glacial to fluvial conditions at the end of the last glaciation

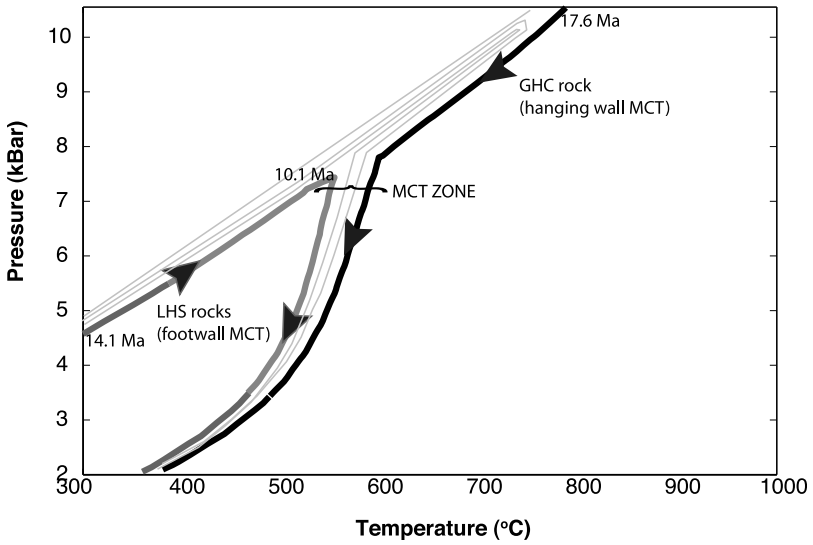

Figure 24. *PT* paths predicted within the MCT zone. LHS rocks experience a tight clockwise loop. GHC rocks experience a completely different history.

may lead to important modifications of the landscape and, in turn, substantial increase of erosion.

8.4. Physiographic Transition

[65] The rock uplift pattern predicted by the duplex model enables us to explain the presence of the topographic break above the underplating window. The feedback mechanisms are strong, since erosion accommodates rock uplift by increasing its local slopes and relief. In the model, we do not include orographically controlled precipitation. It seems obvious that high precipitation is required to maintain the intense incision rates; which is translated in our model by using a high value for K. However, one cannot resolve whether this increase of local rock uplift is due to the natural evolution of the deformation of the orogenic wedge or is related to any change in climate.

8.5. Significance of Age-Elevation Transects

[66] Age-elevation is a measurement of exhumation rate, which at steady state equal rock uplift rate (u), if the isotherms are horizontal, if the wavelength of the topography is sufficiently small for a given thermochronometer [*Braun*, 2002a] and in the absence of horizontal tectonic advection [*Stüwe and Hintermüller*, 2000; *Herman et al.*, 2007a]. It is important to realize it differs from erosion rate if horizontal advection is not small (i.e., $E = u + v\,[\partial h/\partial x]$). In general, it might be erroneous to interpret age-elevation relationship only in terms of vertical exhumation only. For example, if the wavelength of the topography is too large [*Braun*, 2002b] and the isotherms parallel to the topography, cooling ages are independent of elevation.

[67] Furthermore, we observe in our models that, because the imposed kinematics, the isotherms become vertical where the ages of most of the LHS rocks are set, in turn erasing any relationship between ages and elevation (i.e., all the ages are the same).

8.6. Lateral and Temporal Variations

[68] The 2-D duplex model explains relatively well the general trends seen in the thermochronological and thermometric data, but not much of the scatter even if the effect of the topography in three dimensions is taken into account (Figures 21 and 23) and not the youngest ages between the MCT and STD reported in the Marsyangdi area. This might be because the model ignores lateral variations of processes as well as temporal variations. It is clear that there must be some lateral variations within the study area, merely to explain that the Kathmandu klippe does not extend to the west. Only some remnants are preserved, such as the Damauli klippe [*Bollinger et al.*, 2004a]. This suggests that the accretion rate related to the growth of the LHS duplex is probably faster south of the Annapurna area where the klippe has totally been eroded away. This is also consistent with nonreset $^{40}Ar/^{39}Ar$ ages in the LHS which are found closer to the MCT zone [e.g., *Wobus et al.* 2003]. A more rapid accretion rate in this area could be the signature of indentation by of the Himalayan range by some structure of the Indian basement (namely the Faizabad ridge) [*Bollinger et al.*, 2004a]. Regarding temporal variations, the model only considers one major temporal change which corresponds to the onset of the duplex formation dated to 9.8 ± 1.7 Ma. This major change in the kinematics of crustal deformation is required and our estimate of its age corroborates earlier estimates derived from independent arguments by *Robinson et al.* [2003] or *Huyghe et al.* [2001]. One may argue that the timing of duplex formation in the late Miocene could be linked to stronger monsoon across Asia at that time [*Derry and France-Lanord*, 1996; *Dettman et al.*, 2001; *Gupta et al.*, 2004]. By contrast, our models and inversion results are in disagreement with *Clift*'s [2006] flux of clastic sediment in the Indus Fan, who observed a decrease of sedimentation rates at that time, and we do not find a clear signature of any other major temporal change over the last 2 Myr as proposed by *Huntington et al.* [2006], who made the inference based on the observation of dif-

ferent elevation-age slopes for $^{40}Ar/^{39}Ar$ and FT cooling ages from the Marsyangdi area. This might be because different slopes obtained from different thermochronometers do not necessarily mean temporal variations (Figure 22). It can simply result from the effect of horizontal advection if the isotherms corresponding the various thermochronometers are not parallel, as is the case in our model (Figure 22).

8.7. MCT Zone

[69] The pathways experienced by HHC and LHS rocks are clearly distinct. In Figure 24, we show the PT paths for rocks within the MCT zone. LHS rocks undergo a tight clockwise loop during retrograde metamorphism, with reburial of rocks down to 7–8 kbar and up to ~550° at circa 10 Ma, to be then rapidly exhumed toward the surface, which is often observed in the LHS rocks of the MCT zone [e.g., *Catlos et al.*, 2002; *Kohn et al.*, 2001; *Caddick et al.*, 2007; *Kohn*, 2008]. The PT path in the HHC is also similar to what has been observed, with rocks that have seen much higher PT conditions. However, the proposed timing of peak metamorphism in this unit must be treated with caution since the peak pressure might have been reached much earlier (i.e., 30–40 Ma) than the temperature, which was probably reached circa 20–25 Ma [*Kohn et al.*, 2004].

9. Conclusions

[70] This study illustrates how, through a formal inversion, a complex and disparate geological data set can be analyzed globally and used to constrain the kinematics of deformation and the thermal characteristics of the crust involved in an orogeny. In this approach, the importance of a particular sample comes not from the sample itself but how it can be placed in a spatial and temporal continuum. We have adopted this approach to address the most debated question of the kinematics of crustal deformation across the central Nepal Himalaya. For the purpose of the study, we have assembled a data set which includes thermochronological, thermometric and thermobarometric data available from the literature that we have complemented with a large suite of new muscovite $^{40}Ar/^{39}Ar$, apatite fission track and zircon (U-Th)/He ages. All the thermochronological data exhibit the same pattern with a near-linear increase from north to south (i.e., from HHC to LHS), except for the $^{40}Ar/^{39}Ar$ ages that show an abrupt increase across the MCT zone in the Marsyangdi area. This pattern can simply be explained by the effect of erosion accompanying overthrusting of the hanging wall of the Main Himalayan Thrust Fault [e.g., *Avouac*, 2003]. The pattern of exhumation ages is also found to require an erosion rate of 3.0 ± 0.9 mm yr^{-1} in the HHC, significantly higher than the 0.9 ± 0.31 mm yr^{-1} erosion rate in the Lesser Himalaya. Other characteristics in the data, in particular the pattern of peak metamorphic temperatures, point to a necessary component of underplating. We were able to derive thermokinematic models which account for these characteristics and explain to first order the assembled data set. This successfully demonstrates the internal consistency of the data set considered in this study. These data, when considered alone, are consistent with either the out-of-sequence model or the duplex model. However, because the out-of-sequence model would imply a improbably large thrusting rate on the MCT, we favor a simple model in which, over the past 10 Myr, the Himalayan wedge would have grown primarily by underplating, associated with the growth of duplex involving Lesser Himalaya units. We cannot exclude however occasional thrusting at front of the High Himalaya. In any case, the scenario in which the HHC would be extruded due to coeval slip on a thrust fault at front of the high range, close to the MCT zone, and the STD, seems unlikely. The duplex model provides also a simple explanation for the steep front of the high range, and its location about 80 km north of where the basal detachment beneath the Himalayan wedge reaches the surface. In this scenario, locally higher erosion at front of the High Himalaya is compensated by locally higher underplating rather than by out-of-sequence thrusting. Following this model, the MCT zone would actually correspond with the contact between the rocks that were accreted to the Himlayan wedge at great depth and those accreted at shallower depth and colder temperature due to the development of the Lesser Himalayan Duplex. Finally, our analysis brings in additional constraints on some thermal characteristics of the crust in the Himalaya, in particular the radiogenic heat production of HHC and LHS rocks, and shows that a low effective friction on the MHT, less than 0.10, is required.

Appendix A: Analytical Methods for $^{40}Ar/^{39}Ar$ Data

[71] Samples were wrapped in Sn, Cu, or Al foil and stacked in quartz tubes. Individual packets averaged 3 mm thick and fluence monitors were placed every 5 to 8 mm along the tube. Synthetic K-rich glass and optical grade CaF2 were included in each irradiation package to monitor the interfering reactions producing neutron-induced argon from K and Ca. Measured correction factors are given in Table 2.

[72] Fluence monitors used in this study were either Fish Canyon Tuff sanidine or GA1550 biotite. Age used for these monitors when calculating the age of unknowns were 27.9 Ma [*Steven et al.*, 1967; *Cebula et al.*, 1986] and 97.3 Ma for the sanidine and biotite, respectively. Except for one irradiation package, heating of the fluence monitors was done using a 10W CO2 laser, heating 1 to 3 crystals at a time. Reactive gases evolved from the samples during heating were removed from the system using a 50 s^{-1} SAES getter for 5 min after heating was completed. In these instances, J factors for the fluence monitors were calculated by taking the average of three to six such analyses. In the other irradiation, ~1 mg packages of fluence monitors (in this case sanidine) were heated in a resistance furnace to 1550°C and the J factor was taken using this one analysis. Fluence gradients seen in individual tubes ranged from 2 to 17%. The uncertainty assigned to an individual J factor ranged from 0.1 to 0.9%. The uncertainty in J associated with unknowns ranged from 0.5 to 1.5%; this uncertainty is included in the total uncertainty reported for the unknowns.

[73] All unknown samples were heated using a resistance furnace similar to the design described by *Staudecher et al.* [1978] and *Harrison and Fitzgerald* [1986]. Wrapped packets of mica had a net weight which ranged from 2.0 to

41.1 mg (most were in the range 5 to 10 mg). Samples irradiated in Al were mostly repackaged in Sn foil before heating; samples irradiated in Sn or Cu were heated in the same package as irradiation. Samples heated in Sn were heated at ~300°C for ~5 min and this gas was not analyzed. No low-temperature heating was applied to Cu packages. Heating times were generally 12 min for each heating step. Details of the heating schedule of individual samples can be found in the auxiliary material. In the furnace heating reactive gases evolved from the samples during heating were removed from the system using 10 s^{-1} SAES getter during heating and an additional 50 s^{-1} SAES getter for 5 min after heating was completed.

[74] Mass spectrometric analysis was achieved using a Mass Analyzer Products 215–50 rare-gas mass spectrometer. Trap current in the source was maintained at 200 μA. Signal intensities were measured using a Johnston electron multiplier. The sensitivity of this device is approximately 10^{-17} mol mV^{-1}. Samples were measured by peak hopping through the masses 40 to 36 over at least seven cycles. Initial peak height at the time of introduction into the mass spectrometer were determined by regression of the data (intensity versus time) to time zero. Blank values of the system for laser heating were determined after every two to four fluence monitors; the system blank for the furnace was determined after every one to three samples by running a series of steps over the same temperature range used in heating the samples. The blank versus temperature plot was then used to determine the appropriate blank value for a particular step of an unknown run. The entire laboratory is automated through a computer allowing standardized operating conditions.

[75] Two previous studies have reported $^{40}Ar/^{39}Ar$ data from this region. Because this technique is based on the relative difference in age between an unknown sample and a standard of known age it is important to note which standards and methods were used when comparing data from different laboratories. *Macfarlane* [1993] reported $^{40}Ar/^{39}Ar$ data relative to three different standards: (1) an in-house standard of the University of Maine at Orono, SB-51, with an age of 246.7 Ma, (2) the hornblende Mmhb-1 with an associated age of 520.4 Ma, and (3) Fish Canyon Tuff sanidine with an age of 27.8 Ma. While it is difficult to compare to an in-house standard for which no intercalibration data are published, only three of the muscovites of *Macfarlane* [1993] were measured relative to this standard. The two other standards are well known and corrections could be made for the difference in monitor age assignment used in these studies but the differences would likely not be greater than the reported uncertainty. The data of *Arita et al.* [1997] were reported relative to the standard hornblende Mmhb-1; this standard has had several ages proposed in the literature [*Samson and Alexander*, 1987]. However, *Arita et al.* [1997] did not report which age they used; this makes intercalibration between labs difficult. Another problem inherent in the $^{40}Ar/^{39}Ar$ method is that in addition to the (n,p) reaction which produces ^{39}Ar from ^{39}K, other reactions produce unwanted amounts of ^{40}Ar and ^{37}Ar (as well as ^{39}Ar not from K). These interfering reactions become more important with young samples but the problems associated with them can be overcome by irradiating zero-age K- and Ca-rich materials and applying the Ar isotopic ratios obtained from this material to unknown samples to account for these reactions before calculation of ages [see *McDougall and Mark*, 1988]. It is important to measure these correction factors in each irradiation as the magnitude of these reactions is dependant on the power of the nuclear reactor which varies with time. The samples reported by *Arita et al.* [1997] were irradiated in the TRIGA reactor at the USGS in Denver. They did not say exactly when the irradiation took place but they did note that they applied the correction factors of *Dalrymple et al.* [1981]; this suggests to us that these values were 10 years or more out of date. We do not have experience with the USGS reactor in Denver but our experience with the reactor at the University of Michigan in this project alone suggests that using old correction factors could lead to erroneous values (see Table 3).

[76] As mentioned in the main text, if a precision of only ~1 Myr is required, the differences noted above between our data and previously published data may not pose a serious problem but we suggest a more detailed comparison of these results may not be warranted (especially in the case of the *Arita et al.* [1997] data).

Appendix B: Analytical Methods for Fission Track Data

[77] Analytical procedures for apatite fission track analysis followed the techniques described in detail by *Green* [1986]. Apatite grains were separated from crushed samples using conventional magnetic and heavy liquid techniques, mounted in epoxy resin on glass slides, ground and polished to reveal an internal surface, and etched in 5N HNO_3 at room temperature for 20 s to reveal fossil fission tracks. Samples were irradiated in the X-7 position of the Australian HIFAR Research Reactor. Thermal neutron fuences were monitored adjacent to the standard glass CN-5 and ages were determined using the external detector method. Fission tracks were counted at a magnification of 1250x (dry objective) using a fully computer-controlled Zeiss Axiotron microscope, and only those grains orientated parallel to the *c* axis that displayed sharp polishing scratches were counted. Fission track ages were calculated using the zeta calibration method [*Hurford and Green*, 1983] with central ages and errors calculated according to *Galbraith and Laslett* [1993].

Appendix C: Analytical Methods for on (U-Th)/He Dating of Palung Samples

[78] The Palung samples are from leucogranite (PL3 and 7), granite (PL4 and 6) and one amphibole bearing alkaline granite (PL5) collected along a 1070 m high vertical profile. All the separates present good yield of euhedral, medium to small size zircon (48.6 to 68.6 μm in diameter). One to two replicates and three to four replicates of one zircon were dated for the Palung samples, respectively.

[79] Grain dimensions were measured under a microscope to determine the α ejection correction [*Farley et al.*, 1996]. All replicates were loaded in a platinum capsule and laser heated for He extraction for 30 min at ~1300°C following the procedures described by *Tagami et al.* [2003]. Capsules were transferred into graphite crucibles and fused at 1200°C with ultrapure LiBO2. The resulting glass was then dissolved in 10% HNO_2, spiked with ^{235}U and ^{230}Th, analyzed

on a Finnegan ICP-MS, following the procedure described by *Mahéo et al.* [2007].

[80] For each sample we report the mean age of the replicates. For each replicate, typical analytical error on the age based on analytical uncertainty in U, Th and He measurement are 2% (1σ [*Farley*, 2002]). Uncertainties on the mean ages are reported as 1σ standard errors using the standard deviation of the replicate analyses divided by $(n-1)^{1/2}$, where n is the number of replicate analyses performed. For the samples with two replicates the errors are the age difference between the two replicates divided by two. All error estimates are larger than the analytical error alone and are intended to reflect the age uncertainty due to differences in grain size, minor crystal defects, or zoning of parent material, which may contribute to age differences and uncertainties in the alpha ejection correction [*Wolf et al.*, 1996; *Meesters and Dunai*, 2002; *Herman et al.*, 2007b]. (U-Th)/He zircon analytical data are available in Table 3. Replicates gave relatively good reproducibility (the standard deviation represent less than 6.6%).

[81] **Acknowledgments.** This work was partially funded by the Tectonics Observatory of the California Institute of Technology thanks to a grant from the Gordon and Betty Moore Foundation. The computations presented here were performed on the Pangu facility at the Geological and Planetary Science Division, California Institute of Technology. We thank Ken Farley for making his laboratory available for the (U-Th)/He analyses. We thank Mark Harrison, Amos Aikman, Itai Haviv, and Peter van der Beek for discussions and comments on previous versions of this manuscript. Kip Hodges, Kate Huntington, and Cameron Wobus are thanked for their useful reviews.

References

Appel, E., W. Rösler, and G. Corvinus (1991), Magnetostratigraphy of the Miocene-Pleistocene Surai Khola Siwaliks in west Nepal, *Geophys. J. Int.*, *105*(1), 191–198, doi:10.1111/j.1365-246X.1991.tb03455.x.

Arita, K. (1983), Origin of the inverted metamorphism of the lower Himalayas, central Nepal, *Tectonophysics*, *95*, 43–60, doi:10.1016/0040-1951(83)90258-5.

Arita, K., and Y. Ganzawa (1997), Thrust tectonics and uplift process of the Nepal Himalaya revealed from fission-track ages, *J. Geogr.*, *106*, 156–167.

Arita, K., R. Dallmeyer, and A. Takasu (1997), Tectonothermal evolution of the Lesser Himalaya, Nepal: Constraints from $^{40}Ar/^{39}Ar$ ages from the Kathmandu Nappe, *Isl. Arc*, *6*, 372–385, doi:10.1111/j.1440-1738.1997.tb00047.x.

Avouac, J. P. (2003), Mountain building, erosion, and the seismic cycle in the Nepal Himalaya, *Adv. Geophys.*, *46*, 1–80, doi:10.1016/S0065-2687(03)46001-9.

Avouac, J.-P. (2007), Dynamic processes in extensional and compressional settings—Mountain building: From earthquakes to geological deformation, in *Treatise of Geophysics*, vol. 6, *Crust and Lithosphere Dynamics*, edited by A. B. Watts, pp. 377–439, doi:10.1016/B978-044452748-6.00112-7, Elsevier, Boston, Mass.

Beaumont, C., R. A. Jamieson, M. H. Nguyen, and B. Lee (2001), Himalayan tectonics explained by extrusion of a low-viscosity crustal channel coupled to focused surface denudation, *Nature*, *414*, 738–742, doi:10.1038/414738a.

Beaumont, C., R. A. Jamieson, M. H. Nguyen, and S. Medvedev (2004), Crustal channel flows: 1. Numerical models with applications to the tectonics of the Himalayan-Tibetan Orogen, *J. Geophys. Res.*, *109*, B06406, doi:10.1029/2003JB002809.

Bettinelli, P., J.-P. Avouac, M. Flouzat, F. Jouanne, L. Bollinger, P. Willis, and G. Chitraker (2006), Plate motion of India and interseismic strain in the Nepal Himalaya from GPS and DORIS measurements, *J. Geod.*, *80*, 567–589, doi:10.1007/s00190-006-0030-3.

Beyssac, O., L. Bollinger, J. P. Avouac, and B. Goffe (2004), Thermal metamorphism in the lesser Himalaya of Nepal determined from Raman spectroscopy of carbonaceous material, *Earth Planet. Sci. Lett.*, *225*, 233–241, doi:10.1016/j.epsl.2004.05.023.

Bilham, R., et al. (1997), GPS measurements of present-day convergence across the Nepal Himalaya, *Nature*, *386*, 61–64, doi:10.1038/386061a0.

Blythe, A. E., D. W. Burbank, A. Carter, K. M. Schmidt, and J. Putkonen (2007), Plio-Quaternary exhumation history of the central Nepalese Himalaya: 1. Apatite and zircon fission track and apatite (U-Th)/He analyses, *Tectonics*, *26*, TC3002, doi:10.1029/2006TC001990.

Bollinger, L., and E. Janots (2006), Evidence for Mio-Pliocene retrograde monazites from the Lesser Himalayan metamorphic series in far western Nepal, *Eur. J. Mineral.*, *18*(3), 289–297, doi:10.1127/0935-1221/2006/0018-0289.

Bollinger, L., J. P. Avouac, O. Beyssac, E. J. Catlos, T. M. Harrison, M. Grove, B. Goffe, and S. Sapkota (2004a), Thermal structure and exhumation history of the Lesser Himalaya in central Nepal, *Tectonics*, *23*, TC5015, doi:10.1029/2003TC001564.

Bollinger, L., J.-P. Avouac, R. Cattin, and M. R. Pandey (2004b), Stress buildup in the Himalaya, *J. Geophys. Res.*, *109*, B11405, doi:10.1029/2003JB002911.

Bollinger, L., P. Henry, and J. P. Avouac (2006), Mountain building in the Nepal Himalaya: Thermal and kinematic model, *Earth Planet. Sci. Lett.*, *244*, 58–71, doi:10.1016/j.epsl.2006.01.045.

Bonnet, C., J. Malavieille, and J. Mosar (2007), Interactions between tectonics, erosion, and sedimentation during the recent evolution of the alpine orogen: Analogue modeling insights, *Tectonics*, *26*, TC6016, doi:10.1029/2006TC002048.

Braun, J. (2002a), Estimating exhumation rate and relief evolution by spectral analysis of age-elevation datasets, *Terra Nova*, *14*, 210–214, doi:10.1046/j.1365-3121.2002.00409.x.

Braun, J. (2002b), Quantifying the effect of recent relief changes on age-elevation relationship, *Earth Planet. Sci. Lett.*, *200*, 331–343, doi:10.1016/S0012-821X(02)00638-6.

Braun, J. (2003), Pecube: A new finite element code to solve the heat transport equation in three dimensions in the earth's crust including the effects of a time-varying, finite amplitude surface topography, *Comput. Geosci.*, *29*(6), 787–794, doi:10.1016/S0098-3004(03)00052-9.

Braun, J., and M. Sambridge (1997), Modelling landscape evolution on geological time scales: A new method based on irregular spatial discretization, *Basin Res.*, *9*, 27–52, doi:10.1046/j.1365-2117.1997.00030.x.

Braun, J., and P. van der Beek (2004), Evolution of passive margin escarpments: What can we learn from low-temperature thermochronology?, *J. Geophys. Res.*, *109*, F04009, doi:10.1029/2004JF000147.

Brewer, I., and D. W. Burbank (2006), Thermal and kinematic modeling of bedrock and detrital cooling ages in the central Himalaya, *J. Geophys. Res.*, *111*, B09409, doi:10.1029/2004JB003304.

Brown, L. D., W. Zhao, K. D. Nelson, M. Hauck, D. Alsdorf, A. Ross, M. Cogan, M. Clark, X. Liu, and J. Che (1996), Bright spots, structure, and magmatism in southern Tibet from INDEPTH seismic reflection profiling, *Science*, *274*, 1688–1690, doi:10.1126/science.274.5293.1688.

Brunel, M., and J. Kienast (1986), Etude pétro-structurale des chevauchements ductiles himalayens sur la transversale de l'Everest-Makalu, *Can. J. Earth Sci.*, *23*, 1117–1137, doi:10.1139/e86-111.

Brunel, M., M. Colchen, P. Le Fort, G. Mascle, and A. Pecher (1979), Structural analysis and tectonic evolution of the central Himalaya of Nepal, in *Structural Geology of the Himalaya*, edited by P. Saklani, pp. 247–264, Today and Tomorrow's, New Delhi.

Burbank, D. W., A. E. Blythe, J. Putkonen, B. Pratt-Sitaula, E. Gabet, M. Oskin, A. Barros, and T. Ojha (2003), Decoupling of erosion and precipitation in the Himalayas, *Nature*, *426*, 652–655, doi:10.1038/nature02187.

Burchfiel, B., C. Zhiliang, K. V. Hodges, L. Yuping, L. H. Royden, D. Changrong, and X. Jiene (1992), The south Tibetan detachment system, Himalayan orogen: Extension contemporaneous with and parallel to shortening in a collisional mountain belt, *Spec. Pap. Geol. Soc. Am.*, *269*, 48 pp.

Burg, J., and T. Gerya (2005), Viscous heating and thermal doming in orogenic metamorphism: Numerical modeling and geological implications, *J. Metamorph. Geol.*, *23*, 75–95, doi:10.1111/j.1525-1314.2005.00563.x.

Burg, J., M. Brunel, D. Gapais, G. Chen, and G. Liu (1984), Deformation of leucogranites of the crystalline Main Central Sheet in southern Tibet (China), *J. Struct. Geol.*, *6*, 535–542, doi:10.1016/0191-8141(84)90063-4.

Byerlee, J. (1978), Friction of rocks, *Pure Appl. Geophys.*, *116*, 615–626, doi:10.1007/BF00876528.

Caddick, M., M. Bickle, N. Harris, T. Holland, M. Horstwood, R. Parrish, and T. Ahmad (2007), Burial and exhumation history of a Lesser Himalayan schist: Recording the formation of an inverted metamorphic sequence in NW India, *Earth Planet. Sci. Lett.*, *264*, 375–390, doi:10.1016/j.epsl.2007.09.011.

Catlos, E. J. (2000), Geochronologic and thermobarometric constraints on the evolution of the main central thrust, Himalayan orogen, Ph.D. thesis, Univ. of Calif., Los Angeles.

Catlos, E., T. M. Harrison, M. Kohn, M. Grove, M. Ryerson, C. E. Manning, and B. N. Upreti (2001), Geochronologic and thermobarometric constraints on the evolution of the Main Central Thrust, central Nepal Himalaya, *J. Geophys. Res.*, *106*, 16,177–16,204, doi:10.1029/2000JB900375.

Catlos, E. J., L. D. Gilley, and T. M. Harrison (2002), Interpretation of monazite ages obtained via in situ analysis, *Chem. Geol.*, *188*, 193–215, doi:10.1016/S0009-2541(02)00099-2.

Cattin, R., and J.-P. Avouac (2000), Modeling mountain building and the seismic cycle in the Himalaya of Nepal, *J. Geophys. Res.*, *105*, 13,389–13,407, doi:10.1029/2000JB900032.

Cebula, G. T., M. J. Kunk, H. H. Mehnert, C. W. Naeser, J. D. Obradovich, and J. F. Sutter (1986), The Fish Canyon tuff, a potential standard for the $^{40}Ar/^{39}Ar$ and fission-track dating methods, *Terra Cognita*, *6*, 139–140.

Célérier, J., T. M. Harrison, O. Beyssac, F. Herman, W. J. Dunlap, and A. A. G. Webb (2009), The Kumaun and Garwhal Lesser Himalaya, India: Part 2. Thermal and deformation histories, *Geol. Soc. Am. Bull.*, *121*, 1281–1297, doi:10.1130/B26343.1.

Church, M., and J. M. Ryder (1972), Paraglacial sedimentation: A consideration of fluvial processes conditioned by glaciation, *Geol. Soc. Am. Bull.*, *83*, 3059–3072, doi:10.1130/0016-7606(1972)83[3059:PSACOF]2.0.CO;2.

Clift, P. (2006), Controls on the erosion of Cenozoic Asia and the flux of clastic sediment to the ocean, *Earth Planet. Sci. Lett.*, *241*, 571–580, doi:10.1016/j.epsl.2005.11.028.

Coleman, M. E., and K. V. Hodges (1998), Contrasting Oligocene and Miocene thermal histories from the hanging wall and footwall of the south Tibetan detachment in the central Himalaya from $^{40}Ar/^{39}Ar$ thermochronology, Marsyandi Valley, central Nepal, *Tectonics*, *17*, 726–740, doi:10.1029/98TC02777.

Copeland, P., T. M. Harrison, K. V. Hodges, P. Maruejol, P. Lefort, and A. Pêcher (1991), An early Pliocene thermal disturbance of the Main Central Thrust, central Nepal: Implications for Himalayan tectonics, *J. Geophys. Res.*, *96*, 8475–8500, doi:10.1029/91JB00178.

Dalrymple, G. B., E. C. Alexander, M. A. Lanphere, and G. P. Krager (1981), Irradiations of samples for $^{40}Ar/^{39}Ar$ dating using the Geological Survey Triga reactor, *U.S. Geol. Surv. Prof. Pap.*, *1176*, 55 pp.

Davis, D., J. Suppe, and F. A. Dahlen (1983), Mechanics of fold-and-thrust belts and accretionary wedges, *J. Geophys. Res.*, *88*, 1153–1172, doi:10.1029/JB088iB02p01153.

DeCelles, P. G., and P. C. Decelles (2001), Rates of shortening, propagation, underthrusting, and flexural wave migration in continental orogenic systems, *Geology*, *29*, 135–138, doi:10.1130/0091-7613(2001)029<0135:ROSPUA>2.0.CO;2.

DeCelles, P. G., D. M. Robinson, J. Quade, T. Ojha, C. Garzione, P. Copeland, and B. N. Upreti (2001), Stratigraphy, structure, and tectonic evolution of the Himalayan fold-thrust belt in western Nepal, *Tectonics*, *20*, 487–509, doi:10.1029/2000TC001226.

Derry, L., and C. France-Lanord (1996), Neogene Himalayan weathering history and river $^{8}7Sr/^{8}6Sr$; impact on the marine Sr record, *Earth Planet. Sci. Lett.*, *142*, 59–74, doi:10.1016/0012-821X(96)00091-X.

Dettman, D. L., M. J. Kohn, J. Quade, F. J. Ryerson, T. P. Ojha, and S. Hamidullah (2001), Seasonal stable isotope evidence for a strong Asian monsoon throughout the past 10.7 Ma, *Geology*, *29*, 31–34, doi:10.1130/0091-7613(2001)029<0031:SSIEFA>2.0.CO;2.

Edwards, M., W. S. F. Kidd, J. Li, Y. Yue, and M. Clark (1996), Multi-stage development of the southern Tibet detachment system near Khula Kangri. New data from Gonto La, *Tectonophysics*, *260*, 1–19, doi:10.1016/0040-1951(96)00073-X.

England, P., P. Le Fort, P. Molnar, and A. Pêcher (1992), Heat sources for Tertiary metamorphism and anatexis in the Annapurna-Manaslu region (central Nepal), *J. Geophys. Res.*, *97*, 2107–2128, doi:10.1029/91JB02272.

Farley, K. A. (2002), (U-Th)/He dating: Techniques, calibrations, and applications, in *Noble Gases in Geochemistry and Cosmochemistry*, *Rev. Mineral. Geochem.*, 47, 819–843, doi:10.2138/rmg.2002.47.18.

Farley, K. A., R. Wolf, and L. Silver (1996), The effect of long alpha-stopping distances on (U-Th)/He dates, *Geochim. Cosmochim. Acta*, *60*, 4223–4229, doi:10.1016/S0016-7037(96)00193-7.

Galbraith, R. F., and G. M. Laslett (1993), Statistical models for mixed fission track ages, *Nucl. Tracks Radiat. Meas.*, *21*, 459–470, doi:10.1016/1359-0189(93)90185-C.

Gansser, A. (1964), *Geology of the Himalayas*, Interscience, London.

Garzanti, E., G. Vezzoli, S. Ando, J. Lavé, M. Attal, C. France-Lanord, and P. DeCelles (2007), Quantifying sand provenance and erosion (Marsyandi River, Nepal Himalaya), *Earth Planet. Sci. Lett.*, *258*, 500–515, doi:10.1016/j.epsl.2007.04.010.

Graham, C. M., and P. C. England (1976), Thermal regimes and regional metamorphism in the vicinity of overthrust faults: An example of shear heating and inverted metamorphic zonation from southern California, *Earth Planet. Sci. Lett.*, *31*, 142–152, doi:10.1016/0012-821X(76)90105-9.

Green, P. F. (1986), On the thermo-tectonic evolution of northern England: Evidence from fission track analysis, *Geol. Mag.*, *123*, 493–506, doi:10.1017/S0016756800035081.

Guillot, S., M. Cosca, P. Allemand, and P. Le Fort (1999), Contrasting metamorphic and geochronologic evolution along the Himalayan belt, in *Himalaya and Tibet: Mountain Roots to Mountain Tops*, edited by A. Macfarlane, R. Sorkhabi, and J. Quade, *Spec. Pap. Geol. Soc. Am.*, 328, 117–128.

Gupta, K., R. Singh, S. Joseph, and E. Thomas (2004), Indian Ocean high-productivity event (10–8 Ma): Linked to global cooling or to the initiation of the Indian monsoons?, *Geology*, *32*, 753–756, doi:10.1130/G20662.1.

Hansen, F., and N. Carter (1982), Creep of selected crustal rocks at 1000 MPa, *Eos Trans. AGU*, *63*, 437.

Harrison, T. M., and J. D. Fitzgerald (1986), Exsolution in hornblende and its consequences for $^{40}Ar/^{39}Ar$ age spectra and closure temperature, *Geochim. Cosmochim. Acta*, *50*, 247–253, doi:10.1016/0016-7037(86)90173-0.

Harrison, T. M., P. Copeland, S. A. Hall, J. Quade, S. Burner, T. P. Ojha, and W. S. F. Kidd (1993), Isotopic preservation of Himalayan/Tibetan uplift, denudation, and climatic histories of two molasse deposits, *J. Geol.*, *101*, 157–175, doi:10.1086/648214.

Harrison, T., O. Lovera, and M. Grove (1997a), New insights into the origin of two contrasting Himalayan granite belts, *Geology*, *25*, 899–902, doi:10.1130/0091-7613(1997)025<0899:NIITOO>2.3.CO;2.

Harrison, T. M., F. J. Ryerson, P. Le Fort, A. Yin, O. M. Lovera, and E. J. Catlos (1997b), A late Miocene-Pliocene origin for the central Himalayan inverted metamorphism, *Earth Planet. Sci. Lett.*, *146*, E1–E7, doi:10.1016/S0012-821X(96)00215-4.

Harrison, T. M., M. Grove, O. M. Lovera, and E. J. Catlos (1998), A model for the origin of Himalayan anatexis and inverted metamorphism, *J. Geophys. Res.*, *103*, 27,017–27,032, doi:10.1029/98JB02468.

Harrison, T. M., J. Célérier, A. Aikman, J. Hermann, and T. M. Heizler (2009), Diffusion of 40ar in muscovite, *Geochim. Cosmochim. Acta*, *73*, 1039–1051, doi:10.1016/j.gca.2008.09.038.

Hauck, M. L., K. D. Nelson, L. D. Brown, W. Zhao, and A. R. Ross (1998), Crustal structure of the Himalayan orogen at ~90° east longitude from Project INDEPTH deep reflection profiles, *Tectonics*, *17*, 481–500, doi:10.1029/98TC01314.

Heim, A., and A. Gansser (1939), Central Himalaya: Geological observations of the Swiss expedition 1936, *Denkschr. Schweiz. Naturforsch. Ges.*, *73*, 245 pp.

Henry, P., X. Le Pichon, and B. Goffé (1997), Kinematic, thermal and petrological model of the Himalayas: Constraints related to metamorphism within the underthrust Indian crust and topographic elevation, *Tectonophysics*, *273*, 31–56, doi:10.1016/S0040-1951(96)00287-9.

Herman, F., and J. Braun (2006), Landform response to horizontal shortening and glaciations: A study in the Southern Alps of New Zealand, *J. Geophys. Res.*, *111*, F01008, doi:10.1029/2004JF000248.

Herman, F., and J. Braun (2008), Evolution of the glacial landscape of the Southern Alps of New Zealand: Insights from a glacial erosion model, *J. Geophys. Res.*, *113*, F02009, doi:10.1029/2007JF000807.

Herman, F., J. Braun, and W. Dunlap (2007a), Tectonomorphic scenarios in the Southern alps of New Zealand, *J. Geophys. Res.*, *112*, B04201, doi:10.1029/2004JB003472.

Herman, F., J. Braun, T. Senden, and W. Dunlap (2007b), (U-Th)/He chronometry: Mapping 3D geometry using micro-X-ray tomography and solving the associated production-diffusion equation, *Chem. Geol.*, *242*, 126–136, doi:10.1016/j.chemgeo.2007.03.009.

Hetényi, G., R. Cattin, J. Vergne, and J. Nabelek (2006), The effective elastic thickness of the India plate from receiver function imaging, gravity anomalies and thermomechanical modelling, *Geophys. J. Int.*, *167*(3), 1106–1118, doi:10.1111/j.1365-246X.2006.03198.x.

Hilley, G., and M. Strecker (2004), Steady state erosion of critical Coulomb wedges with applications to Taiwan and the Himalaya, *J. Geophys. Res.*, *109*, B01411, doi:10.1029/2002JB002284.

Hirn, A., and M. Sapin (1984), The Himalayan zone of crustal interaction, *Ann. Geophys.*, *39*, 205–249.

Hodges, K. V., J. M. Hurtado, and K. X. Whipple (2001), Southward extrusion of Tibetan crust and its effect on Himalayan tectonics, *Tectonics*, *20*, 799–809, doi:10.1029/2001TC001281.

Hodges, K. V., C. Wobus, K. Ruhl, T. Schildgen, and K. Whipple (2004), Quaternary deformation, river steepening, and heavy precipitation at the front of the Higher Himalayan ranges, *Earth Planet. Sci. Lett.*, *220*, 379–389, doi:10.1016/S0012-821X(04)00063-9.

Huerta, A. D., L. H. Royden, and K. V. Hodges (1998), The thermal structure of collisional orogens as a response to accretion, erosion, and radiogenic heating, *J. Geophys. Res.*, *103*, 15,287–15,302, doi:10.1029/98JB00593.

Huerta, A. D., L. H. Royden, and K. V. Hodges (1999), The effects of accretion, erosion and radiogenic heat on the metamorphic evolution of collisional orogens, *J. Metamorph. Geol.*, *17*, 349–366, doi:10.1046/j.1525-1314.1999.00204.x.

Huntington, K. W., and K. V. Hodges (2006), A comparative study of detrital mineral and bedrock age-elevation methods for estimating erosion rates, *J. Geophys. Res.*, *111*, F03011, doi:10.1029/2005JF000454.

Huntington, K. W., A. E. Blythe, and K. V. Hodges (2006), Climate change and late Pliocene acceleration of erosion in the Himalaya, *Earth Planet. Sci. Lett.*, *252*, 107–118, doi:10.1016/j.epsl.2006.09.031.

Huntington, K. W., T. A. Ehlers, K. V. Hodges, and D. M. Whipp Jr. (2007), Topography, exhumation pathway, age uncertainties, and the interpretation of thermochronometer data, *Tectonics*, *26*, TC4012, doi:10.1029/2007TC002108.

Hurford, A. J., and P. F. Green (1983), The zeta age calibration of fission-track dating, *Chem. Geol.*, *41*, 285–317, doi:10.1016/S0009-2541(83)80026-6.

Hurtado, J. M., K. V. Hodges, and K. X. Whipple (2001), Neotectonics of the Thakkhola graben and implications for recent activity on the south Tibetan fault system in the central Nepal Himalaya, *Geol. Soc. Am. Bull.*, *113*(2), 222–240, doi:10.1130/0016-7606(2001)113<0222:NOTTGA>2.0.CO;2.

Huyghe, P., A. Galy, J.-L. Mugnier, and C. France-Lanord (2001), Propagation of the thrust system and erosion in the Lesser Himalaya: Geochemical and sedimentological evidence, *Geology*, *29*, 1007–1010, doi:10.1130/0091-7613(2001)029<1007:POTTSA>2.0.CO;2.

Johnson, M. R. W., and G. Rogers (1997), Rb-Sr ages of micas from the Kathmandu complex, central Nepalese Himalaya: Implications for the evolution of the main central thrust, *J. Geol. Soc.*, *154*, 863–869, doi:10.1144/gsjgs.154.5.0863.

Jouanne, F., J. L. Mugnier, M. R. Pandey, J. F. Gamond, P. Le Fort, L. Serrurier, C. Vigny, and J. P. Avouac, and the Idylhim Members (1999), Oblique convergence in the Himalayas of western Nepal deduced from preliminary results of GPS measurements, *Geophys. Res. Lett.*, *26*(13), 1933–1936, doi:10.1029/1999GL900416.

Jouanne, L., J.-L. Mugnier, J. Gamond, P. Le Fort, M. Pandey, L. Bollinger, M. Flouzat, and J.-P. Avouac (2004), Current shortening across the Himalayas of Nepal, *Geophys. J. Int.*, *157*(1), 1–14, doi:10.1111/j.1365-246X.2004.02180.x.

Kaneko, Y. (1995), Thermal structure in the Annapurna region, central Nepal Himalaya: Implications for inverted metamorphism, *J. Mineral. Petrol. Econ. Geol.*, *90*, 143–154, doi:10.2465/ganko.90.143.

Kelley, S. (2002), Excess argon in K-Ar and Ar-Ar geochronology, *Chem. Geol.*, *188*, 1–22, doi:10.1016/S0009-2541(02)00064-5.

Kohn, M. J. (2008), P-T-t data from central Nepal support critical taper and repudiate large-scale channel flow of the Greater Himalayan Sequence, *Geol. Soc. Am. Bull.*, *120*(3), 259–273, doi:10.1130/B26252.1.

Kohn, M., E. J. Catlos, F. J. Ryerson, and T. M. Harrison (2001), Pressure-temperature-time path discontinuity in the Main Central Thrust zone, central Nepal, *Geology*, *29*, 571–574, doi:10.1130/0091-7613(2001)029<0571:PTTPDI>2.0.CO;2.

Kohn, M. J., M. Wieland, C. Parkinson, and B. N. Upreti (2004), Miocene faulting at plate tectonic velocity in the Himalaya of central Nepal, *Earth Planet. Sci. Lett.*, *228*, 299–310, doi:10.1016/j.epsl.2004.10.007.

Konstantinovskaia, E., and J. Malavieille (2005), Erosion and exhumation in accretionary orogens: Experimental and geological approaches, *Geochem. Geophys. Geosyst.*, *6*, Q02006, doi:10.1029/2004GC000794.

Kooi, H., and C. Beaumont (1996), Large-scale geomorphology: Classical concepts reconciled and integrated with contemporary ideas via surface processes model, *J. Geophys. Res.*, *101*(B2), 3361–3386, doi:10.1029/95JB01861.

Larson, K., R. Burgmann, R. Bilham, and J. Freymueller (1999), Kinematics of the India-Eurasia collision zone from GPS measurements, *J. Geophys. Res.*, *104*, 1077–1093, doi:10.1029/1998JB900043.

Lavé, J. (1997), Active thrusting and river incision across the Himalaya of Nepal, Ph.D. thesis, Univ. Paris VII Denis Diderot, Paris.

Lavé, J., and J.-P. Avouac (2000), Active folding of fluvial terraces across the Siwalik Hills (Himalaya of central Nepal), *J. Geophys. Res.*, *105*, 5735–5770, doi:10.1029/1999JB900292.

Lavé, J., and J.-P. Avouac (2001), Fluvial incision and tectonic uplift across the Himalayas of central Nepal, *J. Geophys. Res.*, *106*, 26,561–26,591, doi:10.1029/2001JB000359.

LeFort, P. (1975), Himalaya: The collided range; present knowledge of continental arc, *Am. J. Sci.*, *275A*, 1–44.

Lemonnier, C., G. Marquis, F. Perrier, J. Avouac, G. Chitrakar, B. Kafle, S. Sapkota, U. Gautam, D. Tiwari, and M. Bano (1999), Electrical structure of the Himalaya of central Nepal: High conductivity around the mid-crustal ramp along the MHT, *Geophys. Res. Lett.*, *26*, 3261–3264, doi:10.1029/1999GL008363.

Lyon-Caen, H., and P. Molnar (1983), Constraints on the structure of the Himalaya from an analysis of gravity anomalies and a flexural model of the lithosphere, *J. Geophys. Res.*, *88*, 8171–8191, doi:10.1029/JB088iB10p08171.

Macfarlane, A. (1993), Chronology of tectonic events in the crystalline core of the Himalaya, Langtang National Park, central Nepal, *Tectonics*, *12*, 1004–1025, doi:10.1029/93TC00916.

Macfarlane, A., K. V. Hodges, and D. Lux (1992), A structural analysis of the Main Central Thrust zone, Langtang National Park, central Nepal Himalaya, *Geol. Soc. Am. Bull.*, *104*, 1389–1402, doi:10.1130/0016-7606(1992)104<1389:ASAOTM>2.3.CO;2.

Mahéo, G., P. Leloup, F. Valli, R. Lacassin, N. Arnaud, J. Paquette, A. Fernandez, L. Haibing, K. Farley, and P. Tapponnier (2007), Post 4 Ma initiation of normal faulting in southern Tibet: Constraints from the Kung Co half graben, *Earth Planet. Sci. Lett.*, *256*, 233–243, doi:10.1016/j.epsl.2007.01.029.

Martin, A., G. Gehrels, and P. DeCelles (2007), The tectonic significance of (U,Th)/Pb ages of monazite inclusions in garnet from the Himalaya of central Nepal, *Chem. Geol.*, *244*, 1–24, doi:10.1016/j.chemgeo.2007.05.003.

McDougall, I. H., and T. Mark (1988), *Geochronology and Thermochronology by the $^{40}Ar/^{39}Ar$ Method*, *Oxford Monogr. Geol. Geophys.*, vol. 9, Oxford Univ. Press, New York.

Meesters, A. G. C. A., and T. J. Dunai (2002), Solving the production-diffusion equation for finite diffusion domains of various shape: Part I. Implications for low-temperature (U-Th)/He thermochronology, *Chem. Geol.*, *186*, 333–344, doi:10.1016/S0009-2541(01)00422-3.

Menon, R., P. Kumar, G. Reddy, and R. Srinivasan (2003), Radiogenic heat production of late Archaean Bundelkhand granite and some Proterozoic gneisses and granitoids of central India, *Curr. Sci.*, *85*, 634–638.

Molnar, P., and P. England (1990), Late Cenozoic uplift of mountain ranges and global climate change: Chicken and egg?, *Nature*, *346*, 29–34, doi:10.1038/346029a0.

Molnar, P., and H. Lyon-Caen (1989), Fault plane solutions of earthquakes and active tectonics of the Tibetan Plateau and its margins, *Geophys. J. Int.*, *99*, 123–154, doi:10.1111/j.1365-246X.1989.tb02020.x.

Molnar, P., and P. Tapponnier (1975), Cenozoic tectonics of Asia: Effects of a continental collision, *Science*, *189*, 419–426, doi:10.1126/science.189.4201.419.

Mugnier, J.-L., and P. Huyghe (2006), The Ganges basin geometry records a pre-15 Ma isostatic rebound of Himalaya, *Geology*, *34*, 445–448, doi:10.1130/G22089.1.

Mugnier, J.-L., P. Leturmy, G. Mascle, P. Huyghe, E. Chalaron, G. Vidal, L. Husson, and B. Delcaillau (1999), The Siwaliks of western Nepal: I. Geometry and kinematics, *J. Asian Earth Sci.*, *17*(5–6), 629–642, doi:10.1016/S1367-9120(99)00038-3.

Nelson, K. D., et al. (1996), Partially molten middle crust beneath southern Tibet: Synthesis of project INDEPTH results, *Science*, *274*, 1684–1688, doi:10.1126/science.274.5293.1684.

Pandey, M. R., R. P. Tandukar, J.-P. Avouac, J. Lavé, and J. P. Massot (1995), Interseismic strain accumulation on the Himalaya crustal ramp (Nepal), *Geophys. Res. Lett.*, *22*, 751–754, doi:10.1029/94GL02971.

Patriat, P., and J. Achache (1984), India–Eurasia collision chronology has implications for crustal shortening and driving mechanism of plates, *Nature*, *311*, 615–621, doi:10.1038/311615a0.

Pêcher, A. (1989), The metamorphism in central Himalaya, *J. Metamorph. Geol.*, *7*, 31–41, doi:10.1111/j.1525-1314.1989.tb00573.x.

Powell, C., and P. Conaghan (1973), Plate tectonics and the Himalayas, *Earth Planet. Sci. Lett.*, *20*, 1–12, doi:10.1016/0012-821X(73)90134-9.

Rai, S. M. (1998), Etude structurale, metamorphique, geochimique et radiochronologique des nappes deKatmandou et du Gosainkund, Himalaya du Nepal central, Ph.D. thesis, Univ. Joseph Fourier, Grenoble, France.

Rai, S. M., S. Guillot, P. Le Fort, and B. N. Upreti (1998), Pressure-temperature evolution in the Kathmandu and Gosainkund regions, central Nepal, *J. Asian Earth Sci.*, *16*(2–3), 283–298, doi:10.1016/S0743-9547(98)00019-1.

Ray, L., A. Bhattacharya, and S. Roy (2007), Thermal conductivity of Higher Himalayan crystallines from Garhwal Himalaya, India, *Tectonophysics*, *434*, 71–79, doi:10.1016/j.tecto.2007.02.003.

Robinson, D. M., P. G. DeCelles, C. N. Garzione, O. N. Pearson, T. M. Harrison, and E. J. Catlos (2003), Kinematic model for the Main Central Thrust in Nepal, *Geology*, *31*, 359–362, doi:10.1130/0091-7613(2003)031<0359:KMFTMC>2.0.CO;2.

Robinson, D. M., P. G. DeCelles, and P. Copeland (2006), Tectonic evolution of the Himalayan thrust belt in western Nepal: Implications for channel flow models, *Geol. Soc. Am. Bull.*, *118*, 865–885, doi:10.1130/B25911.1.

Robl, J., K. Stüwe, and S. Hergaten (2008), Channel profiles around Himalayan river anticlines: Constraints on their formation from digital elevation model analysis, *Tectonics*, *27*, TC3010, doi:10.1029/2007TC002215.

Rolfo, F., C. D'Anna, L. Magiapane, and B. Lombardo (2001), A section through the MCT zone, Nepal Himalaya (abstract), *J. Asian Earth Sci.*, *19*(3A), 54–55.

Roy, S., and R. Rao (2000), Heat flow in the Indian shield, *J. Geophys. Res.*, *105*, 25,587–25,604, doi:10.1029/2000JB900257.

Sambridge, M. (1999a), Geophysical Inversion with a Neighbourhood Algorithm -I. Searching a parameter space, *Geophys. J. Int.*, *138*, 479–494, doi:10.1046/j.1365-246X.1999.00876.x.

Sambridge, M. (1999b), Geophysical Inversion with a Neighbourhood Algorithm -II. Appraising the ensemble, *Geophys. J. Int.*, *138*, 727–746, doi:10.1046/j.1365-246x.1999.00900.x.

Samson, S., and E. Alexander (1987), Calibration of the interlaboratory ^{40}Ar–^{39}Ar dating standard, MMhb-1, *Chem. Geol.*, *66*, 27–34, doi:10.1016/0168-9622(87)90025-X.

Schärer, U., and C. Allégre (1983), The Palung granite (Himalaya); high-resolution U-Pb systematics in zircon and monazite, *Earth Planet. Sci. Lett.*, *63*, 423–432, doi:10.1016/0012-821X(83)90115-2.

Schelling, D., and K. Arita (1991), Thrust tectonics, crustal shortening, and the structure of the far eastern Nepal Himalaya, *Tectonics*, *10*, 851–862, doi:10.1029/91TC01011.

Schulte-Pelkum, V., G. Monslave, A. Seehan, M. R. Pandey, S. Sapkota, R. Bilham, and F. Wu (2005), Imaging the Indian subcontinent beneath the Himalaya, *Nature*, *435*, 1222–1225, doi:10.1038/nature03678.

Searle, M. P., and L. Godin (2003), The south Tibetan detachment and the Manaslu Leucogranite: A structural reinterpretation and restoration of the Annapurna-Manaslu Himalaya, Nepal, *J. Geol.*, *111*(5), 505–523, doi:10.1086/376763.

Searle, M. P., R. Law, L. Godin, K. Larson, M. Streule, J. Cottle, and M. Jessup (2008), Defining the Himalayan Main Central Thrust in Nepal, *J. Geol. Soc.*, *165*(2), 523–534, doi:10.1144/0016-76492007-081.

Srivastava, P., and G. Mitra (1994), Thrust geometries and deep structure of the outer and lesser Himalaya, Kumaon and Garhwal (India): Implications for evolution of the Himalayan fold-and-thrust belt, *Tectonics*, *13*, 89–109, doi:10.1029/93TC01130.

Staudecher, T., E. Jessberger, D. Dörflinger, and J. Kiko (1978), A refined ultrahigh-vacuum furnace for rare gas analysis, *J. Phys. Earth*, *11*, 7781–7784.

Steven, T., H. Mehnert, and J. Obradovich (1967), Age of volcanic activity in the San Juan Mountains, Colorado, *U.S. Geol. Surv. Prof. Pap.*, *575-D*, D4–D55.

Stöcklin, J. (1980), Geology of Nepal and its regional frame, *J. Geol. Soc.*, *137*, 1–34, doi:10.1144/gsjgs.137.1.0001.

Stöcklin, J., and K. D. Bhattarai (1977), Geology of the Kathmandu area and central Mahabharat range, *Nepal, Tech. Rep. 86*, Nepal Dep. of Mines and Geol., Kathmandu.

Stüwe, K., and D. Foster (2001), $^{40}Ar/^{39}Ar$, pressure, temperature and fission track constraints on the age and nature of metamorphism around the Main Central Thrust in the eastern Bhutan Himalaya, *J. Asian Earth Sci.*, *19*, 85–95, doi:10.1016/S1367-9120(00)00018-3.

Stüwe, K., and M. Hintermüller (2000), Topography and isotherms revisited: The influence of laterally migrating drainage divides, *Earth Planet. Sci. Lett.*, *184*, 287–303, doi:10.1016/S0012-821X(00)00315-0.

Stüwe, K., J. Robl, S. Hergarten, and L. Evans (2008), Modeling the influence of horizontal advection, deformation, and late uplift on the drainage development in the India-Asia collision zone, *Tectonics*, *27*, TC6011, doi:10.1029/2007TC002186.

Suppe, J. (1983), Geometry and kinematics of fault-bend folding, *Am. J. Sci.*, *283*, 684–721.

Tagami, T., K. A. Farley, and D. F. Stockli (2003), (U-Th)/He geochronology of single zircon grains of known Tertiary eruption age, *Earth Planet. Sci. Lett.*, *207*, 57–67, doi:10.1016/S0012-821X(02)01144-5.

Whipp, D. M., and T. A. Ehlers (2007), Influence of groundwater flow on thermochronometer-derived exhumation rates in the central Nepalese Himalaya, *Geology*, *35*, 851–854, doi:10.1130/G23788A.1.

Whipp, D. M., T. A. Ehlers, A. Blythe, K. Huntington, K. Hodges, and D. W. Burbank (2007), Plio-Quaternary exhumation history of the central Nepalese Himalaya: 2. Thermokinematic and thermochronometer age prediction model, *Tectonics*, *26*, TC3003, doi:10.1029/2006TC001991.

Whipple, K. X., and G. E. Tucker (1999), Dynamics of the stream-power river incision model: Implications for height limits of mountain ranges, landscape response timescales, and research needs, *J. Geophys. Res.*, *104*, 17,661–17,674, doi:10.1029/1999JB900120.

Wobus, C. W., K. V. Hodges, and K. X. Whipple (2003), Has focused denudation sustained active thrusting at the Himalayan topographic front?, *Geology*, *31*, 861–864, doi:10.1130/G19730.1.

Wobus, C., A. M. Heimsath, K. X. Whipple, and K. V. Hodges (2005), Active out-of-sequence thrust faulting in the central Nepalese Himalaya, *Nature*, *434*, 1008–1011, doi:10.1038/nature03499.

Wobus, C. W., K. X. Whipple, and K. V. Hodges (2006), Neotectonics of the central Nepalese Himalaya: Constraints from geomorphology, detrital $^{40}Ar/^{39}Ar$ thermochronology and thermal modeling, *Tectonics*, *25*, TC4011, doi:10.1029/2005TC001935.

Wolf, R. A., K. A. Farley, and L. T. Silver (1996), Helium diffusion and low-temperature thermochronometry of apatite, *Geochim. Cosmochim. Acta*, *60*, 4231–4240, doi:10.1016/S0016-7037(96)00192-5.

Yin, A. (2006), Cenozoic tectonic evolution of the Himalayan orogen as constrained by along-strike variation of structural geometry, exhumation history, and foreland sedimentation, *Earth Sci. Rev.*, *76*, 1–131, doi:10.1016/j.earscirev.2005.05.004.

Zhao, W., K. D. Nelson, and Project INDEPTH Team (1993), Deep seismic-reflection evidence continental underthrusting beneath southern Tibet, *Nature*, *366*, 557–559, doi:10.1038/366557a0.

J.-P. Avouac, Tectonics Observatory, California Institute of Technology, Pasadena, CA 91106, USA.

L. Bollinger, Département Analyse Surveillance Environnement, CEA, DAM, DIF, F-91297 Arpajon, France.

P. Copeland, Department of Earth and Atmospheric Sciences, University of Houston, Houston, TX 77204-5503, USA.

D. Foster, Department of Geological Sciences, University of Florida, PO Box 112120, Gainesville, FL 32611-2120, USA.

P. Henry, CEREGE, Europole de l'Arbois, F-13090 Aix-en-Provence, France.

F. Herman, Earth Sciences Department, ETH Zurich, Haldenbachstrasse 44, CH-8092 Zurich, Switzerland. (frederic@erdw.ethz.ch)

P. Le Fort and A. Pêcher, Institut Dolomieu, Université Joseph Fourier, 15 rue Maurice Gignoux, F-38031 Grenoble, France.

G. Mahéo, Laboratoire des Sciences de La Terre, UMR 5570, Ecole Normale Supérieure de Lyon, Université de Lyon 1, CNRS, F-6922 Villeurbanne, France.

S. Rai, Department of Geology, Tribuhvan University, Kirtipur, Gandhi Bhawan, Kathmandu, Nepal.

K. Stüwe, Institut für Geologie, Universität Graz, Heinrichstr 26, A-8010 Graz, Austria.